Università degli Studi di Cagliari

DOTTORATO DI RICERCA

Ingegneria Elettronica ed Informatica

Ciclo XXXII

TITOLO TESI

UPGRADING THE SARDINIA RADIO TELESCOPE FOR SPACE OBJECTS OBSERVATION AND TRACKING

Settore/i scientifico disciplinari di afferenza

ING-INF/02

Presentata da:	Luca Schirru
Coordinatore Dottorato	Prof. Alessandro Giua
Tutor	Prof. Giorgio Montisci Dr. Alessandro Fanti

Esame finale anno accademico 2018 – 2019

Tesi discussa nella sessione d'esame Gennaio-Febbraio 2020

Sommario

Introduction: space debris mitigation measure

Space debris is defined as all inactive, human-made objects, including fragments, with variable sizes and shapes, orbiting the Earth or reentering the atmosphere. The population of these objects counts more than 500,000 samples, which orbiting around Earth, across three main orbits and is continuously growing, representing a serious threat for space missions [1]. The most crowded orbit is the Low Earth Orbit (LEO), between 200 and 2000 km of altitude, with the highest number of officially catalogued objects with size down to 10 cm (about 24,000) [2]. These debris are more significant than natural meteoroids and they generate two types of risk:

- the in-orbit collision risk for every manned and unmanned spacecraft;
- the risks from reentering debris.

Since travel speeds in LEO are up to 10 km/s [3], even a small object could heavily damage an active satellite or a spacecraft. A collision event could lead to a cascading process in which the impact generates more fragments, significantly greater than the number of damage space crafts. Several years ago, this self-sustained growth in the object population was predicted and studied by Donald Kessler and it is known today as "Kessler syndrome". A graphical representation of the problem is shown in Figure 1, for objects larger than 10 cm.

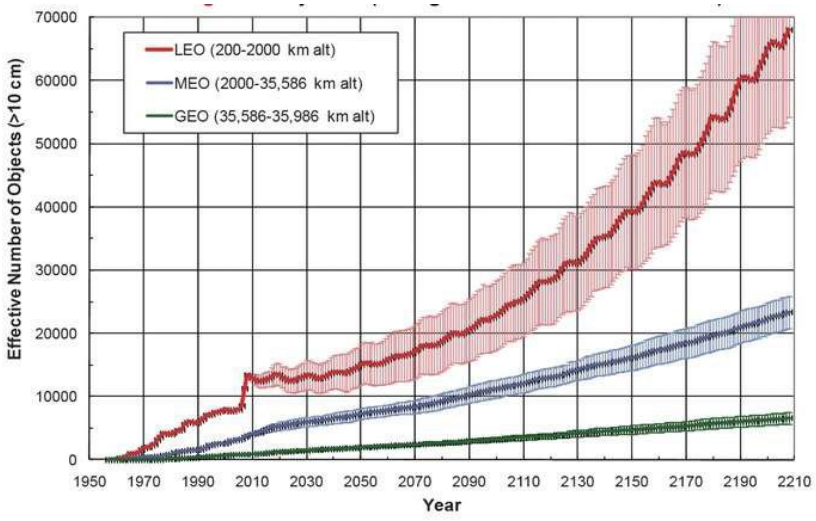

Figure 1- Representation of the Kessler Syndrome.

An interesting fact that arises from this graph is, except the predominance of the objects in LEO, the sudden increase of the red curve slope, around year 2007. Indeed, the majority of the catalogued objects is originated by break-up events. Fundamentally, two of these events are responsible for a considerable increase in the space debris population: the anti-satellite Chinese test on January 2007, that completely destroyed the weather satellite Feng Yun-1C, increasing the total orbital debris population of 25% and the accidental collision between two satellites – the Iridium-33 and the Cosmos-2251 -causing a further population increase of 16%.

As for the re-entry risk, when a spacecraft lifetime decays, the orbit of the object and the orbit of the Earth collide. Smaller debris does not represent a serious threat, because of their reduced size, in fact they are vaporized by the friction with the atmosphere. However, larger objects may re-enter in the atmosphere and there is a small but definitely not negligible chance that they land in an inhabited area. For instance, last year,

the re-entry of the Chinese space station Tiangong-1 aroused great interest worldwide and was constantly monitored in the first months of the 2018.

From the situation described above, the necessity to monitor and catalog the population of the space debris is of the utmost importance for space situation awareness. Mitigation guidelines for space debris include:

- the monitoring and observations of the resident space objects using radar and optical sensors from ground as well as from space, for performing collision avoidance;
- the development of new spacecraft which, in the event of a break-up, will be divided into as few pieces as possible, minimizing a further increase in debris population;
- the study of the so called Active Debris Removal (ADR), a number of methods aimed to the disposal of the useless orbiting objects.

Regarding collision avoidance procedures, they represent an important mitigation measure but they require an accurate knowledge of the state of the orbiting objects. Within this framework, space-based and ground-based measurements have been used to monitor the SD situation at various altitudes [4]. Regarding ground-based measurements, a network of dedicated sensors (i.e. radars, telescopes and lasers) is necessary for surveillance and tracking of space debris. Optical sensors are typically used to detect and track space debris at higher orbits, e.g. Medium Earth Orbit (MEO), between 2000 and (below) 35786 km of altitude, and Geosynchronous Equatorial Orbit (GEO), at 35786 km of altitude, whereas radar sensors are employed at lower altitudes (LEO) [5].

Radar sensors are an essential part of the worldwide resident space debris monitoring program, named Space Situational Awareness (SSA) programme, and they are spread all over the world. The United States are the most exhaustive source of information about orbital objects. Thanks to the Space Surveillance Network (SSN), an extensive network of optical and radar sensors, the United States Strategic Command (USSTRATCOM) is able to hold and maintain the largest database of catalogued objects in LEO [6]. The SSN radar sensors are comprised of phased arrays, reflector antennas, multi-static fences, and other types of radar that do not fall under the canonic SSN network, but are hosted by the US and could provide useful SSA data [7]. A detailed list of US SSN sensors is reported in [8]. The US Joint Space Operations Center (JSpOC) acts as coordinator for the large amount of data coming from the SSN, elaborating the orbital parameters and making them available in a suitable format, i.e. the Two-Line Element set (TLE) [9].

After the US, Russia holds the second most important radar network for this application. It is based, for the most part, on inactive missile warning systems, distributed across the former USSR. Among the Russian radar network, it is worth mentioning a few of them. The two Daryal-Radar located in Pechora (Russia) and Gabala (Azerbaijan), are both phased array in a bi-static configuration, working in VHF range (150-200 MHz) and capable of transmitting up to 350 MW [7, 8]. The same configuration is used by the Volga-type radar in Baranivichy (Belarus), operating at 3 GHz and by the Don-2N radar (also known as Pill Box) located in Moscow [7].

Unfortunately, there is very limited information about the radar sensors owned by the People's Republic of China. From the poor data found in the web, it can be stated that the Chinese Space Surveillance System (CSSS) radar sensors are, for the majority, phased arrays and some of them might be located in Xuanhua, Zhangjiakou (Hebei province) and Xinjiang [8].

Given the relevance of the space debris issue, also Europe has started a space surveillance program. Following the steps of the USSTRATCOM, the European Space Agency (ESA) created the Space Surveillance and Tracking segment (SST) within the SSA European program, focused on the creation of its own catalogue of orbiting objects.

Europe can count on a large network of radar sensors, likewise USA and Russia. The European Incoherent Scatter Scientific Association (EISCAT), for instance, is a radar system composed by three separate sites [10]: the monostatic VHF radar, located near Tromsø (Norway), which operates at 224 MHz; the monostatic double antenna EISCAT Svalbard radar, located in Longyearbyen (Svalbard), which operates at 500 MHz; and the tristatic UHF EISCAT radar operating at 930 MHz, with transmission site located in Tromsø and receiving sites located also in Tromsø, Kiruna (Sweden) and Sodankylä (Finland). All the EISCAT transmitters are able to supply a peak power of the order of magnitude of Megawatts, with a duty cycle of about 10-20%.

Other important radar facilities for space debris observations can be found in Germany, France, Spain and Italy. Germany has at its disposal a powerful bi-static radar consisting of the FGAN Tracking and Imaging Radar (TIRA), located near Bonn, as a transmitter, and the Max-Planck-Institute Effelsberg Radio Telescope as a receiver [11]. In this configuration, the system can transmit 1-2 MW peak power pulses in L-Band, allowing the detection of objects with size down to 1 cm. In the next future, the German Space Administration (DLR) will include the German Experimental Surveillance and Tracking Radar (GESTRA) [12] among the active radar sensors. GESTRA is a close-monostatic pulsed phased array working in L-band (1280-1400 MHz), able to perform digital beamforming.

On the French side, remarkable radar facilities for SD are the Grand Réseau Adapté à la Veille Spatiale (GRAVES), a military continuous wave (CW) bi-static phased array radar operating at 143.05 MHz, located in Dijon [13] and the ARMOR, a mono-pulse C-band system with 1 MW peak power [14] located on the missile range instrumentation ship “Monge”.

The Spanish Space Surveillance and Tracking (S3T) system is currently equipped with two radars: the Monostatic Space Surveillance Radar (MSSR), a close-monostatic L-band radar, located in the Santorcaz military naval base, and the new S3T Surveillance Radar (S3TSR) [15].

In the United Kingdom, in 2010, the Chilbolton radar, a fully steerable 25-m dish antenna working in S-band (3 GHz) with a peak power of 700 kW, located near Winchester (Hampshire), was converted, for SST purposes, in the Chilbolton Advanced Satellite Tracking Radar (CASTR). These features allow the CASTR to efficiently detect objects with Radar Cross Section (RCS) greater than 0.5 m^2 in LEO [16].

Finally, in Italy, the main radar sensor completely dedicated to the SD observations is the Bi-static Radar for LEO Survey (BIRALES). The transmitting antenna of this system is the Radio Frequency Transmitter (TRF), handled by the Italian Air Force. The receiver is the Northern Cross Radio Telescope, located in the Medicina Radio Astronomical Station, near Bologna, in Northern Italy. This system is used for monitoring the space environment in survey mode. The receiver exploits a multi-beam configuration that provides, along with the available measurements, i.e. Doppler shift, illumination time and measured power intensity represented by signal-to-noise ratio (SNR), an estimate of the angular track of the transiting object in the receiver field of view obtained from the analysis of the beam illumination sequence. This innovative configuration allows the sensor to perform initial orbit determination [17]. In its actual configuration, BIRALES is capable of detecting objects as small as 0.01 m^2 [18].

In this framework, more recently, the Sardinia Radio Telescope (SRT) has been employed in the European space debris monitoring project [19]. The SRT is a fully steerable wheel-and-track 64-m dish, located near Cagliari (Sardinia, Italy), devoted mainly to radio astronomical observations and capable to observe the sky in a wide frequency range, i.e. from 0.3 to 116 GHz. The azimuth and elevation maximum speeds, 0.85 deg/s and 0.5 deg/s respectively, allow to follow objects travelling in LEO (with typical angular speed < 0.1 deg/s [3]), making the radio telescope suitable for tracking purposes.

In April 2014 [19], the first beam parking experiments with the SRT used as a receiver in a P-band (410 MHz) bi-static Doppler radar configuration, named Bi-static Radar for LEO Tracking (BIRALET), have shown that the radio telescope could be a valuable resource in the European Space Agency (ESA) space debris monitoring

segment. In these experiments, the transmitter consisted in a small, large-beam width, sector antenna named Flight Termination System (FTS), with about 13 dBi gain. The signal transmitted was a Continuous Wave (CW) with 4 kW power. Within this configuration, the BIRALET system allowed to detect the echoes of objects in LEO with a RCS of about 0.03 m^2.

The measurement campaign of April 2014 [19] can be considered a first test of the capabilities of the SRT as a receiver in a bi-static configuration for space debris monitoring purposes. The results of this campaign can be considered encouraging, since the SRT is a powerful instrument, even if compared to the other Italian cornerstone of the space debris monitoring, the Northern Cross. In fact, the SRT can count on a higher effective area with respect to the Medicina array. This works in favor of the overall sensitivity of the radio telescope, which, on equal terms of operating frequency and transmitted power, is able to detect smaller and/or more distant objects.

During the experiments of April 2014 [19], the receiving chain of the P-band was simply connected to a spectrum analyzer. This choice was dictated by the lack of opportunities available at that moment of the experiment, since no space debris dedicated back-end was available, and using an existing radio astronomical back-end was not a reasonable option for the reasons mentioned above. However, the spectrum analyzer employed during the experiment, being not a state-of-the-art instrument, can be characterized by technical limitations, i.e. the speed of the frequency sweep tied to the Resolution Bandwidth (RBW) selected, the poor processing capabilities, and the missing information due to the “blind time” during the calculations (sampling time). Considering that the typical passage time of a debris in LEO inside the beam of the SRT (in the P-band) can be lower than 500 milliseconds [19], using a non-performing detector may lead to an impairment in the identification of the echo. A step ahead from the described scenario was the planning and the realization of a new receiving chain for the P-band receiver, in order to make it suitable for space debris measurements, reducing the global observation bandwidth, limiting the RFI problem, and developing a dedicated back-end.

1. The Sardinia Radio Telescope: main characteristics and applications

The SRT is a fully steerable wheel-and-track multiple-reflectors antenna used mainly for radio astronomical applications (see Figure 2). It is located 35 km Northeast of Cagliari, in Pranu Sanguini (Lat. 39.493072°N - Long. 9.245151°E), at an altitude of about 650 meters above sea level.

The first work on the telescope started in 2002, but the SRT saw its first light in August 2012. The telescope has a primary mirror of 64-meter, a dish which makes the antenna the largest radio telescope in Italy and one of the largest in Europe. The system can operate, with a radiation efficiency of about 60 percent, in the frequency range from 0.3 to 116 GHz. The main SRT purpose is the scientific research in the radio-astronomical field but a fraction of its employment is devoted to the spacecraft monitoring (such as space debris). Together with the radio telescopes located in Noto and Medicina, the SRT constitute the Italian Very Long Baseline Interferometer network (VLBI).

Figure 2 - Picture of the Sardinia Radio Telescope (SRT) in a typical measurement campaign.

Currently, four receivers are available, covering a portion of P-band (305-410 MHz), L-band (1300-1800 MHz), C-band (5.7-7.7 GHz) and K-band (18-26.5 GHz) [20]. New receivers are currently under development. The SRT is a Gregorian configuration system with the primary parabolic mirror and the secondary mirror diameters of 64 and 7.9 meters, respectively. In addition, the telescope is equipped with a Beam Waveguide system (BWG) which includes two 2.9-m mirrors and one 3.9-m mirror, for a total of four additional focal positions [20]. One of the features of the SRT is the active surface system that permits the modification the profile of the primary mirror (by means of an electro-mechanical control) in order to compensate for deformations caused by gravitational loads, pressure of the wind and thermal gradients [21]. The SRT can be pointed from 5 to 90 degrees in elevation and from -270 to 270 degrees in azimuth, with a rotational speed of 0.5 and 0.85 degrees per second, respectively. Table 1 summarizes the main characteristics of the radio telescope.

1.1 Mechanical structure

The SRT is an impressive structure with a height of about 70-meter and a weight around 3000 tons. For these reasons the telescope is installed on reinforced concrete foundations with a diameter of 40-meter and a depth of 6.5 m. The center of the foundations is provided with an octagonal housing for cable routing and bearing installation that allow azimuth movements of the SRT. Figure 3 offers a front view of the SRT structure.

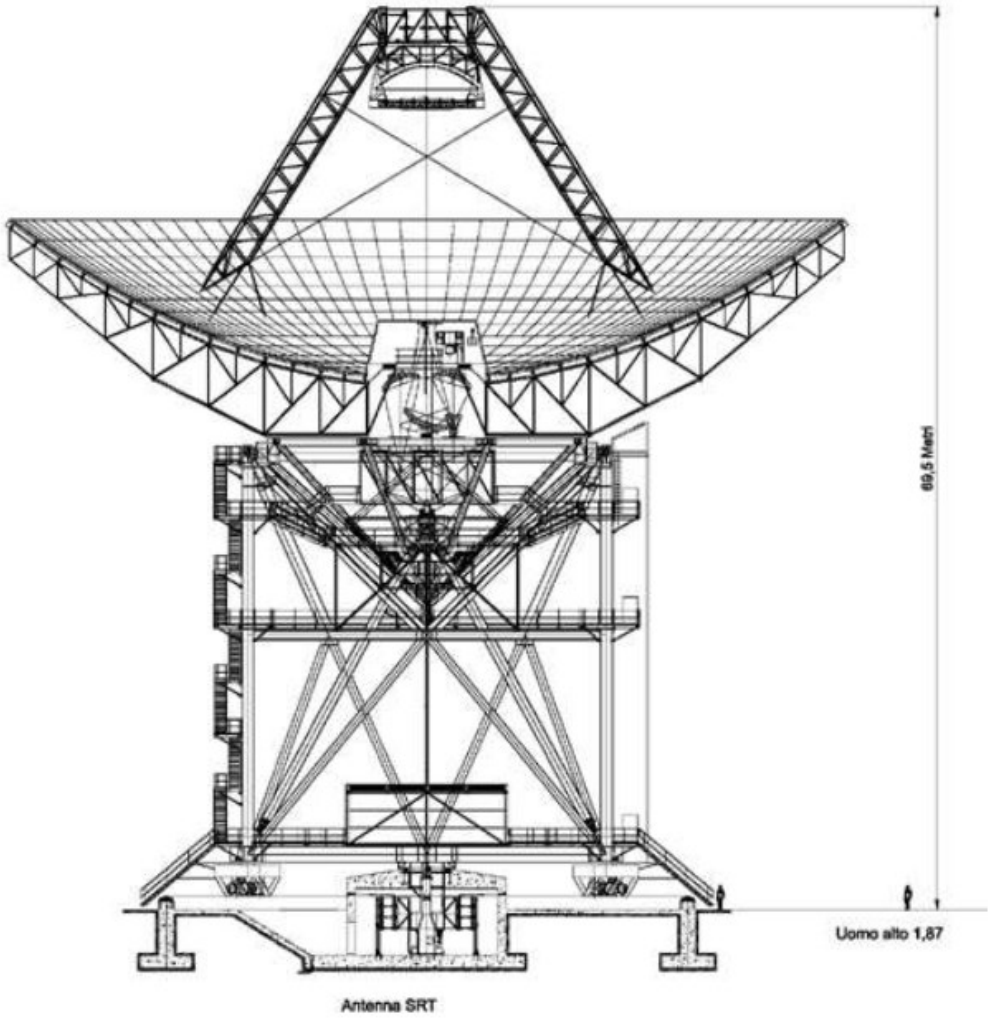

Figure 3- Sketch of the Sardinia Radio Telescope.

The azimuth rotation is possible thanks to a rail built on the foundations. Such a rail has the same diameter of the foundations and it is coupled with them by means of an interface made of a specific concrete reinforced with thin steel rings. The rotation system can count on a total of 16 wheels (4 of them are drive wheels) permitting an angular excursion of ± 270° at a maximum speed of 0.85°/sec. The wheel for elevation pointing is made up of a conical truss frame behind the primary mirror and it permits an angular excursion from 5 to 90 degrees at a maximum speed of 0.5°/sec.

The primary 64-meter dish is composed by 1008 aluminum panels supported by a rear truss frame. The housing for the instrumentation related to the Gregorian focus is located at the top of the primary mirror. The base configuration of the antenna is the Gregorian shaped with a “quasi-parabolic” primary mirror and a “quasi-elliptical” secondary mirror. This configuration guarantees a better illumination of the Gregorian focus, with respect to a standard configuration, creating a zero field zone in the central region of the primary mirror which is obscured by the blockage of the secondary mirror. In this way the field is redistributed in the non-obscured zone, decreasing the standing waves between the feeds at the secondary focus and the sub-reflector. In addition, the shaped configuration allows to under illuminate the sub-reflector edge, reducing the spill-over. This choice, resulting from the combination of the curvature of the primary and secondary mirror, allows the optimization of observations in Gregorian and Beam Wave Guide (BWG) foci.

One of the most innovative and recognizable features of the SRT is the active surface: a total of 1116 electromechanical actuators are currently installed in the back of the primary reflector. The actuators, acting on singular panels, help to compensate every possible surface deformation, such as:

- Gravitational effects, due to the weight of the antenna itself;
- Wind pressure;
- Thermal gradients.

The trussing of the primary mirror supports the secondary one, located at a distance of about 24 m, by means of a quadrupode. The “quasi-elliptical” 8-m sub-reflector is composed by 49 panels supported by a rear truss frame. A primary focus positioner (PFP) allows positioning different feeds at the primary focus. The PFP is anchored to the truss behind the mirror. The overall blockage on the geometric area of the primary mirror, by the sub-reflector, the quadrupode, the cables and the positioner is of about 6%. The correct orientation of the sub-reflector is ensured by 6 electromechanical actuators, 3 along the z-axis (the same axis of the primary reflector), 1 along x-axis (parallel to the elevation axis) and 2 along the y-axis (perpendicular to x-axis).

One important parameter is the pointing error accuracy, which is tied to the frequency and, thus, to the antenna beam. The higher the frequency, the smaller the beam and the better the accuracy should be. The pointing error is expressed as it follows:

$$\delta_p \leq \frac{HPBW}{10}$$

where HPBW stands for Half-Power Beam-Width, the width of the beam corresponding to –3 dB (half of the total power) in the main lobe. The causes for the pointing error are:

- Systematic errors of the mechanical and electromagnetic alignment of the structural parts and the feeds;
- Non-systematic errors, due to the pressure of the wind and the thermal gradients.

Typically, systematic errors have high values, in the order of few arc minutes. However, such errors can be evaluated by means of astronomical observation campaigns of calibration radio sources, and, consequentially, removed. As for non-systematic errors, active error correction techniques are needed in order to remove them. The observations at high frequencies (within the range 22-100 GHz) are possible only during accurate and normal weather conditions.

1.2 Geometric optics

The design of SRT optics has been made in an attempt to obtain the largest number of focal position in the available space. The availability of several operating foci allows greater freedom in the selection of the receivers to be used.

There are three main operative areas, for a total of 6 focal positions. With reference to the schematic of the focal positions of the SRT reported in Figure 4, the focal positions are:

- Primary focus (F1);
- Gregorian focus (F2);
- Beam Wave Guide (2 x F3, 2 x F4).

The Gregorian configuration permits the use of the parabolic mirror focus without the necessity to move the secondary mirror. In order to use the primary focus, the antenna design includes the PFP, that supports different receivers. The PFP consists of a structure rotating around one of the transverse axes of the sub-reflector. Once extended, the latter can place the feeds in front of the secondary reflector, by the primary focus. In this way, by means of the translation movement along the same rotation axis, it is possible to choose the receiver suitable for the observation, and, by means of the movement along the z-axis, it is possible to hold the optical focal position.

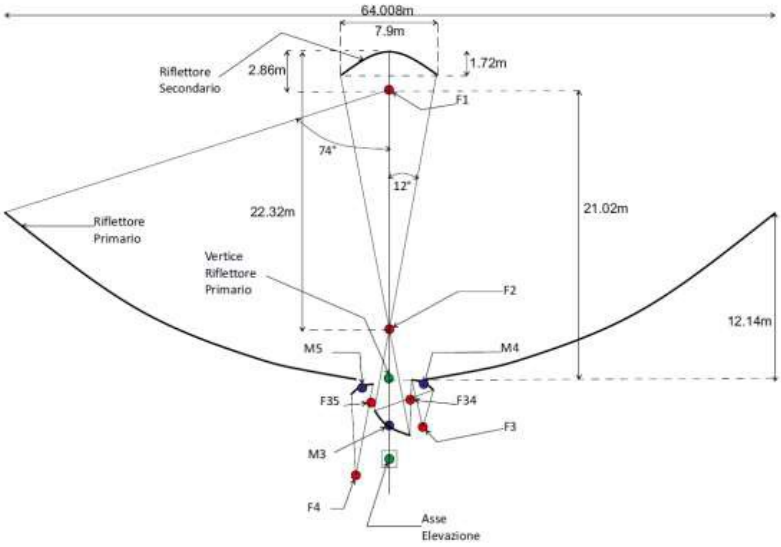

Figure 4 - Focal position of the Sardinia Radio Telescope.

As shown in Figure 4, the focal length of the primary mirror is about 21 meters, resulting in a ratio F1/D ≈ 0.33. The suitable operating frequencies range for the receivers at focal position are in the range 0.3-22 GHz. Moreover, the simultaneous usage of the couple of frequencies 2 and 8 GHz is possible thanks to a coaxial receiver, employed primarily for geodynamic purposes. The Gregorian focus is located 3.5 m above the reflector vertex. By this point, an observational structure provided with an off-axis cylindrical rotating system, capable of hosting up to 8 receiving systems, is present. It is possible to select the feed to be placed in correspondence of the focal area through the rotation around the cylinder axis. The secondary mirror, thanks to its elliptical geometry, produces a magnification i_2 that depends on the ratio between its focal length and its distance from the first focus (about 20 meters and 3 meters respectively, in this case). The complete focal calculation is herein reported:

$$i_2 = \frac{20.32}{2.85} \approx 7.13$$

$$F_2 = i_2 \cdot F_1 \approx 149.87\ [m]$$

resulting in a ratio F2/D ≈ 2.34. The operating frequencies for this focal position range from 7.5 to 100 GHz. The BWG foci are located beneath the primary reflector vertex. The housing for these foci, as well as for the Gregorian focus, is a three-floor structure. The top floor of this structure host the instrumentation for the Gregorian focus observations. The lower floors host a combination of 5 "quasi-elliptical" mirrors, a mobile one, in the central position and the others fixed and divided in couples. The central mobile mirror, called M3 and facing upwards, receive the beam directly from the Gregorian focus, and has a diameter of about 4 meters. The four fixed mirrors are labeled M4 (A & B), with a diameter of 3 meters, located above M3 on the right side, and receiving its reflected beam, and M5 (A & B), also with a diameter of 3 meters, located above M3 on the left side, and receiving its reflected beam. Although the elliptical mirrors have similar size, they have different radii of curvature and eccentricity. In this way they can offer different focal positions, a longer one for the M5 couple and a shorter one for the M4 couple. In order to calculate the focal positions for each couple, it is necessary to find the magnification of M3 and then the magnification of the next mirror depending on the couple, M4 and M5 respectively. In formulas, for the M4 mirror (focal length 3.6 m) we can translate this in:

$$i_3 = \frac{2.4}{7} \approx 0.34$$

$$i_4 = \frac{3.6}{2.1} \approx 1.71$$

$$i_{tot} = i_2 \cdot i_3 \cdot i_4 \approx 4.19$$

$$F_3 = i_{tot} \cdot F_1 \approx 183.91\ [m]$$

resulting in a ratio F3/D ≈ 1.38. Whereas for the M5 mirror (focal length 7 m) we have:

$$i_5 = \frac{7}{2} \approx 3.5$$

$$i_{tot} = i_2 \cdot i_3 \cdot i_5 \approx 8.56$$

$$F_4 = i_{tot} \cdot F_1 \approx 179.87\ [m]$$

resulting in a ratio F4/D ≈ 2.81. However, the overall accuracy of the BWG, primary and secondary mirrors allow the use of the BWG foci up to 32 GHz. A summary of the focal position of the SRT is reported in Table 1.

Table 1 - Sardinia Radio Telescope foci.

FOCUS	MIN FREQUENCY [GHZ]	MAX FREQUENCY [GHZ]	F/D
F1	0.3	22	0.33
F2	7.5	116	2.34
F3	1.4	32	1.38
F4	1.4	32	2.81

1.3 Front-end

The SRT is designed to continuously cover the frequency range 0.3-116 GHz. All the receivers installed on the SRT (except the P-band) are super-heterodyne type, allowing the transformation of a high frequency signal to an intermediate frequency signal (IF), by means of a mixer and a local oscillator. All the receivers are cryogenically cooled to ≈ 20 K by a closed-cycle cooling system. The lower operating bandwidth of the SRT (0.3-3 GHz) is polluted by many radio frequency interferences (RFIs), and many filtering stages are present in the receiving chains within this interval, as a result. For each operating frequency, a total of 4 instantaneous IF bandwidths are available: 150 – 450 – 1000 – 2100 MHz.

The receivers installed on the Gregorian or BWG foci use a double down-conversion. Figure 5 shows a general schematic of the front-end chain. The feed is usually a corrugated horn that couples the incoming electromagnetic radiation propagating in free space from the antenna to the transmission line. The directional coupler injects a signal for the calibration of the receiving chain in front of a polarizer. The polarizer converts two orthogonal linear polarizations in right-handed and left-handed circular polarization. This is achieved by phase shifting 90° one polarization signal with respect to the other. The Ortho-Mode Transducer (OMT) separates the two polarization channels, which are the amplified by an amplification block composed by one or more Low Noise Amplifiers (LNA). From this point the signals are, eventually, donw-converted and sent to the back-end.

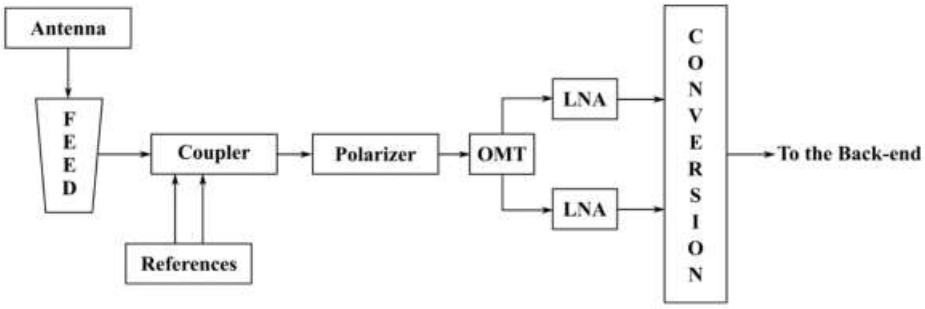

Figure 5 - Block diagram of a general front-end of the Sardinia Radio Telescope.

In general, the connections between the foci of the SRT regards three different types of signal:

- Local Oscillator (LO); in order to reduce the cost of the design and the construction of a high number of separate super-heterodyne receivers, completely independent, a very common solution involves the sharing of some LOs (at least one for one of the two conversions, for instance). In this way, a single LO can serve multiple receivers, through a signal distribution system.
- IF; the RF signal coming from the antenna have to be down-converted and sent to the back-end using the same analog fiber optic links which are shared by all the receivers
- Reference; the reference signals (5 MHz, 10 MHz and 1 pulse per second) are used for phase-locking the receivers to a common maser source located near the telescope.

All the signals are transported through coaxial cables connections and optical links that connect the antenna to the control and back-end rooms.

The receivers installed in the Gregorian and BWG foci employ the same two LOs (one for each channel) located in the Gregorian focus, using distribution systems named OLD. The disequalization resulting from the

use of coaxial cables over long distances is compensated by using specially designed amplifiers (known as AmpEq). The reference signals are necessary to the calibration of the receivers, and, once again, they are distributed by means of coaxial cables.

1.4 Efficiency and System Temperature

Being the SRT an instrument mainly employed for radio astronomy purposes, a very common representation of the antenna gain is the following:

$$G = 10^{-26} \frac{m\eta_a A_g}{k_B} \left[\frac{K}{J_y}\right]$$

where m accounts for a completely non-polarized radiation and is equal to 0.5, Ag is the geometric area of the antenna, kB is the Boltzmann's constant and ηa is the antenna efficiency. G is expressed in Kelvin per Jansky, where the Jansky is 10^{-26} W/m^2·Hz in the International System. The latter term takes into account every possible degradation factor of the received signal that could mostly influence the antenna's overall gain. These contributions are also in the form of an efficiency factor:

- Blockage efficiency ($\eta_{Blockage} \approx [1 - A_{Blocked}/A_{Total}]2 = 0.88$), due to the blockage of the field from the sub-reflector and the supporting structure.
- Surface efficiency ($\eta_{Surface} \approx e^{-(4\pi\delta\lambda)2} = 1 \div 0.35$), the worst case is for the highest operation frequency (116 GHz), as for the shorter wavelength. In fact, the efficiency is determined by manufacturing errors of the panels and to their misalignment. The deformation of the reflecting surfaces, the pressure of the wind, the gravitational effects and the dilatation owed to the thermal gradients contribute to decrease the surface efficiency. A metrology system is under development to reduce the RMS of the surfaces to below 150 μm (λ/20 at 100 GHz) and allow observations at highest frequencies. As already said, to counterbalance these effects the antenna is provided with an active surface system.
- Phase efficiency ($\eta_{Phase} \approx 0.99$), also known as de-focalization efficiency, it is tied to the lateral (axial) shift of the feed from the focus.
- Diffraction efficiency ($\eta_{Diffraction} \approx 0.98 \div 0.86$), that takes into account the losses due to the diffraction on the antenna edges.
- Illumination efficiency ($\eta_{Illumination} \approx 0.9 \div 0.76$), takes into account the amplitude and phase distribution unevenness in the antenna's aperture.
- Cross polarization efficiency ($\eta_{CrossPol} \approx 1$), takes into account the portion of the power radiated with an orthogonal polarization with respect to the nominal polarization of the radiation received by the antenna.
- Spill-over efficiency ($\eta_{SpillOver}$), is the percentage of power radiated by the feed that is intercepted by the reflectors, the rest of the power being radiated outside the reflectors edges; maximizing this term requires to decrease the aperture efficiency. Therefore, an optimum is usually adopted in radio-astronomy applications with tapered illumination (a Gaussian profile), such that the feed's beam is more intense in the center and attenuated at the edges.
- Loss efficiency ($\eta_{Loss} \approx 0.95$), takes into account the attenuation of the signal before the LNA stage.
- Return loss efficiency ($\eta_{ReturnLoss} \approx 0.98$), takes into account the losses due to the reflection of the feed.

The overall efficiency is the product of all these terms.

An important parameter for a radio telescope is the sensitivity, namely the indication of the minimum flux measurable by the system:

$$\Delta S = \frac{\alpha T_{sys}}{G\sqrt{Dfn}N_{IF}}$$

where α is a coefficient (≤ 1), Tsys is the system temperature, G is the gain expressed in K/Jy, Δf is the observation bandwidth, τ is the integration time expressed in seconds, n is the number of observations and NIF is the number of available channels.

1.5 Digital back-ends

The back-end is intended as the set of components that allow the processing of the signal coming from the front-end. At the moment the available back-end at the SRT are:

- The Total Power (TP);
- XARCOS;
- The Digital Base Band Converter (DBBC);
- The Pulsar Digital Filter Bank (DFB);
- The Sardinia ROACH2-based Digital Architecture for Radio Astronomy (SARDARA).

The TP platform was developed by the Institute of Radio Astronomy (IRA) that can work in two different modes: the focus selector mode (see Figure 6) and the continuum back-end mode (see Figure 7).

The TP consist of 14 identical boards, each one manages the Intermediate Frequency signals coming from the three SRT foci. The signal selected by the TP is attenuated (in a range of 0-15 dB) and filtered with one of the following LPF: 100-350 MHz, 100-830 MHz, 100-1300 MHz, and 100-2100 MHz. Three copies of the signal are generated to be processed by the others SRT back-end (described below in this section) and one copy is sent to the TP itself. The signals are then sent to square law detectors and converted in digital format.

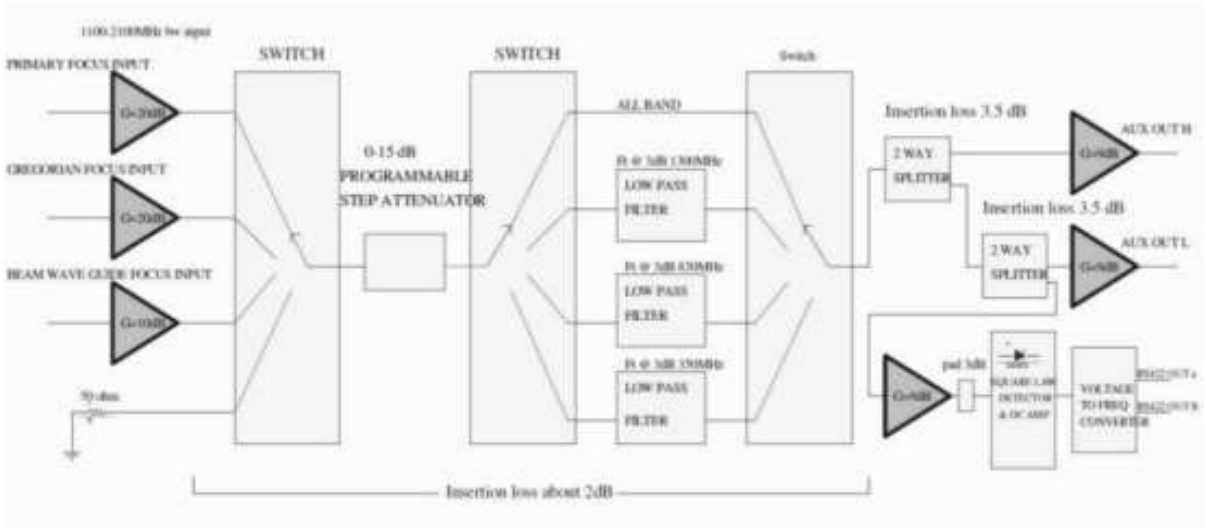

Figure 6 - Schematic of the Focus Selector.

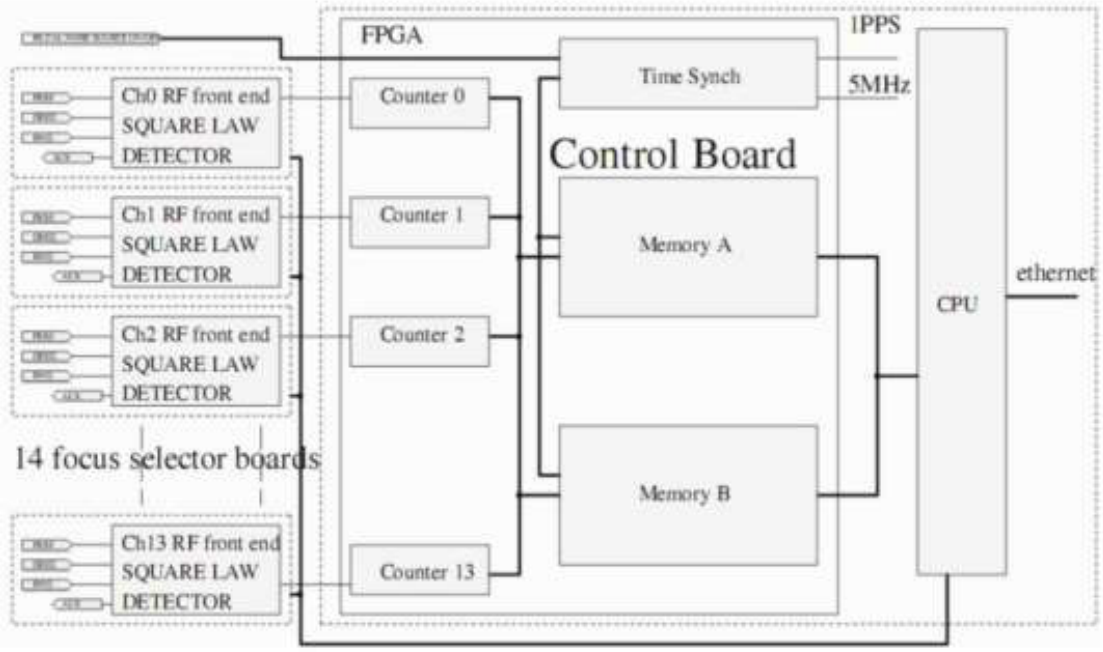

Figure 7- Schematic of the Total Power.

XARCOS is a spectral polarimeter developed by the Astrophysical Observatory of Arcetri (see Figure 8) containing 40 Field Programmable Gate Arrays (FPGAs) and capable of processing up to 16 signals with 125 MHz bandwidth, giving total power a spectralpolarimetric information. The signal from the front-end is amplified in the first stage of the back-end, filtered with BPFs (125-250 MHz), and converted by means of two ADC boards. The real signals are then converted to complex ones and sent to the FFT boars. For each IF, different values of the input bandwidth can be selected: 25 MHz, 62.5 MHz, 31.25 MHz, 15.625 MHz, 7.8125 MHz, 3.90625 MHz, 1.953125 MHz, 0.9765625 MHz and, finally, 0.48828125 MHz. The FFT spectral-polarimeter provides both auto- and cross-correlation products of the left and right circular polarizations. These signals are later integrated for a programmable time, multiple of 10 seconds.

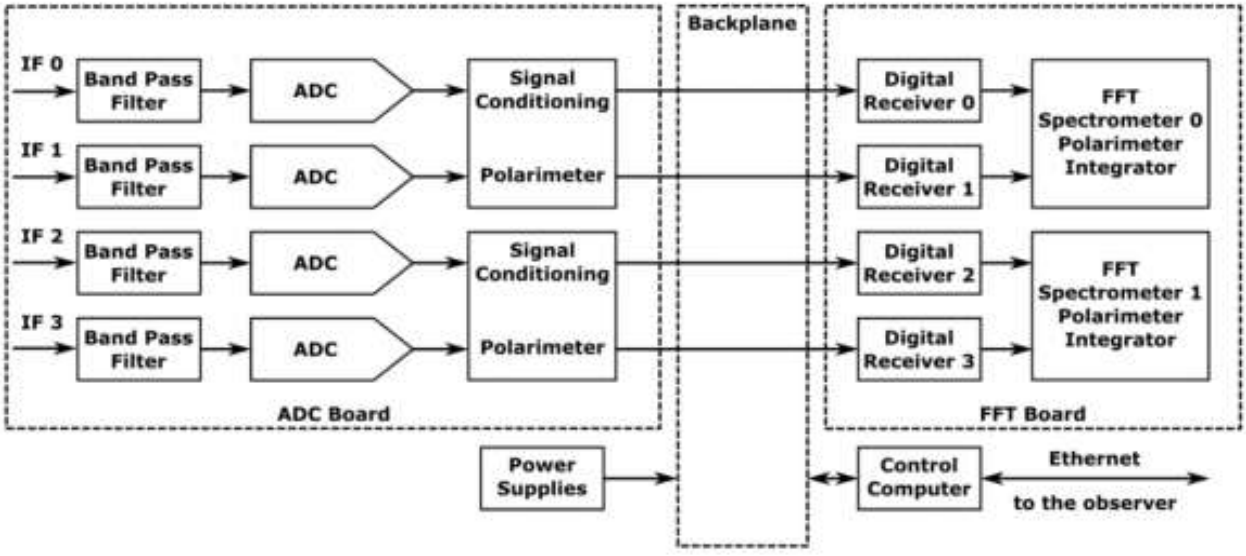

Figure 8 - Simplified schematic of the XARCOS with only 4 inputs.

The DBBC is a project developed by the IRA of Noto and consists of a reconfigurable modular data acquisition platform for radio astronomical applications; Figure 9 shows a block diagram of the DBBC. It is mainly used as a VLBI (Very Long Baseline Interferometry) machine: almost all the stations of the EVN (European VLBI Network) employ a DBBC for VLBI observations. The DBBC has a flexible architecture with more FPGA-based boards that can be stacked together. One of the strengths of the DBBC is that is a complete platform: indeed, it contains a control personal computer, a synthesizer, a digital-to-analog board and, more generally, all that is necessary to make it an independent machine.

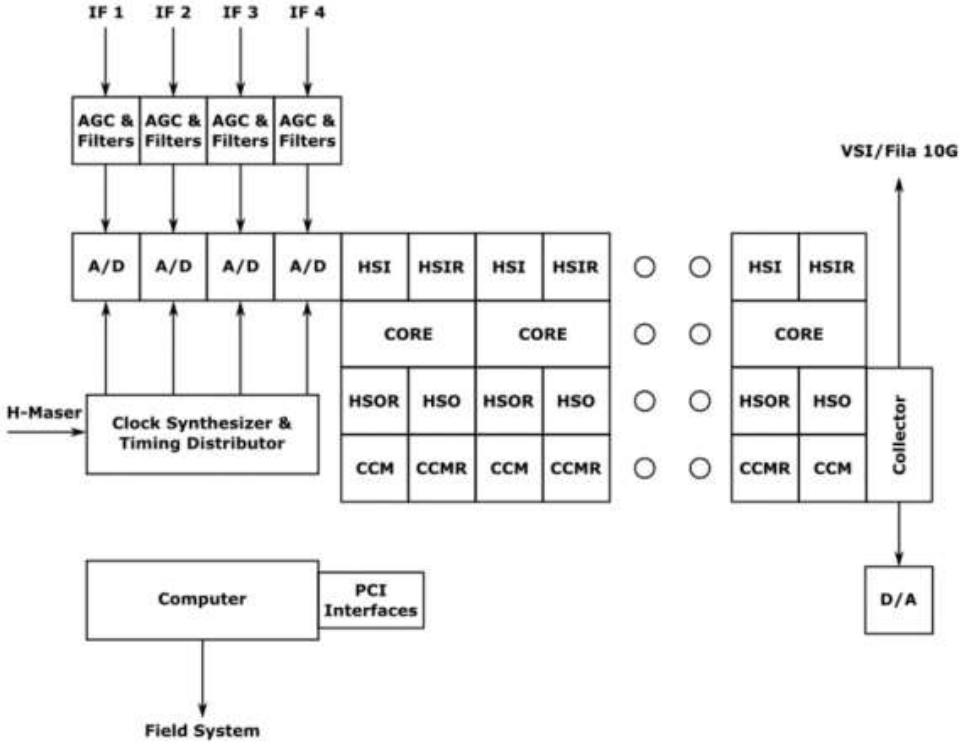

Figure 9 - DBBC architecture.

The DFB is a digital back-end developed by CSIRO-ATNF (Australia Telescope Natural Facility) for continuum and spectro-polarimetric observations. The system is based on four 2048 MS/s 8-bit samplers to detect both polarizations of two frequency bands with a bandwidth of up to 1024 MHz. It provides full Stokes information of two receivers simultaneously. The spectra are computed by FPGAs with polyphase filters which perform an isolation between neighboring channels that are higher than 60 dB. This prevents even strong in-band RFI from contaminating the other detected channels during an observation. A full set of configurations for pulsar and spectro-polarimetric observations is available, although, at SRT it is currently used only for pulsar observations.

SARDARA is the acronym for Sardinia Roach2-based Digital Architecture for Radio Astronomy. The SRT is equipped with a variety of digital back-ends that are applicable to a significant breadth of radio astronomical studies. However, they each present strengths and weaknesses: the Total Power backend is the only back-end capable of providing the entire bandwidth (2.1 GHz) and all 14 IFs, but can be used solely for continuum observations; XARCOS can act as a full-Stokes spectrometer, but 125 MHz - reduced to half because of its far from optimal antialiasing filters - is the widest available bandwidth; the DFB can be used as a spectro-polarimeter as well and with a larger instantaneous bandwidth (1 GHz) than XARCOS, but the system is equipped with only 4 ADCs. As a consequence, we need an infrastructure that can overcome the aforementioned drawbacks. In particular, a possible optimal solution for SRT should provide up to 14 IFs, a

bandwidth of (up to) 2.1 GHz and, more generally, an easier and quicker re-use for any scientific observing mode: this is what SARDARA offers. Figure 10 shows a block diagram of the system. The ROACH2 boards are reconfigurable and suitable for the wide required bandwidth; additionally, we are part of CASPER, namely a consortium where the motto is “hardware and software are open source”. The system consists of seven ROACH2 boards equipped with two 5 GSample/s ADCs and mezzanine cards 10 Gbe SFP+. The eight outputs of the mezzanine cards are used to connect each ROACH2 board to all of the others and to a GPU-based PC, in which a dual port SFP+ 10 Gbe is installed. A 24-port SFP+ 10 Gbe is employed to interface computers with a high-performance data storage unit.

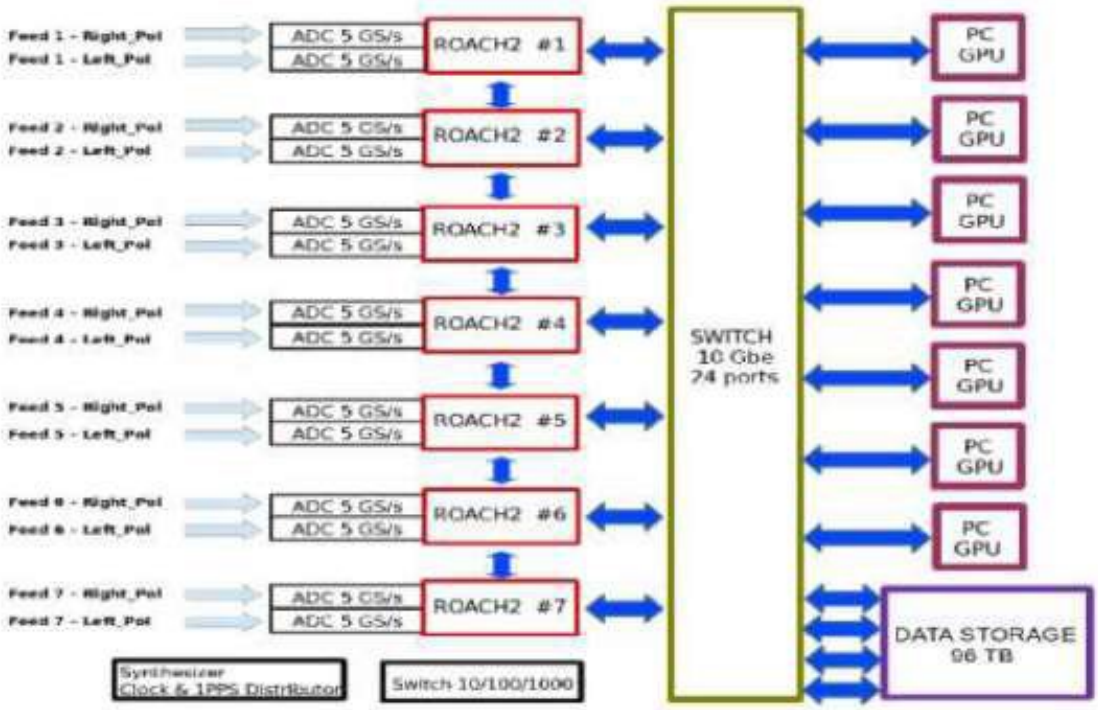

Figure 10 - Block diagram of the SARDARA system.

2. The P-band BIRALET system: Bi-static Radar for LEO Tracking

The acronym BIRALET stands for Bi-static Radar for LEO Tracking and it is a bi-static system, where the transmitter and receiver antennas are separated. When the system was born, in April 2014 [19], it was composed by the Flight Terminator System (FTS) as a transmitter, a small, large-beam-width, sector antenna with 13 dBi gain, owned by the Italian Air Force (AFI) and located inside the Italian Joint Test Range in the region Salto di Quirra (PISQ), at coordinates Lat.39.493068°N – Long. 9.64308°E (Sardinia, Italy). The FTS was composed by a powerful amplifier, capable to supply an averaged and leveled power of 4 kW within the bandwidth 400-455 MHz (P-band). The FTS was always employed in Continuous Wave (CW) mode at 410 MHz and, consequently, this prevented the possibility to directly measure the object range, which was obtained analytically. The receiver was, obviously, the SRT, without a dedicated back-end, but with a simplified acquisition chain where the two channels of the P-band receiver, one for horizontal and vertical polarization, respectively, typically used for radio astronomical measurements, were combined and simply connected to a spectrum analyzer (see Figure 11). In this way, it was possible to see in real time the echo radar with a resolution bandwidth less than 20 Hz, but data processing could be poor, mainly due to the limitations of the spectrum analyzer, i.e. the slow frequency sweep for low resolution bandwidths, thus preventing all data saving in real time.

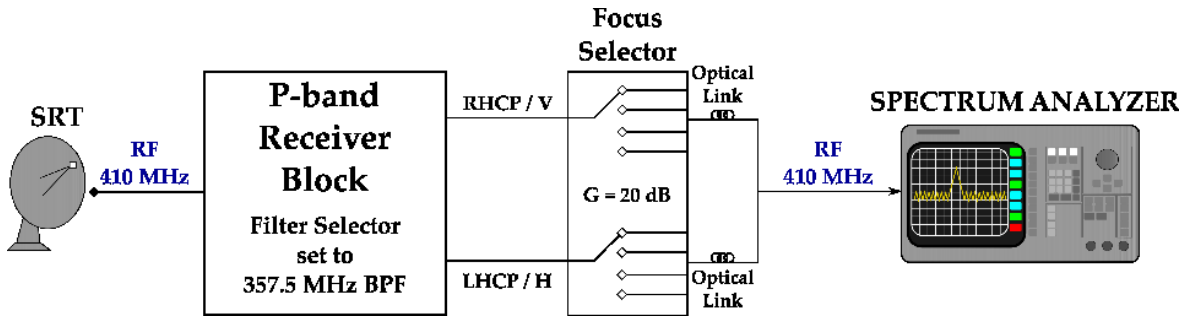

Figure 11 - Simplified measurement setup, used in the first space debris experiment with the SRT, in April 2014.

Compared to the early years when the SRT was used for space debris measurement campaign, the BIRALET system has recently been upgraded with a new transmitter (i.e. the TRF), described in Section 2.1, and with a dedicated channel, for the SRT, developed ad-hoc for space debris monitoring, which comprises a dedicated backend with its acquisition chain. The P-band space debris dedicate channel for the SRT is reported in Section 2.2.

2.1 The Radio Frequency Transmitter of the P-band BIRALET system

The new transmitting antenna of the BIRALET system is named Radio Frequency Transmitter (TRF) and it is located in the region "Salto di Quirra" (Cagliari, Sardinia, Italy), at coordinates Lat. 39.6050°N – Log. 9.4396°E. It is a 7-m fully steerable parabolic antenna with a primary focus configuration. The azimuth and elevation excursion of the antenna ranges from 0 to 360 deg and from 0 to 90 deg, respectively, with an accuracy of 0.1 deg and a maximum speed of 3 deg/s [20]. The system is composed by a set of 7 power amplifiers that allows to supply a maximum RMS power of 10 kW (continuous peak power of 14 kW). The latter are optimized

to work in the frequency range 400-420 MHz, where the TRF has an antenna gain of about 27 dBi and an Equivalent Isotropic Radiated Power (EIRP) of more than 60 dB, and filtered with a tunable central frequency (e.g. 410 MHz) and a bandwidth of 5 MHz. The main features of the TRF antenna are reported in Table 2.

Table 2 - Main characteristics of the TRF transmitter.

ANTENNA NAME	TRF
FREQUENCY	410 MHz
ANTENNA GAIN	27.3 dBi
HALF POWER BEAM WIDTH (HPBW)	7.3 deg
AZIMUTH SPEED	3 deg/sec
ELEVATION SPEED	3 deg/sec

The block diagram of the transmitting system is shown in Figure 12. It is composed by a central control unit (CCU) that takes in input a signal originated by a vector signal generator. The CCU is linked to an Automatic Gain Control (AGC) for the adjustment of the system gain depending on the level of the signal coming from the combiner. The AGC sends the signal to the radio frequency splitter. This block creates seven signals, adjusted in phase, each one for every power amplifier available (with nominal continuous peak power of 2 kW). After the power amplification block, the signals are combined, filtered with a low pass filter and sent to the antenna.

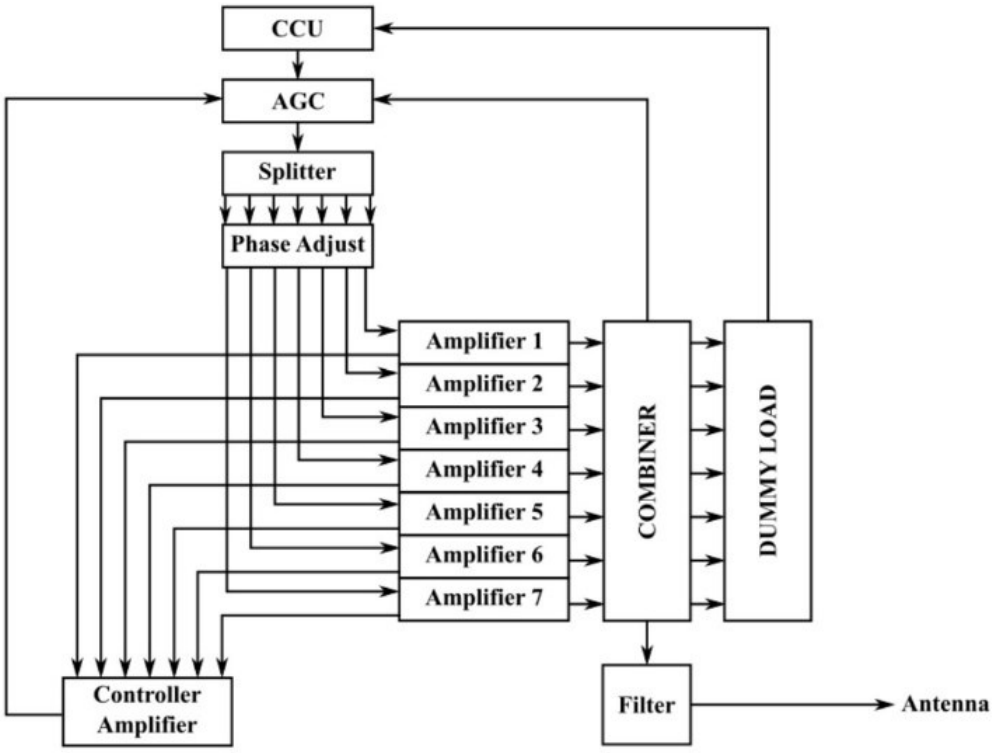

Figure 12 - Block diagram of the transmitting system.

To date, the transmitter has been employed in CW mode and, consequently, this prevented the measurement of the object range, but allows only the Doppler shift and Signal-to-Noise ratio (SNR) received measurements.

2.2 The Sardinia Radio Telescope as a receiver in the P-band BIRALET system

The receiver for the BIRALET system is the SRT, a flexible instrument for radio astronomy studies and space science. As described in Section 1, the antenna is a quasi-Gregorian system with a 64-meter parabolic primary mirror and a 7.9-meter elliptical secondary mirror. It has three other mirrors (two with a diameter of 2.9 m and one with a diameter of 3.9 m), which provide the Beam Wave-Guide (BWG) system. The radio telescope is characterized by six focal position: the primary focus named F1, the Gregorian focus named F2, and the beam wave-guide foci named 2xF3 and 2xF4. The azimuth and elevation maximum speeds, 0.85 deg/s and 0.5 deg/s respectively, allow to follow objects travelling in LEO (with typical angular speed < 0.1 deg/s [3]), making the radio telescope suitable also for tracking purposes. The sketch of the SRT is show in Fig. 2 and the antenna features are summarized in Table 3.

Table 3 - Characteristics of the SRT.

OPTICS	**GREGORIAN (SHAPED) + BWG**
FOCAL POSITIONS	Primary: f/D = 0.33 Gregorian: f/D = 2.34 2 x BWG I: f/D = 1.38 2 x BWG II: f/D = 2.81
FREQUENCY RANGE	0.3 – 116 GHz
PRIMARY REFLECTOR DIAMETER	64 m
SECONDARY REFLECTOR DIAMETER	7.9 m
BWG MIRRORS DIAMETER	2.9 – 3.9 m
AZIMUTH AND ELEVATION SPEED (WIND SPEED < 60 KM/H)	0.85 °/sec (Az) 0.5 °/sec (El)
ANTENNA GAIN AT 410 MHZ	46.6 dB
ANTENNA EFFICIENCY AT 410 MHZ	57.7%

The SRT is one of the largest radio telescopes in the world equipped with an active surface system [21]. A total of 1116 electro-mechanical actuators can control the 1008 aluminum panels of the primary mirror, supported by a rear frame. The actuators help to compensate for possible undesired deformations of the primary mirror surface, due to gravitational loads, pressure of the wind, and even thermal gradients.

The P-band receiver of the SRT, used for space debris monitoring in the BIRALET system, is installed in the primary focus of the antenna (Figure 13). The receiver is a cryogenic dual-band coaxial-feed, that simultaneously covers the frequency range of 305-410 MHz (P-band) and 1.3-1.8 GHz (L-band). The section view and the photo of the P-Band receiver coaxial feed is shown in Figure 14. The simulated (CST Microwave Studio) radiation pattern of the P-band feed at 410 MHz is reported in Figure 15. The primary focus has a feed edge illumination of ± 74°. The feed gain is 10.4 dB, the cross-polarization is -31.4 dB and the edge taper at 74° is about -17 dB.

The electromagnetic coupling between the P-band feed system and the SRT has been simulated using the 3D analysis software GRASP (by TICRA) in order to estimate the antenna performance. In the GRASP model we have taken into account both the blocking effects of the sub-reflector (simulated with a hole on the primary mirror reflector, equivalent to the secondary mirror aperture) and the quadrupod. The simulated antenna efficiency is 57.7% and the resulting radiation pattern of the SRT is reported in Figure 16, showing a gain of 46.6 dB, a cross-polarization of -33.1 dB, and a HPBW of 0.86 degrees at 410 MHz [22].

Figure 13 - Picture of the L-P cryogenic receiver (red circled) installed on the SRT primary focus.

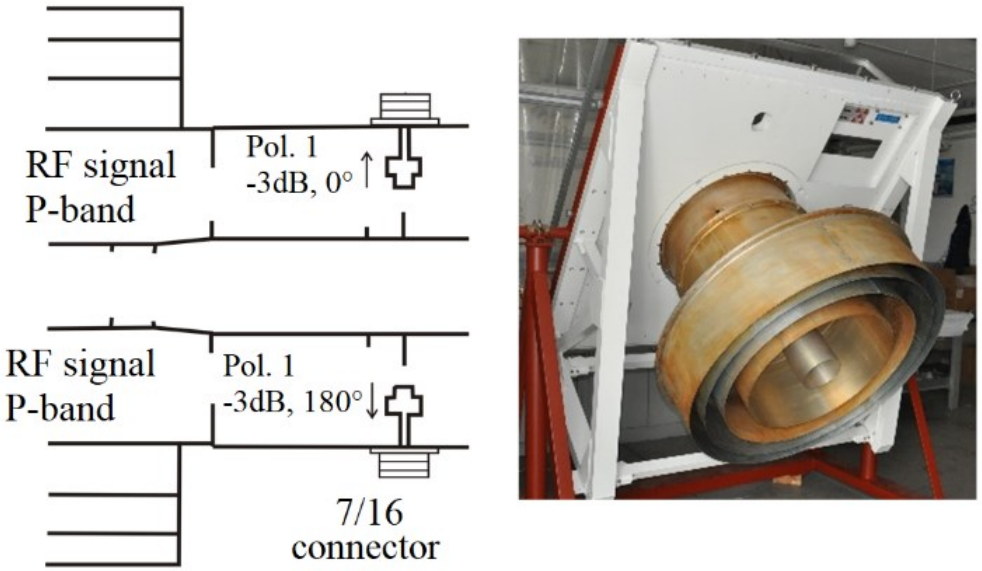

Figure 14 - Section view and photo of the P-band feed.

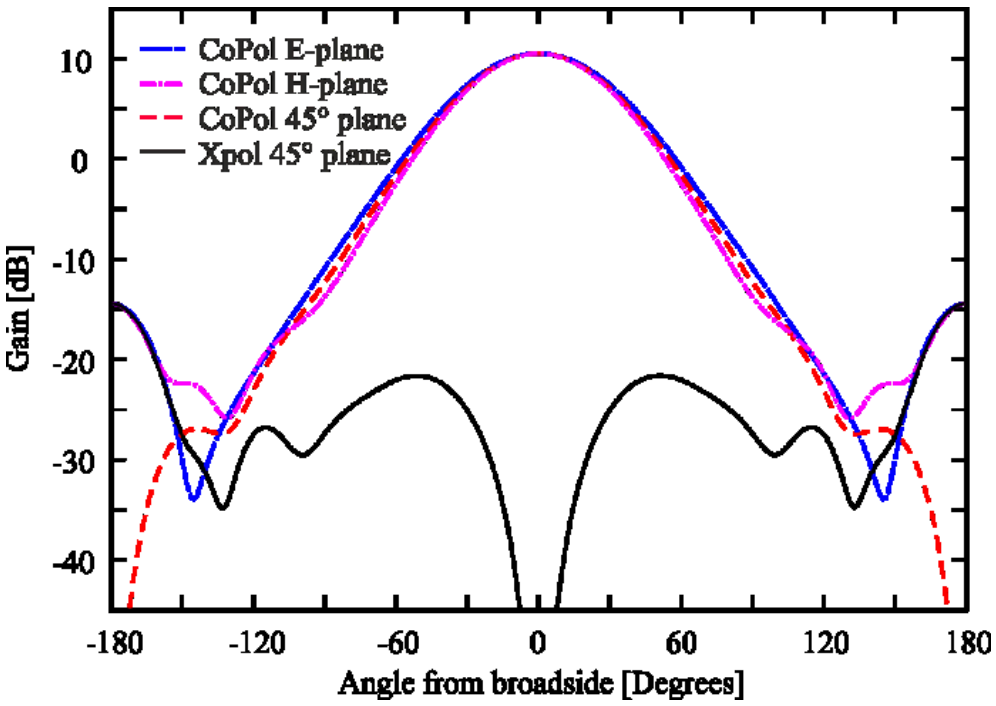

Figure 15 - Radiation pattern of the coaxial feed at 410 MHz.

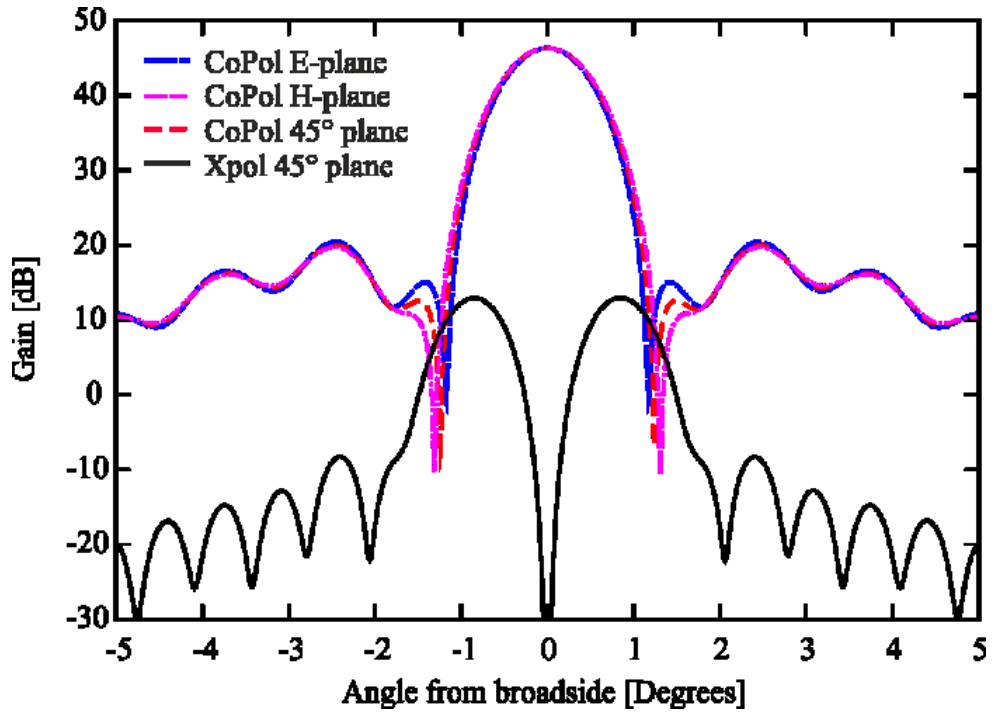

Figure 16 - Radiation pattern of the SRT at 410 MHz.

The original schematic of the P-band receiver is shown in Figure 17 [22]. Four main blocks can be identified: the Cryogenic Front-End (CFE), the linear to circular polarizer, the noise calibrator and antenna unit injection, and the filter selector. The coaxial feed receives the Radio Frequency (RF) signal between 305 and 410 MHz, then a coaxial ortho-mode junction splits each polarization into two equal amplitude signals, 180° out of phase. These two signals are sent to the CFE block through two distinct equi-phase cables and then

recombined with a 180 degrees hybrid. The CFE block is directly connected with the Noise calibration and Antenna Unit injection block for the calibration of the whole system. The output signals from the CFE enter in the P-band Linear to Circular Polarizer block. This block allows to keep the linear polarizations of the two signals but at the same time to collect them in circular polarization (RHCP and LHCP). The last block is the P-band Filter Selector block, which allows the choice of a suitable filter for the radio astronomy observation [22].

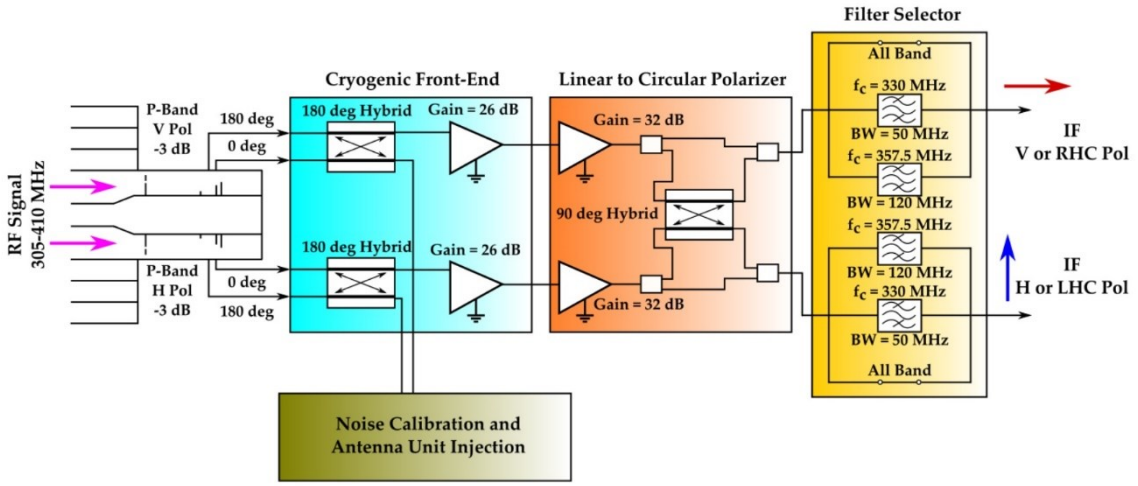

Figure 17 - Schematic of the P-band receiver block of the SRT.

2.3 A P-band space debris dedicated channel for the Sardinia Radio Telescope

Given the speed of the objects traveling in LEO, which ensures that a piece of debris remains in its orbit despite the Earth's gravitational attraction, the passage inside the beam of a radio telescope at the microwave frequencies can be very quick, i.e. some seconds tops [18]. Therefore, a good responsivity of the measurement and recording system is a priority for the SD monitoring. As described above, during the first experiments on April 2014, the two channels of the P-band receiver, one for each polarization, typically used for radio astronomical measurements, were simply connected to a spectrum analyzer. This measurement setup is shown in Figure 11. After the P-band receiver block, before the signal reaches the Spectrum Analyzer, it goes through the Focus Selector, composed by a set of amplifiers, variable attenuators and filters. This system is used to select the focus of the SRT, depending on the type of observation, and is characterized by an overall gain of about 20 dB. Finally, an optical link is used, in order to transfer the RF signal from the P-band receiver to the shielded room of the SRT radio astronomy station, wherein all the back end used by the SRT are installed. The distance covered by the optical link, which is composed by an initial RF-optical transducer, the optical fiber and a final RF-optical transducer, is of about 500 m, with a negligible total loss.

The downsides of the above setup are mostly tied to the wide frequency band and to the poor processing capabilities. The latter can be avoided by storing the entire bulk of raw data deriving from the observation, to allow a post-processing elaboration. A commercial System-on-a-Chip (SoC) FPGA Board, such as the Red Pitaya board, can perform this task. Other than that, from the spectrograms reported in [18], it is rather clear that the operating bandwidth of the P-band receiver is plagued by many RFIs. For this reason, but also to reduce the overall bandwidth, multiple filtering stages have been introduced throughout the entire receiving chain. The schematic of the new dedicated channel for SD monitoring of the SRT is shown in Figure 18. The

main blocks that compose the new channel are the P-band receiver block, the down-conversion block and the Back End. Each block is described in detail in the following sub-sections.

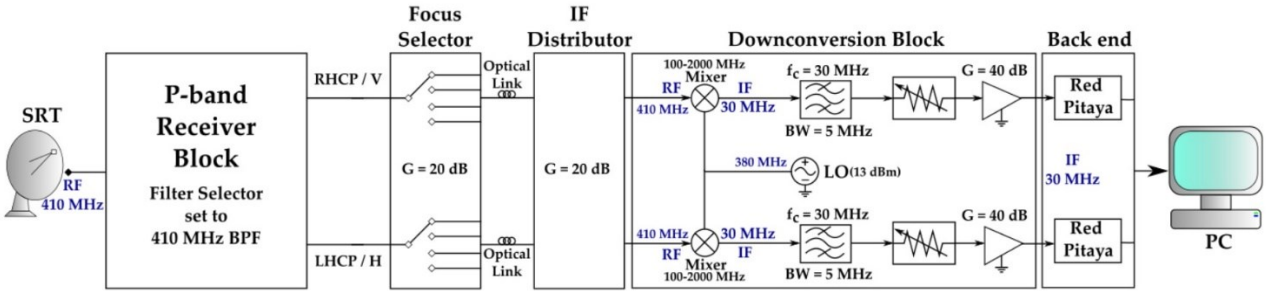

Figure 18 - Schematic of the SD dedicated channel.

2.3.1 P-band receiver modifications

The main modification applied to the P-band receiver (reported in in Figure 17 and indicated as P-band receiver block in Figure 18) has been the insertion of two tubular 99.06 x 31.75 x 31.75 (mm) Band Pass Filters (BPF), model 3B110-410/T15-O/O from K&L, centered at 410 MHz, with 16 MHz bandwidth and 1.1 dB of insertion loss. With reference to the schematic in Figure 17, the BPFs have been installed inside the P-band filter selector block, in the place of the "all band channels". The choice of the filter was not only influenced by the technical specification but also by the overall dimensions, due to the lack of available space inside the receiver block. Figure 19shows the picture of the BPFs mounted on the filter selector block. This filter allows a first discrimination of the frequencies of interest, reducing the bandwidth of the P-band receiver (305-410 MHz) and partially mitigating the RFI problem. It is worth mentioning that an IF Distributor, which was not present during the 2014 measurement campaign, has been added downstream to the optical link (compare Figure 11 and Figure 18). It allows the distribution of the RF signal coming from the antenna to the different back-ends installed inside the shielded room. This system is composed by an amplification stage and a set of passive splitters that separate the signal into three channels, one for each back-end. The overall gain of this section is of about 20 dB.

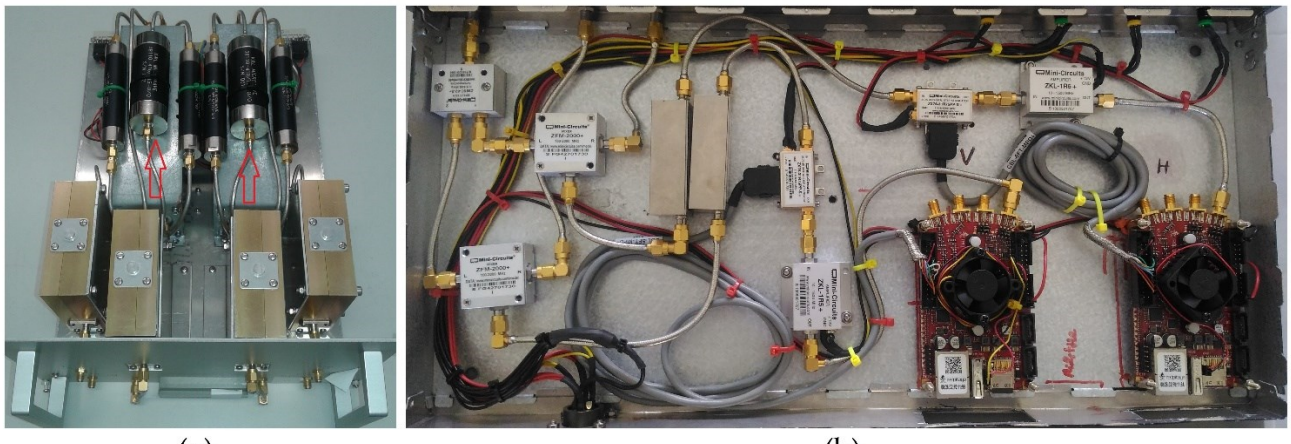

(a) (b)

Figure 19 - Photo of the 16 MHz bandwidth BPFs at 410 MHz (indicated by red arrows) mounted inside the filter selector block (a); Photo of the realized down-conversion block connected to the Red Pitaya board (b).

2.3.2 Down-conversion System

A down-conversion block was necessary to match the operating bandwidth of the dedicated back-end (0-50 MHz), based on the Red Pitaya board, which will be described in Section 2.3.3. Hence, for each path inside the channel, the RF signal in input at this block is down-converted to an Intermediate Frequency (IF) of 30 MHz and later filtered with a second BPF, model 3LB30-30/T5-O/O from K&L, centered at 30 MHz with 5 MHz bandwidth and 0.9 dB of insertion loss. The Local Oscillator (LO) frequency has been set to 380 MHz, depending on the frequency of the input signal, with a power of 13 dBm [22]. It is worth mentioning that the level of LO power in input at the mixer has to be 10 dBm, thus we doubled the level to be equally shared between the two channels. The frequency mixer is the ZFM-2000 model, from Mini-Circuits, working in the bandwidth 100-2000 MHz, with an isolation between the L-R and L-I ports of about 52 dB and 35 dB, respectively. Since the echoes traveling back from the debris could be very weak, a further amplification stage has been placed before the back-end section. The amplifier is the ZKL-1R5 model, from Mini-Circuits, working in the bandwidth 10-1500 MHz with about 40 dB gain at 30 MHz, a noise figure of 3 dB and an output power of about 17 dBm at 1-dB compression point [22].

It should be noted that the transmitter and the receiver of the BIRALET system are very close (20.86 km distance), therefore, the signal of the carrier is clearly visible during the acquisition by the SRT (see Section 2.4).

Due to the high transmitted power, this could be a critical downside, because it may “blind” the receiver system and bring to the saturation of the receiving chain. Unfortunately, the power level of the carrier at the SRT is not predictable, since it is influenced by several factors, such as the pointing direction of both the transmitter and the receiver antennas (the direct link is due to the side-lobes), the reflections from the ground, and the multiple reflections from hills, mountains, buildings, and so on. Thereby, a pre-detection measurement is required whilst the transmitter is switched on, just before the debris observation, in order to assess the true carrier power level. Though in our case the power level of the carrier is usually higher than the level of the echoes received by the debris, under particular conditions, due to the reasons listed above, it could be even possible that the echo of the debris is higher than the carrier. As a consequence, in order to avoid the saturation of the receiving chain, a digital step attenuator has been placed upstream of the amplifier, and suitably set based on the maximum expected received power. The attenuator is the ZX76-31R75PP-S model, purchased from Mini-Circuits, characterized by a resolution of 0.25 dB, a maximum attenuation of 31.75 dB and controlled by a 7-bit parallel interface with a single positive supply voltage. The control of the step attenuator is undertaken by the Red Pitaya, by means of the digital I/O pins available on the board, with a logic tension of 3.3 V. All the components described above are linked via SMA connectors. As there was the necessity to feed the Red Pitaya, the amplifier (both working with 5 V) and the step attenuator (12 V), at the same time, for both channels, a simple rack for supply management has been designed and realized. Inside the supply rack, two commercial switching transformers from Traco Power, again one for each channel, provide the 5 V and 12 V feeding. For each tension provided by the transformers, a fuse has been used. Every fuse has a protection stage against possible short-circuit of the fed elements. Figure 9b shows the realized down-conversion block, connected to the Red Pitaya board [22].

2.3.3 Dedicated Back-end

Once the signals are properly conditioned (filtered and adapted in terms of power level), they are ready to be processed by the Red Pitaya. The Red Pitaya is a System-on-a-Chip (SOC) board characterized by a dual-core ARM9 processor, working at 800 MHz, a FPGA with 28000 logic cells, 512 MB of DDR3 RAM system

memory, 2 RF inputs and 2 RF outputs, an overall 3dB-bandwidth of 50 MHz, a sample rate of 125 MSample/s and 14 bit of ADC resolution [22]. Hence, the two single polarization 5 MHz-wide signals centered at 30 MHz are converted into digital format at the sampling frequency corresponding to an instantaneous bandwidth of 65 MHz, in accordance with the Nyquist's theorem. At this stage, the general-purpose nature of the board allows any type of digital signal processing upon these signals. Initially, each Red Pitaya board was able to provide the digital data in a "raw" format, via the 1 Gbit/s link that the board is equipped with; in this case, the board would only operate as a digitizer and packetizer. However, because of the BPF at 30 MHz placed before the board, this unnecessary oversampling would be a useless waste of resource. In order to avoid the latter, a digital down-conversion (DDC) has been performed. The DDC converts a real, time domain signal into a complex one, centered in baseband. The process of frequency conversion is achieved by mixing the input signal with a digital tone (i.e. a sinusoid) at the center of the bandwidth of interest, 30 MHz in our case. This creates two copies of the signal, one centered near zero, and one centered at twice the tone frequency. This is possible using a second sinusoid, out of phase by 90 degrees. A direct digital synthesizer (DDS) generates the sinusoids internally. Once the base-band complex data, a low-pass filtering is necessary to remove unwanted spectral information and to avoid aliasing phenomena [22].

Since a considerable decimation is needed, we used the well-known CIC-FIR chain. The Cascade Integrator Comb (CIC) filter (also known as the Hogenauer filter) has proven to be an effective element in high-decimation systems, however CIC filters present an unsatisfactory frequency response, thus a Finite Impulse Response (FIR) filter is used in cascade so as to compensate for the CIC response and, as a consequence, to improve the overall filter response. Figure 20 shows a block diagram of the digital processing chain. The described procedure creates a base-band complex signal that can be stored and subsequently divided in several sub-bands by means of a Fast Fourier Transform (FFT). The FFT engine could be implemented in the FPGA as well, however the number of spectral points would be limited by the available memory on the FPGA, thus the engine has been implemented in the CPU/GPU boards [20].

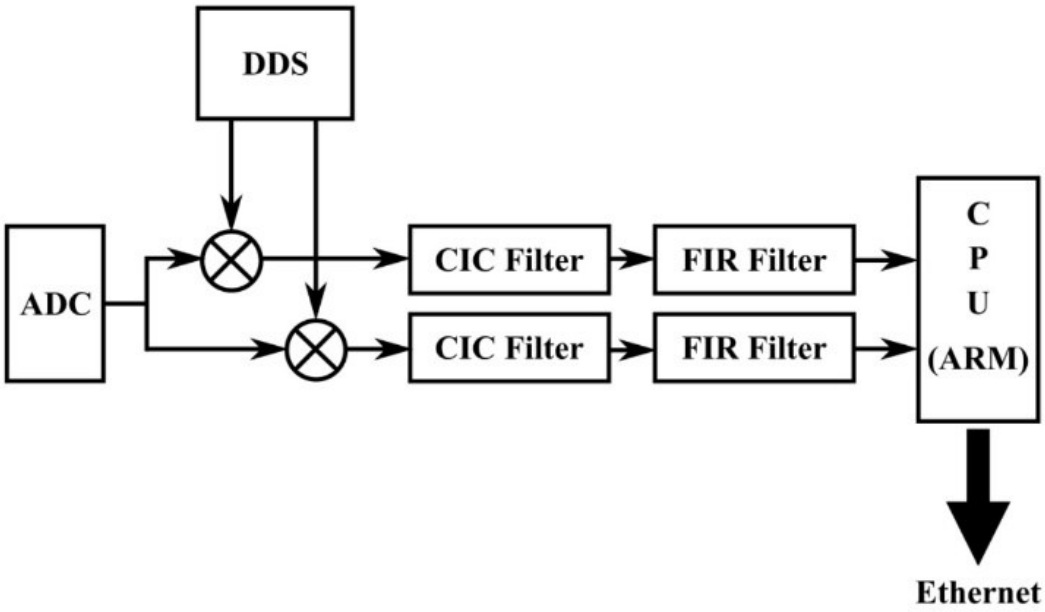

Figure 20 - Block diagram of the digital signal processing chain.

2.3.4 Characterization of the Receiving Chain

A complete characterization of the receiving chain has been performed in the Microwave Laboratory of the Cagliari Astronomical Observatory (INAF-OAC). The instrumentation employed for the characterization includes: two signal generators, model SMC100A from Rohde & Schwarz, a spectrum analyzer, model FSV from Rohde & Schwarz, and a Vector Network Analyzer (VNA), model ZVA67 from Rohde & Schwarz [22].

The first section to be characterized has been the P-band receiver block, with the latest addition of the two BPFs at 410 MHz with 16 MHz bandwidth (Figure 19a). For this measurement, the CFE of the P-band receiver has been bypassed, injecting a signal directly in the warm section (i.e. Linear to Circular Polarizer), and testing the whole block using the VNA. The response of the receiver block, in terms of scattering parameters, is reported in Figure 21.

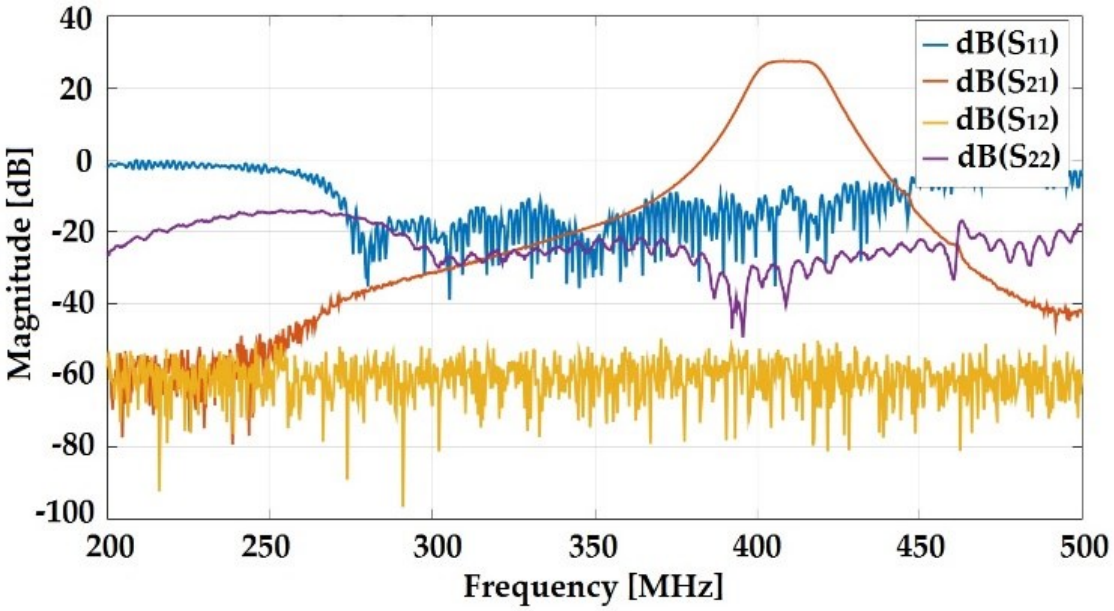

Figure 21 - Response of the vertical polarization channel of the P-band receiver, filtered with the BPF at 410 MHz.

For the sake of simplicity, we have reported only the response of the first channel, entrusted to carry the vertical polarization component of the signal. From the S21 curve, it is possible to appreciate the contribution of the BPF at 410 MHz that confines the signal in the 3-dB bandwidth 400.4-419.6 MHz. The S21 curve shows a maximum gain of about 27 dB, which matches, apart from some losses imputable to the coaxial cables used during the measurement, with the overall gain of the warm section of the P-band receiver (Figure 17).

The down-conversion block has been characterized taking into account the overall conversion gain, the compression point, and the evaluation of possible spurious frequencies of the whole block within the useful bandwidth. In the following, the LO power is set to 10 dBm and its frequency to 380 MHz, with the step attenuator set to 0 dB [22].

The conversion gain is a standard index of the performance of a heterodyne or super-heterodyne receiver system, determining the amount of IF power at the output of the block under test, given an input RF power level. In order to produce this result, a RF signal of -40 dBm, spanning from 407 to 413 MHz, has been injected in the block using a signal generator.

Then, a spectrum analyzer has been connected to the output of the amplifier of the acquisition chain, to detect the overall output signal. The conversion gain curve related to the down-conversion block is reported in Figure 22, showing a 3-dB bandwidth of about 5 MHz, between 27.5 and 32.5 MHz, with a maximum value of 33 dB. Such behavior was expected because of the BPFs centered at 30 MHz with 5 MHz bandwidth.

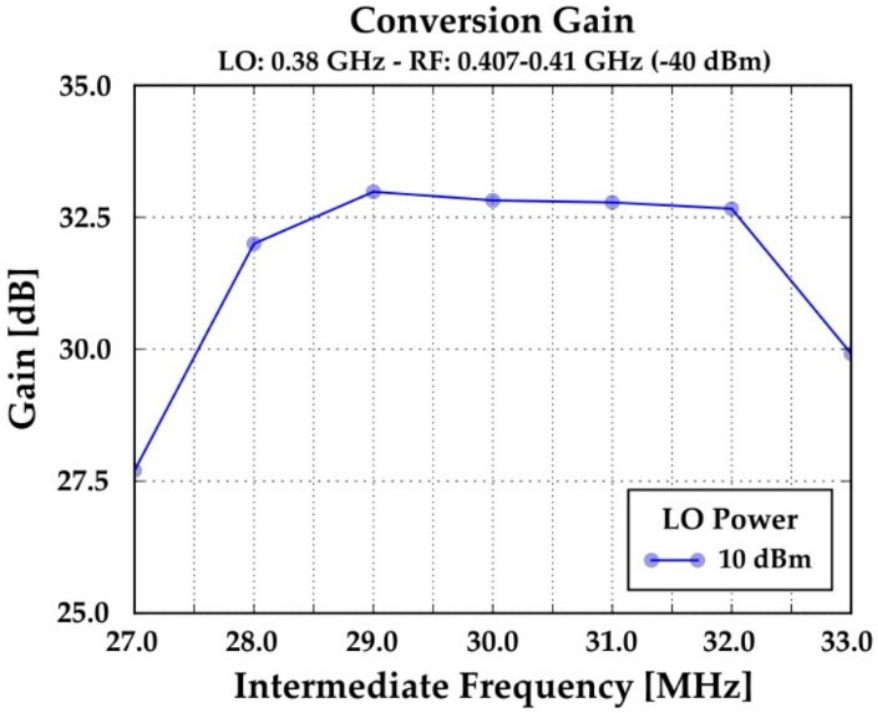

Figure 22 - Conversion Gain of the down-conversion block.

The evaluation of the compression point is useful to predict the level of signal that induces a non-linear response. This is due to the saturation of the amplifier that could produce signal distortion, and/or intermodulation products. In order to identify the compression point, a relatively low power signal has been injected at the input of the down-conversion block, and increased gradually, until the output signal starts to flatten. The 1-dB compression point at 410 MHz is reported in Figure 23, wherein RF input power has been varied from -40 dBm to -15 dBm with 1-dB steps. The dashed line represents the ideal output power and the slope of the curve represents the gain. The red line is the real output power of the block. It can be noticed that the 1-dB compression point, after which the down-conversion block enters in the compression region, is found for RF input signals greater than -21.2 dBm [22].

Finally, it should be noted that any possible contribution at the input of the block, including undesirable signals, could be potentially down-converted and fall into the bandwidth of the receiving chain due to the spurious frequencies of the LO. These frequencies can be evaluated using the following formula:

$$\omega_S = n \cdot \omega_{LO} - m \cdot \omega_{RF} \qquad (2.1)$$

where ω_{LO} is the LO frequency, ω_{RF} is the input RF frequency and $\{n, m\} \in \mathbb{Z},\ |n, m| \leq 5$. Higher values of the coefficients *n* and *m* give poor and, therefore, negligible contribution to the evaluation of the spurious frequencies. All the possible combinations of these values have been covered, giving no remarkable input in the IF bandwidth.

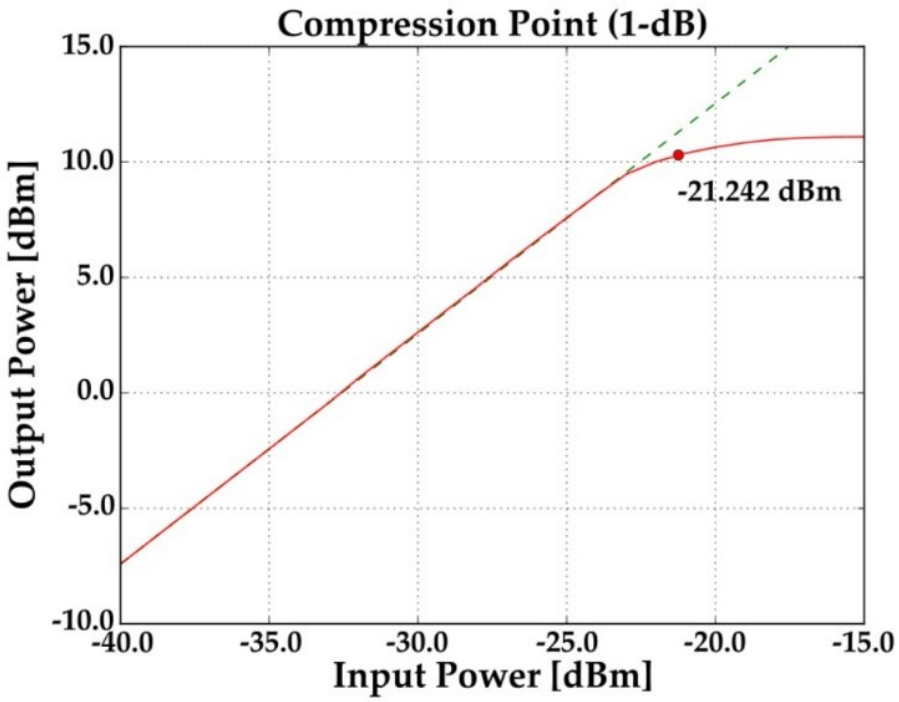

Figure 23 - 1-dB compression point at 410 MHz of the down-conversion block.

2.4 Space debris measurement campaigns

The typical scenario of observation with the BIRALET system is similar to operations for sky imaging with a single antenna as a receiver in a standard radio telescope. Imaging a large angular area of the sky with a single beam it requires to point that beam to a specific direction of the sky, then steering the antenna to different positions in order to cover the desired sky area. For each of the pointing, the antenna will be sensitive to signals from an angular area (FoV) depending on the HPBW, approximately equal to λ/D (with D is the telescope diameter). Different observing techniques are available to map a given area of the sky with a single-pixel feed (raster scan, on-the-flight mapping, etc.). If the beam shape is known, it is possible to mosaic over a given field with near-uniform sensitivity. This kind of pointing is the same used for space debris tracking observations with the BIRALET system. In fact, a generic known object can be tracked pointing the antenna beam in direction of the predicted object orbit. Moreover, this observation mode, based on various pointing for one sky map, could be used for tracking of unknown objects considering the covariance matrix associated to the object state. In other words, it is possible to track the object with a set of telescope pointing around the space debris predicted orbit through the covariance matrix related to the object state. The covariance matrix with the object state, in particular for unknown object, should be defined in a first measurement campaign using data performed by a survey radar, such as the BIRALES system. In this way, it is possible to observe unknown space debris with a multi-static radar composed by the BIRALES for survey mode and the BIRALET for tracking mode.

2.4.1 The first assessment of the new space debris channel in the Tiangong-1 re-entry campaign

The system described in the previous sections has been tested, for the first time, during the re-entry of the Chinese space station Tiangong-1. The Chinese National Space Administration (CNSA) launched the space station in September 2011, from the Jiuquan space center. However, in March 2016, the CNSA lost contact with the Tiangong-1; thereby, the re-entry in the Earth's atmosphere was uncontrolled. The space station was orbiting at altitudes below 250 km; it was characterized by an overall mass of about 7500 kg and a RCS of about 20 m^2. Since the expected re-entry point was comprised between latitudes of -42°S and +42°N, involving also southern Italy, the BIRALET system was included among the sensors engaged for the observation campaign.

On March 29, 2018 (not long before the space station re-entered in the Pacific Ocean, at 00:16 UTC of April 2, 2018), the falling Tiangong-1, was expected to cross our area of visibility. In particular, the following observations have been scheduled based on our estimate: from 07:55:38 UTC and 07:56:17 UTC, and from 09:27:28 UTC and 09:28:07 UTC. These intervals will be denoted in the following as "first passage" and "second passage", respectively.

Before the measurement campaign, a preliminary study has been conducted to evaluate the received power and the Doppler shifts for the two planned passages. The power level has been estimated in two specific points of the receiving chain: before the down-conversion block and at the end of the chain (see Figure 18). The values have been obtained starting from the well-known radar equation (the parameter used for the power estimate are reported in Table II) and adding both the gain and the losses of the receiving chain at the point of evaluation.

At this stage, the estimate of the echo power level before the down-conversion block has been compared with the pre-detected power level of the carrier (as pointed out in section III.B). Then, the higher value among the latter, has been used to properly set the step attenuator in order to avoid a possible compression of the amplifier.

The estimated power levels, compared with the measured ones, for the two passages, are reported in Table III. It is apparent that, in the first passage, the attenuation is not necessary, since neither the carrier nor the echo power are above the compression point, whereas for the second passage, the carrier is largely beyond it, and, therefore, the attenuation has been set to 20 dBm.

The Doppler shifts have been evaluated using the following formula:

$$\Delta f = \lambda^{-1}(\boldsymbol{v} \cdot \hat{\rho}_{TX} + \boldsymbol{v} \cdot \hat{\rho}_{RX}) \qquad (2.2)$$

wherein λ is the wavelength at the operating frequency, $\boldsymbol{v}$ is the object velocity vector, $\hat{\rho}_{TX}$ and $\hat{\rho}_{RX}$ are the versors of the conjunction vectors between transmitter and target and receiver and target, respectively, with reference to Figure 24. Using (2), the results are $\Delta f = -7.75\ kHz$ for the first passage and $\Delta f = 12.88\ kHz$ for the second passage.

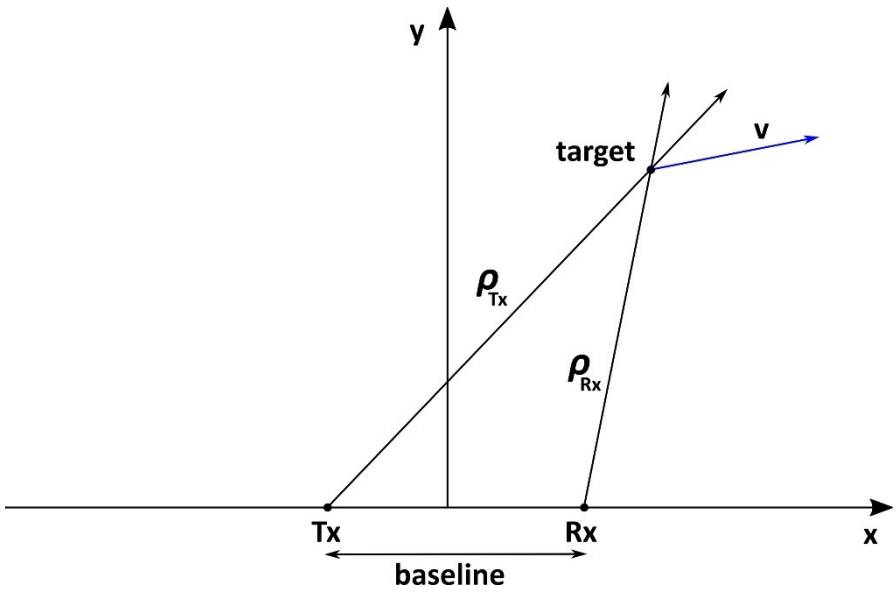

Figure 24 - Schematic of the bi-static Doppler geometry.

Table 4 - Parameters Used for the Estimation of the Received Power

Parameter	**1st Pass (07:56:03)**	**2nd Pass (09:27:48)**
Frequency	410.085 MHz	410.085 MHz
Tx Gain	27.3 dBi	27.3 dBi
Rx Gain	46.6 dBi	46.6 dBi
RCS	20.8 m^2	20.8 m^2
Tx Range	444 km	427 km
Rx Range	290 km	300 km

Table 5 - Estimated and measured power.

	CARRIER POWER (PRE-DETECTION/ INPUT OF THE DOWN-CONVERSION BLOCK)	**ECHO POWER (ESTIMATED/ INPUT OF THE DOWN-CONVERSION BLOCK)**	**TOTAL ECHO POWER**
ESTIMATED 1ST PASSAGE	NA	-28.85 dBm	3.65 dBm
MEASURED 1ST PASSAGE	-29.1 dBm	NA	3.30 dBm
ESTIMATED 2ST PASSAGE	NA	-22.85 dBm	-10.25 dBm
MEASURED 2ST PASSAGE	-7.24 dBm	NA	-9.51 dBm

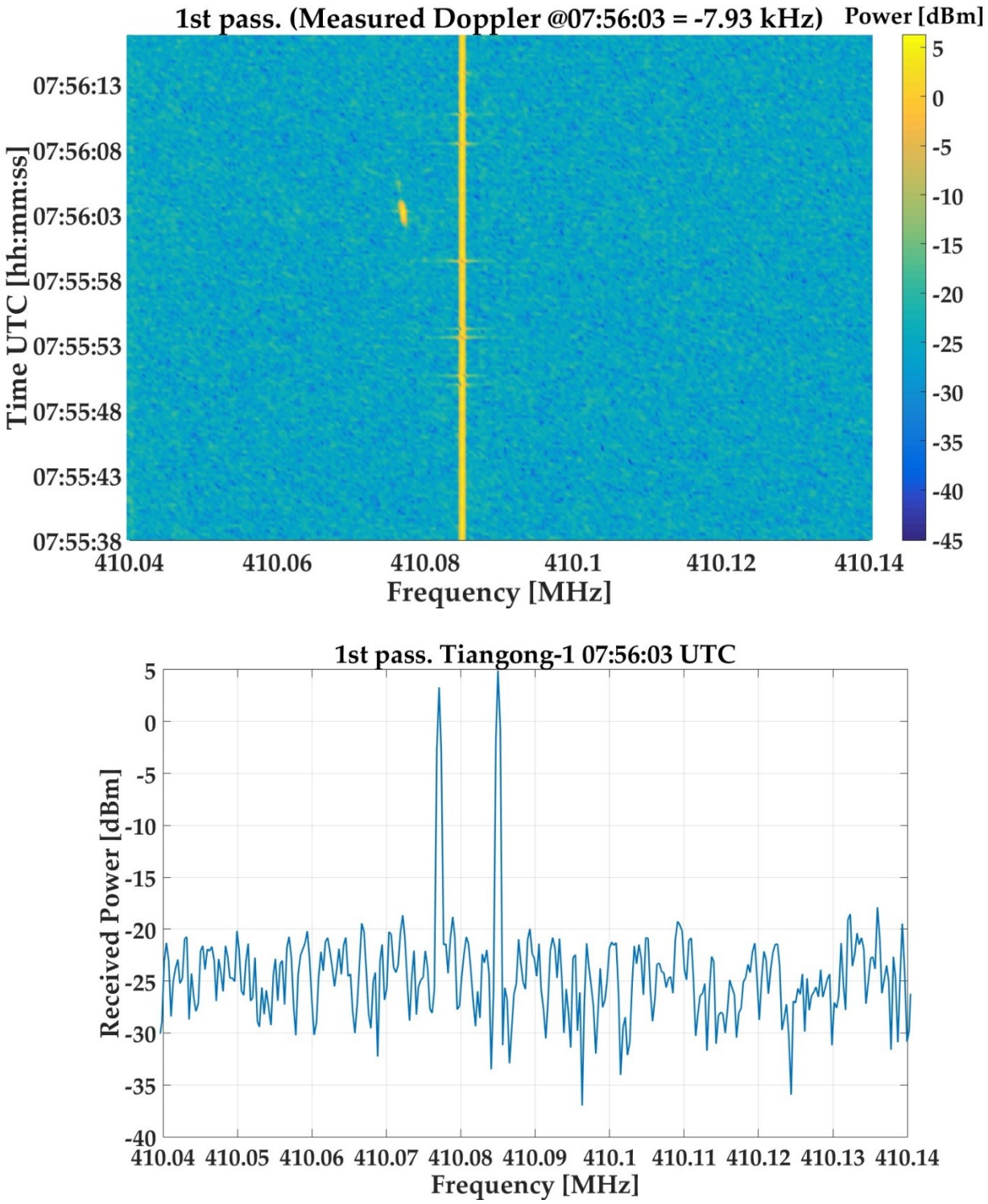

Figure 25 - Spectrogram of the first passage of the Tiangong-1 and data acquisition at 07:56:03 UTC.

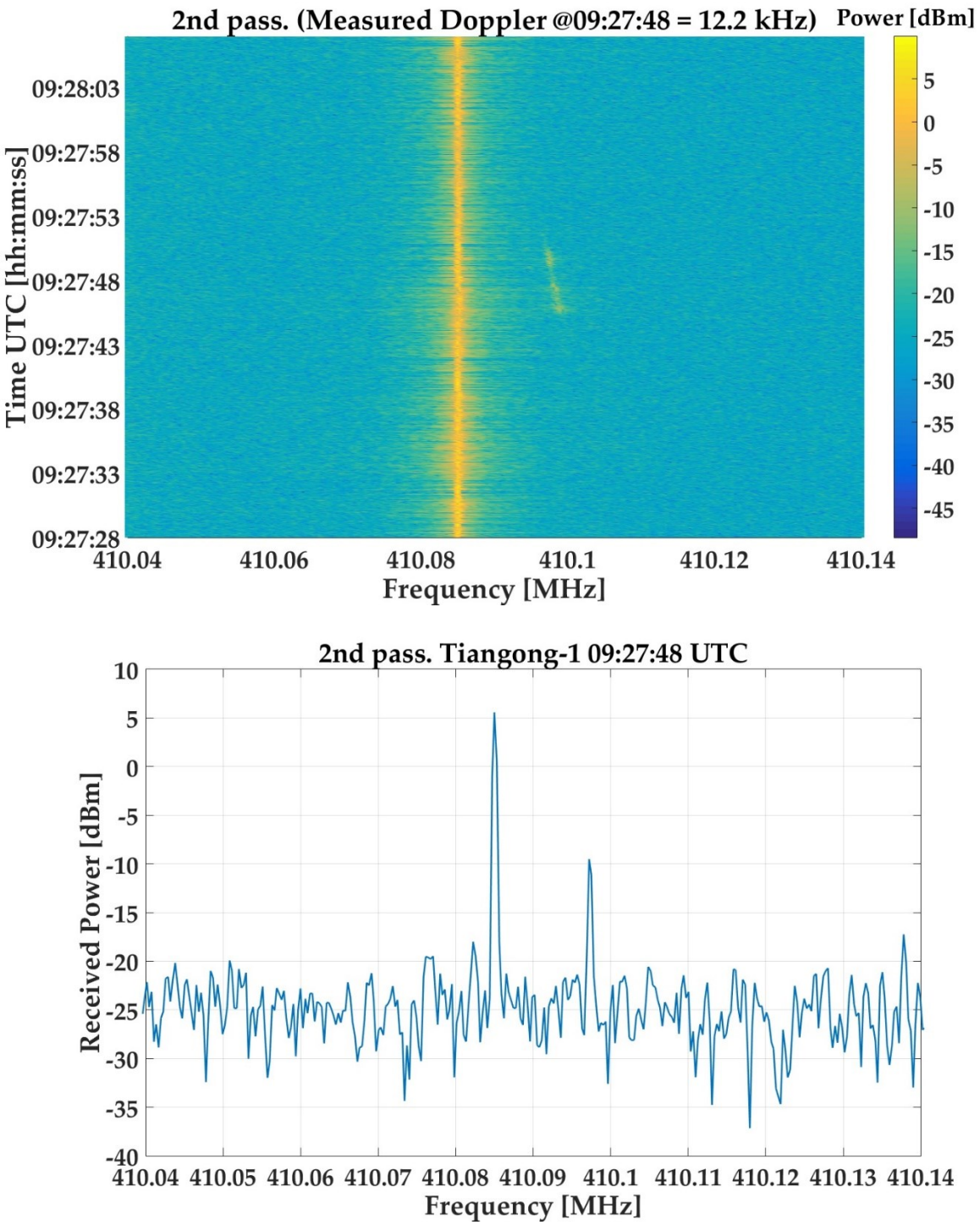

Figure 26 - Spectrogram of the second passage of the Tiangong-1 and data acquisition at 09:27:48 UTC.

The spectrograms, along the observation window, and the data acquisition at the center of the visibility interval, for these two passages are shown in Figure 25 and Figure 26, respectively. In these images, it is possible to recognize the swipe of the Tiangong-1 as it approaches the BIRALET system (first passage in Figure 25) and as it moves away from it (second passage in Figure 26). The carrier of the TRF transmitter is also clearly visible due to the proximity of the transmitter with the SRT. The measured Doppler shifts are in good agreement with predicted values (-7.75 kHz estimated vs -7.93 kHz measured for the first passage, 12.88 kHz estimated vs 12.2 kHz measured for the second passage).

Finally, a map of the captured spots of the two passages is shown in Figure 27: it has been obtained merging the data extracted from our tracking algorithm, useful to retrieve the position of the debris, with the satellite map of central Europe from Google Maps.

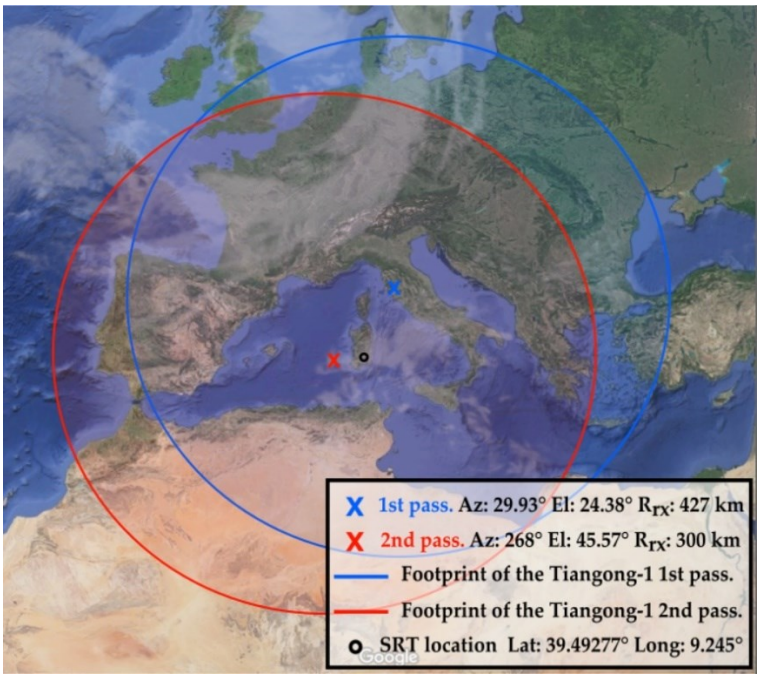

Figure 27 - Azimuthal equidistant map of the two passages of the Tiangong-1, with the relative footprint. For each passage, the pointing coordinates (azimuth and elevation) and the range from the SRT are shown.

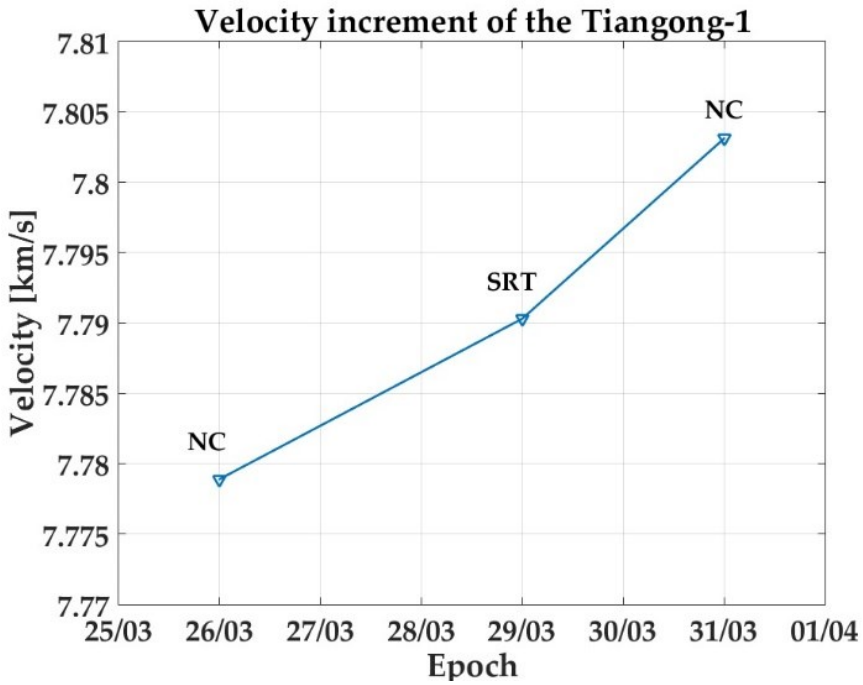

Figure 28 - Velocity increment of the Tiangong-1 based on the data of March 26 (Northern Cross), 29 (SRT) and 31 (Northern Cross) 2018.

The Doppler data derived from the SRT measurements have been used along with those of different sensors involved in the Tiangong-1 monitoring program, in particular with the Northern Cross Radio Telescope [17]. Figure 18 shows how the joint measurements of the SRT and the Northern Cross allowed the estimation of the acceleration of the Chinese space station. It can be noticed the gradual increment in the velocity of the object, which corresponds to a consistent lowering in its orbit, i.e. the altitude from the Earth's surface. The Doppler data from the Northern Cross are related to March 26 and 31, 2018.

2.4.2 Resident space objects measurement campaigns

Between December 13th, 2018 and October 8nd, 2019, the BIRALET system has been able to observe a total of 33 objects. All the observations have been made in beam-park mode, waiting for the objects to cross the Field Of View (FOV) of the antenna.

The list of the scheduled passages for the debris, complete with the pointing coordinates, RCS, slant range (SR) and detection time for each object, is reported in Table 6. Before the observations, a forecasting campaign has been made in order to obtain the azimuth and elevation pointing coordinates and to predict the Doppler frequency. An algorithm based on the reading of the Two-Line Element set (TLEs - a coded ASCII text file containing the orbital information of the debris and made available by the US Joint Space Operations Center) provides these pieces of information. These operations are described in detail in the next Chapter 3. The predicted and the measured Doppler shift for each object in the list is reported in Table 7.

Table 6 - Scheduled passages of the debris.

NORAD ID OBJECT	AZIMUTH [DEG]	ELEVATION [DEG]	RCS [M^2]	SR [KM]	DATE [MM/DD/YYYY]	TIME OF DETECTION [UTC]
6350	16.437	32.751	1.73	1694.078	12/13/2018	13:28:25
1328	79.358	75.448	2.16	1901.43	12/13/2018	13:48:19
26222	43.996	65.927	4.99	1571.70	12/13/2018	14:30:57
25482	33.651	62.505	1.06	1732.62	12/13/2018	15:00:36
30774	18.163	32.133	3.64	1526.68	12/13/2018	15:57:26
4256	87.967	75.484	0.51	1883.31	03/19/2019	14:36:20
39194	45.917	56.256	7.77	1068.92	03/22/2019	15:45:54
12150	49.961	72.920	5.07	2077.30	03/22/2019	16:07:03
28931	40.097	63.139	13.4	1540.01	03/22/2019	16:28:14
11166	126.647	70.556	6.05	1808.33	03/22/2019	16:53:39
7337	204.068	69.955	2.98	1952.61	09/06/2019	13:25:49
7646	311.755	50.602	0.17	2447.17	09/06/2019	14:38:30
36508	340.408	55.379	2.95	1700.43	09/06/2019	15:10:44
1328	94.379	66.816	2.16	2090.32	09/06/2019	15:43:55

39452	42.087	51.607	2.34	1080.77	09/06/2019	15:57:17
1328	118.746	72.537	2.16	1929.63	09/16/2019	12:08:18
42969	36.109	72.375	unknown	1727.42	09/16/2019	12:16:11
27944	60.085	53.297	0.13	1646.96	09/16/2019	13:31:07
1328	68.865	53.699	2.16	2220.55	09/16/2019	14:02:58
22824	99.517	53.116	0.16	1953.58	09/16/2019	14:45:45
36508	263.826	46.492	2.95	1918.60	09/16/2019	14:59:43
39453	321.540	48.670	2.41	1136.08	09/16/2019	15:29:59
15494	193.782	68.242	7.12	1071.12	10/08/2019	07:02:44
26102	22.286	60.228	3.35	917.86	10/08/2019	07:28:36
36119	58.139	63.318	2.18	1057.37	10/08/2019	07:34:44
3047	180.116	65.685	2.96	1557.96	10/08/2019	07:57:54
43243	182.686	79.956	unknown	586.60	10/08/2019	08:34:46
8458	253.576	71.252	2.02	1650.39	10/08/2019	08:48:32
40961	328.387	39.208	2.32	1955.37	10/08/2019	10:21:38
7363	18.799	67.056	4.76	1908.75	10/08/2019	11:36:22
33492	27.231	61.772	4.8	1500.13	10/08/2019	12:44:46
15595	44.335	63.236	9.3	1694.26	10/08/2019	14:10:37
25105	318.231	51.425	4.14	1876.84	10/08/2019	14:42:20

Table 7 - Estimated and measured Doppler shift of the debris.

NORAD ID OBJECT	SNR [DB]	ESTIMATED DOPPLER [KHZ]	MEASURED DOPPLER [KHZ]
6350	20.3	2.660	2.070
1328	22.9	-4.036	-3.300
26222	32.2	-3.635	-3.486
25482	7.5	-6.313	-6.480
30774	29.5	-1.590	-2.110
4256	24.6	-1.699	-1.650
39194	12	4.222	4.440
12150	20	-1.182	-0.872
28931	34	-5.854	-4.660
11166	17.5	-5.015	-4.280
7337	18.5	4.872	4.900
7646	25.3	4.641	5.360
36508	31.3	9.215	9.600
1328	10.7	-6.246	-6.380
39452	16.4	-8.657	-8.820
1328	25.7	-3.086	-3.120
42969	34.8	-3.290	-3.260

27944	14.3	7.121	6.880
1328	16.4	-9.319	-9.416
22824	16.7	5.254	5.540
36508	22.4	-3.731	-3.260
39453	20.8	-9427	-9.750
15494	31.1	7.279	7.260
26102	17.1	-7.962	-7.440
36119	23.5	5.778	5.620
3047	20.2	-7.192	-7.280
43243	16.5	-4.042	-4.240
8458	32.0	3.543	3.400
40961	18.1	9.587	9.922
7363	19.5	-6.636	-6.660
33492	19.9	8.486	8.160
15595	16.2	7.799	7.420
25105	21.7	-7.693	-8.040

For clarity, the spectrogram of the entire observation window for the objects with NORAD ID 4256, as well as the passage inside the beam of the SRT for each debris in the list, are shown in Figure 29. As it can be seen from the analysis of the results in Table 7, every debris in the list has been correctly detected. Due to the relative close proximity of the transmitter with the SRT, the radio telescope has been able to receive the carrier frequency (410.085 MHz), which is clearly visible in the images. Additionally, in the spectrogram (Figure 29), it is recognizable the frequency swipe of the debris echo, due to its high velocity, as it moves toward the receiver position (when the echo is located to the left of the carrier, which implies a negative Doppler shift) or as it moves away from it (when the echo is located to the right of the carrier, which implies a positive Doppler shift). The passage inside the beam of the SRT is a representation of the portion of the beam's footprint covered by each debris during its passage. This particular subject is a case in study that might be worth to be further investigate. At this stage, we may assume that the diameter of this footprint is ideally equal to the width of the HPBW (0.8 degrees). As it can be seen from the figures, the distance travelled inside the SRT beam, for every debris listed, is smaller than this value. The degrees travelled for each debris are evaluated taking into account the transit time and the angular velocity (which has been calculated from the Doppler frequency and reported in Table 7). The likely implication is that the debris does not pass through the beam's center, but instead in a peripheral area. This drawback is easily explainable with a very small inaccuracy in the pointing coordinates.

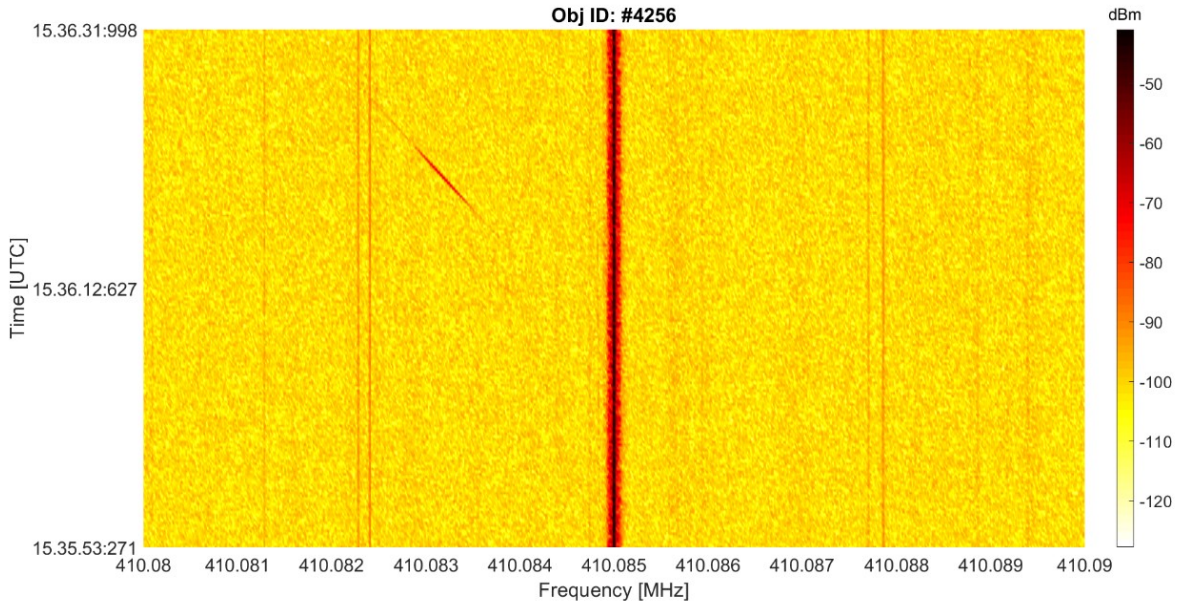

(a)

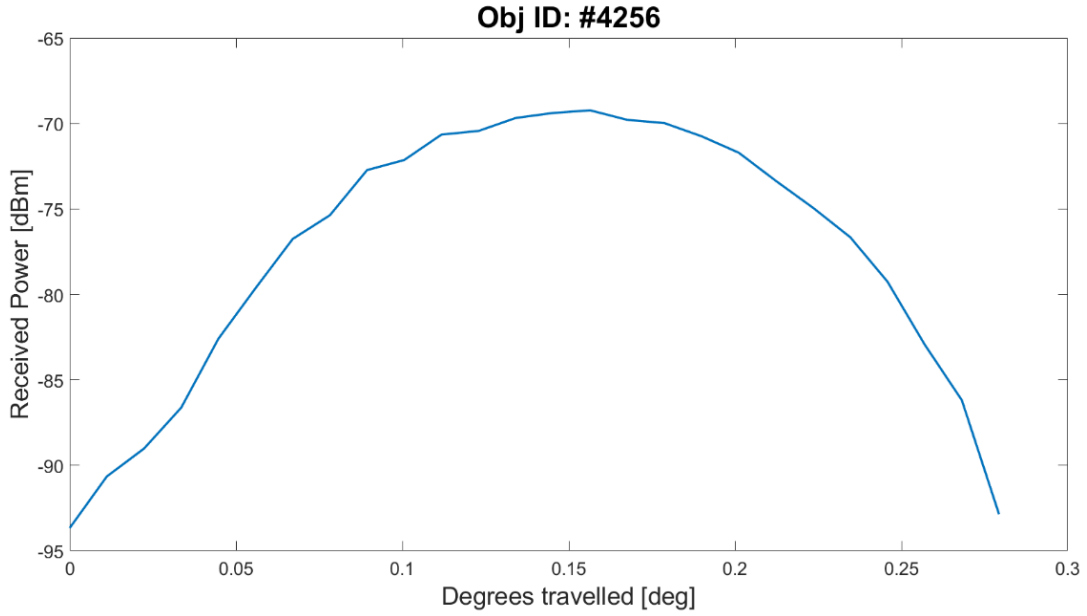

(b)

Figure 29 - Debris 4256: (a) spectrogram; (b) passage inside the beam of the SRT.

A remarkable result obtained in these measurement campaigns, is that the RFI along the observation bandwidth is heavily reduced with respect to the previous debris observation campaign [19].

To further emphasize the absence of in-band RFI of the new measurements, in Figure 30, the results of an RFI measurement campaign for the P-band receiver of the SRT are presented. The measurements date back to June 2013, 10 months before the first space debris test of April 2014, and they have been acquired in three different locations around the radio telescope facility, accordingly to the map shown in Figure 31, using a mobile station equipped with a spectrum analyzer [13]. From Figure 30, it is clear that the P-band of the SRT is plagued by many RFI, partly self-generated and partly due to external sources. With self-generated, we

refer to interferences due to micro-electrical discharges of the power lines near the SRT and to the instrumentation located in the area of the radio telescope. The main contributions to the latter are:

- SRT electrical box (350 MHz);
- Control board of the P-band receiver (around 410 MHz);

The external signals, instead, are imputable to:

- VOIP services (318-321 MHz);
- AM services (327-332 MHz);
- Terrestrial Trunked Radio (TETRA) in use by the Italian Ministry of Defense (385-395 MHz);
- Radio TV link signal (400 MHz);
- Weather balloon (406.8 MHz - variable).

It is worth noting that most of these interferences do not change in frequency and so are easily recognizable.

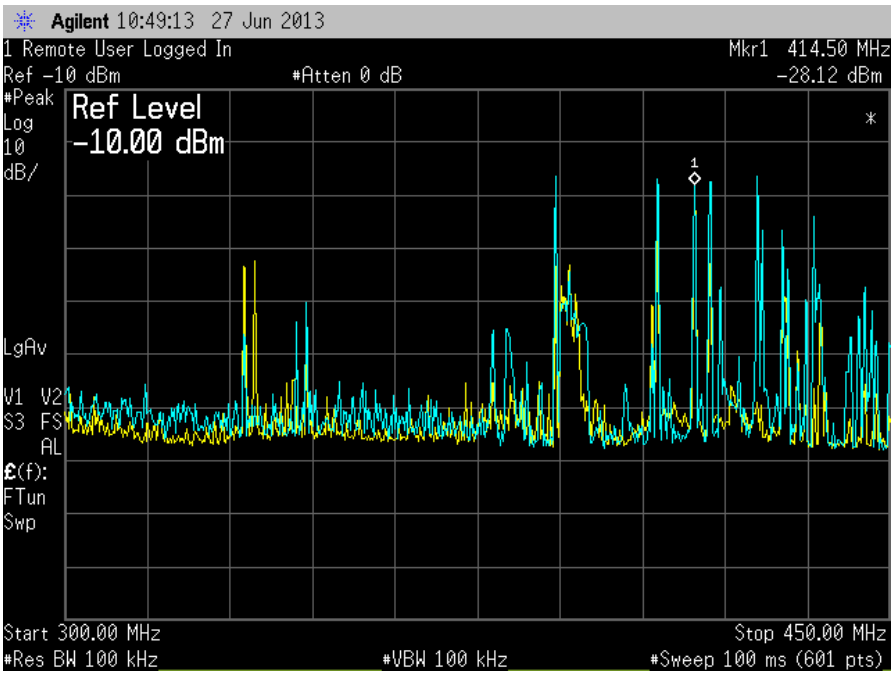

(a)

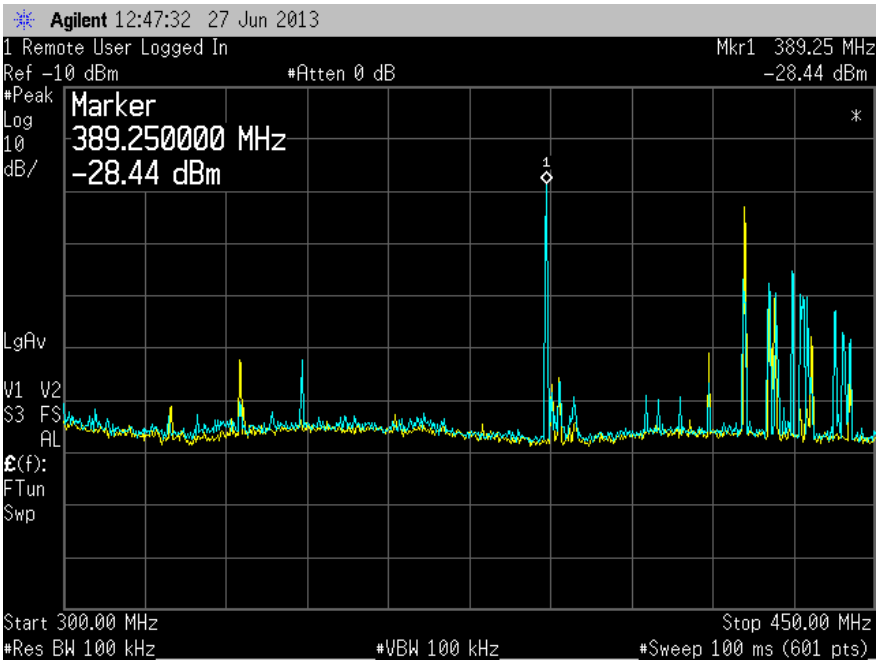

(b)

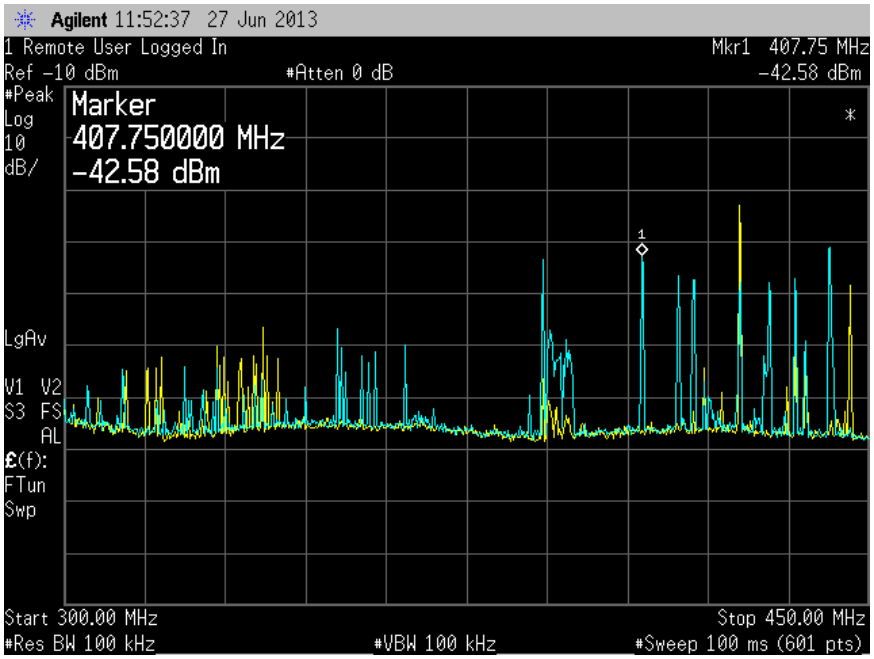

(c)

Figure 30 - RFI measurement campaign for the P-band of the SRT during June 2013: (a) RFI acquired in point X (see Figure 31); (b) RFI acquired in point Y; (c) RFI acquired in point Z.

Both types of interferences had to be filtered in order to make the space debris channel suitable for the observations. The presence of RFI is undeniable in the results presented in [19], but being the latter the first test on the capabilities of the SRT as a receiver for space debris monitoring, the authors focused on the reception of the object echo rather than on the presence of in-band interferences. With the following measurements and the consequent change of priority, the main goal was to make the SRT not only employable but also performing. Such an achievement is confirmed by the presented results. Most of the RFI have been suppressed thanks to the 5 MHz BPF of the down-conversion block (see Figure 18). However, the

resulting operating bandwidth 407.5-412.5 MHz was still vulnerable to the interferences. Thus, a device that was able to remove the interferences preserving the useful signals was needed. These features can be found in an adaptive filter, such as a Finite Impulse Response (FIR) filter [23]. The idea behind this procedure is to obtain a mask representing the in-band RFI that can be subtracted to the acquired signal in order to receive only the carrier and the debris echo [23]. While this operation requires a very powerful (and expensive) FPGA board to work over wide frequency range, to handle the IF 5-MHz bandwidth of the new channel, the Red Pitaya was sufficient. As shown in [23], the acquisition of the RFI mask requires a reference antenna. However, in our case, since the new channel is doubled (see Figure 18), one for each linear polarization, the RFI mask has been acquired by the second chain when the carrier transmission was off. In this case, the a priori knowledge of the exact frequency of the interferences allowed for a simpler implementation of the RFI suppression that otherwise would have required a recursive algorithm. Furthermore, the implementation of a FIR filter has been already done for the digital processing chain of the Red Pitaya board, as shown in [22] (see Figure 18). One of the advantages of using a digital filter implemented in the Red Pitaya is that the RFI "subtraction" can be performed in post-processing.

Figure 31 - Map of the locations of the P-band RFI measurements performed on June 2013.

3. Orbit determination using the P-band BIRALET system

The data obtained from the measurement campaigns are used in input at orbit determination algorithms. For the resident space objects orbit determination problem, the minimal set of parameters will be the position and velocity vectors at some given epoch. This minimal set could be expanded to include dynamic and measurement model parameters, which may be needed to improve the prediction accuracy. The general orbit determination problem can then be posed as follows. If at some initial time, the state of a vehicle following a ballistic trajectory is given and if the differential equations that govern the motion of the vehicle are known, then the equations of motion can be integrated to determine the state of the vehicle at any time. However, during an actual flight, the initial state is never known exactly. Moreover, certain physical constants as well as the mathematical specification of the forces required to define the differential equations of motion are known only approximately. Such errors will cause the actual motion to deviate from the predicted motion. Consequently, in order to determine the position of the spacecraft at some time t > t0, it must be tracked or observed from tracking stations whose positions are known precisely. With the observations of the spacecraft motion, a better estimate of the trajectory can be determined. The term “better estimate” is used since the observations will be subject to both random and systematic errors and, consequently, the estimate of the trajectory will not be exact. The observational data will usually consist of such measurements as range, range-rate, azimuth, elevation, or other observable quantities. That is, the state variables (position, velocity, unknown model parameters, etc.) will not be observed, but rather the observable will usually be some nonlinear function of the state variables. When an estimate of the trajectory has been made, the subsequent motion and values for the observations can be predicted. In the orbit determination procedure, the process of predicting the state of a vehicle is referred to as “generating an ephemeris.” An ephemeris for a space object is a table of its position and velocity components as a function of time. The predicted values will differ from the true values because of inaccuracies in the estimated state vector (i.e., position and velocity vector) caused by errors in the orbit determination process, such as approximations involved in the method of orbit improvement and in the mathematical model, errors in the observations, errors in the computational procedure used in the solution process. Consequently, the process of observation and estimation must be repeated continually as the vehicle’s motion evolves. Furthermore, the orbit determination procedure may be used to obtain better estimates of the location of tracking stations, adjust the station clocks, calibrate radar biases, obtain a better estimate of geophysical constants, and so on. In fact, any observable quantity directly affecting either the motion of the vehicle or the observation-state relationship can be determined by appropriately using the observational data.

This section illustrates the results of numerical simulations performed to assess the performance of BIRALET in terms of both observation capabilities and orbit determination accuracy during follow-up observations. The analyses will be limited to the case of catalogued objects, i.e. objects for which a preliminary knowledge of the state and objects parameters is available. Details are provided in the following paragraphs.

3.1 Observation Capabilities

This section investigates the observational capabilities of BIRALET sensor. The analysis is carried out considering the NORAD LEO population as target objects [24]. The population and related Two-Line Elements were retrieved from SPACE-TRACK website on July 25, 2019 and consist of 3015 objects. Of these objects, only those with known radar cross section (RCS) are considered, giving a total number of objects of 2301. A dedicated software for simulating the passages of the objects was developed. For each catalogued object, the software propagates its TLE by means of the SGP4 dynamical model and computes possible passages that

could be detected by BIRALET. A passage is considered detectable if the constraints on the RX and TX minimum elevation are satisfied, and the detected SNR is larger than an imposed threshold (typically 6 dB). For each detectable passage, the software provides a list of time epochs and required pointing directions, i.e. RX and TX azimuth and elevation, along with the measured SNR value and Doppler shift measurements. Only time epochs for which the SNR limit and the RX and TX rotational speeds constraints are satisfied are considered. For the considered simulations, the TLE propagated with the SGP4 dynamical model represents the real dynamics of the system. In order to model possible discrepancies between the real object dynamics and the available model, a uniform random error in the time variable is assumed, i.e., for each passage, a time shift δ is guessed by sampling from a uniform distribution $\Delta \sim \mathcal{U}(-0.2, 0.2)$s, and the RX and TX pointing direction are computed considering a time epoch.

$$t_{shift} = t_{real} + \delta \qquad (3.1)$$

where t_{real} represents the time epoch predicted by the TLE (the real world), whereas t_{shift} represents the time epoch used to compute the sensor pointing directions. This model essentially assumes that the error is mainly in the along-track direction, which is what typically happens when an estimate is propagated in time. The uncertainty interval for the time variable was selected according to data obtained from some observation campaigns performed with the sensor [24].

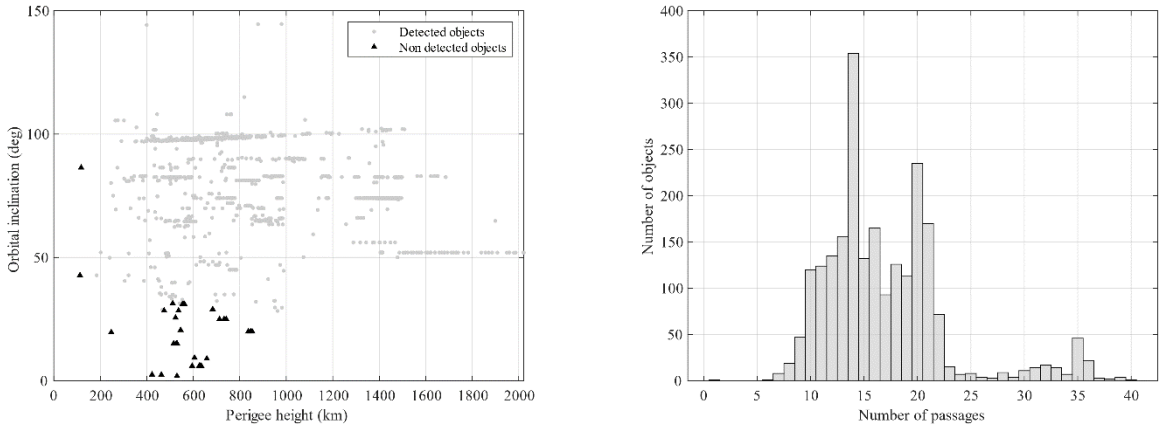

(**a**) (**b**)

Figure 32 - SRT observation capabilities: (a) orbital inclination as a function of the perigee height, (b) number of passages per object.

The analysis considers an observation window of one week, from July 26th, 2019, 00:00:00 UTC to August 2nd, 2019, 00:00:00 UTC [24]. Figure 32a shows the results of the simulation in terms of objects orbital inclination distribution as a function of the perigee height. Objects that are detected during the seven-days observation campaign are represented with grey dots, whereas non-detected objects are plotted with black triangles. Starting from a catalogue of 2301 objects, 2262 objects are detected at least once. That it, the sensor potentially covers more than 98% of the target population. As can be seen, the sensor cannot observe only objects with a low orbital inclination and perigee height. Figure 32b, instead, shows the distribution of the number of passages per object. The vast majority of the objects has a number of passages between 10 and 20. The results previously described represent the upper bound of the performance of BIRALET. The sensor, indeed, is assumed to be capable of observing multiple objects at the same time, and no time separation

between consecutive observations is imposed. These constraints are introduced when orbit determination is performed, as described in the following paragraphs.

3.2 Orbit Determination Refinement

The analysis presented in the previous section was focused on the observation capabilities of BIRALET. The goal of this second section is to assess the performance of the sensor while performing Orbit Determination (OD) refinement. Specifically, the accuracy of the state estimates at both the OD epoch and later epochs is investigated. Starting from the list of detectable passages, a reduced list of passages is obtained by sorting them in chronological order and imposing a minimum time distance between two consecutive passages of 20 minutes. The list is thus reduced to 355 passages [24]. For all the objects of the list, we assume that an estimate for their state vector (i.e. position and velocity) is available at time epoch t_0 (26 July 2019 00:00:00 UTC). This estimate, which may be obtained by other sensors capable of performing initial orbit determination (e.g. BIRALES radar sensor), can be modelled as a normal random variable (RV)

$$\widehat{\boldsymbol{X}}_{t_0}^{ECI} \sim \mathcal{N}(\widehat{\boldsymbol{\mu}}_{t_0}^{ECI}, \widehat{\boldsymbol{C}}_{t_0}^{ECI}) \tag{3.2}$$

where $\widehat{\boldsymbol{\mu}}_{t_0}^{ECI}$ is the mean value, whereas $\widehat{\boldsymbol{C}}_{t_0}^{ECI}$ is the associated covariance matrix. The superscript "ECI" indicates that the variable is expressed in the Earth Centered Inertial reference frame, whereas the subscript t_0 indicates the epoch the estimate refers to. The mean value of the estimate $\widehat{\boldsymbol{\mu}}_{t_0}^{ECI}$ is computed by propagating, for each object, its TLE to $t = t_0$, computing its state vector in ECI reference frame $\boldsymbol{x}_{t0}^{ECI}$, computing the rotation matrix $A^{ECI2RSW}$ from ECI to radial, along-track, cross track (RSW) reference frame [22], and perturbing the state vector with a random vector $\boldsymbol{\varepsilon}_{t_0}^{ECI}$

$$\widehat{\boldsymbol{\mu}}_{t_0}^{ECI} = \boldsymbol{x}_{t_0}^{ECI} + \boldsymbol{\varepsilon}_{t_0}^{ECI} \tag{3.3}$$

where

$$\boldsymbol{\varepsilon}_{t_0}^{ECI} = \begin{bmatrix} \boldsymbol{A}^{ECI2RSW^T} & 0 \\ 0 & \boldsymbol{A}^{ECI2RSW^T} \end{bmatrix} \begin{Bmatrix} \boldsymbol{\varepsilon}_{t_0,p}^{RSW} \\ \boldsymbol{\varepsilon}_{t_0,v}^{RSW} \end{Bmatrix} \tag{3.4}$$

and

$$\begin{aligned} \boldsymbol{\varepsilon}_{t_0,p}^{RSW} &= \begin{Bmatrix} \mathcal{U}(-00.1,0.01) \\ \mathcal{U}(-0.05,0.05) \\ \mathcal{U}(-0.01,0.01) \end{Bmatrix} \text{km} \\ \boldsymbol{\varepsilon}_{t_0,v}^{RSW} &= \begin{Bmatrix} \mathcal{U}(-0.5,0.5) \\ \mathcal{U}(-0.5,0.5) \\ \mathcal{U}(-0.5,0.5) \end{Bmatrix} \text{m/s} \end{aligned} \tag{3.5}$$

The variables $\boldsymbol{\varepsilon}_{t_0,p}^{RSW}$ and $\boldsymbol{\varepsilon}_{t_0,v}^{RSW}$ represent random errors in position and velocity expressed in the RSW reference frame. The covariance matrix is estimated by assuming reasonable values for the standard deviations in position (σ_p) and velocity (σ_v) in the RSW reference frame, building a diagonal covariance in RSW reference frame, and expressing this matrix in the ECI reference frame. If we indicate with $\widehat{\boldsymbol{C}}_{t_0}^{RSW}$ the covariance matrix expressed in the RSW reference frame, where

$$\widehat{\boldsymbol{C}}_{t_0}^{RSW} = \text{diag}\left(\left(\sigma_p^R\right)^2 \quad \left(\sigma_p^S\right)^2 \quad \left(\sigma_p^W\right)^2 \quad (\sigma_v^R)^2 \quad (\sigma_v^S)^2 \quad (\sigma_v^W)^2 \right) \tag{3.6}$$

and $\sigma_p^R = \sigma_p^W = 0.1$ km, $\sigma_p^S = 0.2$ km, $\sigma_v^R = \sigma_v^S = \sigma_v^W = 1$ m/, we can express the covariance matrix in the ECI reference frame as

$$\widehat{\boldsymbol{C}}_{t_0}^{ECI} = \boldsymbol{A}^{ECI2RSW^T}\, \widehat{\boldsymbol{C}}_{t_0}^{RSW} \boldsymbol{A}^{ECI2RSW} \tag{3.7}$$

The values used for the errors and the standard deviations are typical values that can be obtained with accurate initial orbit determination [4]. The described procedure is repeated for all the objects of the passage list, thus creating a database of state estimates at time epoch t_0.

The goal of the presented analysis is to understand how the initial database evolves in time assuming orbit refinement with BIRALET only. For all the objects of the selected passage list, the OD refinement consists of two phases: estimate propagation and estimate update. The estimate propagation phase consists in propagating the available state estimate of a given object to the epoch of its new passage

$$\overline{\boldsymbol{X}}_{t_{obs,1}^{new}} = \boldsymbol{g}\left(\widehat{\boldsymbol{X}}_{t^{old}}\right) \sim \mathcal{N}\left(\overline{\boldsymbol{\mu}}_{t_{obs,1}^{new}}, \overline{\boldsymbol{C}}_{t_{obs,1}^{new}}\right) \tag{3.8}$$

where $\boldsymbol{g}$ is the nonlinear function (i.e. the considered orbital dynamics) mapping the state estimate from the epoch t^{old} to the new observation epoch $t_{obs,1}^{new}$, $\widehat{\boldsymbol{X}}_{t^{old}}$ is the last available estimate at time epoch t^{old}, whereas $\overline{\boldsymbol{X}}_{t_{obs,1}^{new}}$ is the a priori estimate at the new observation epoch $t_{obs,1}^{new}$ (here assumed still a Gaussian RV). The estimate propagation is done by means of the unscented transform (UT). The UT is a method for calculating the statistics of a random variable that undergoes a nonlinear transformation. The basic idea of the UT is to convert the nonlinear transformation of the RV into a series of nonlinear transformation of selected realizations of the RV, called "sigma points", and then retrieve the mean and covariance of the transformed RV by performing a weighted sample mean and covariance of the transformed sigma points. Following the description given in [23], consider propagating the state estimate $\widehat{\boldsymbol{X}}_{t^{old}}$ through the nonlinear function $\boldsymbol{g}$ from t^{old} to $t_{obs,1}^{new}$, thus obtaining the estimate $\overline{\boldsymbol{X}}_{t_{obs,1}^{new}}$. The initial state estimate is assumed to be a normal random variable, so it can be described by a mean $\widehat{\boldsymbol{\mu}}_{t^{old}}$ and a covariance $\widehat{\boldsymbol{C}}_{t^{old}}$. In order to compute the statistics of $\overline{\boldsymbol{X}}_{t_{obs,1}^{new}}$, the UT starts by forming a matrix $\boldsymbol{\mathcal{X}}$ of $(2L+1)$ sigma vectors $\boldsymbol{\mathcal{X}}_{i,t^{old}}$ and the corresponding weights W_i, according to the following definitions

$$\boldsymbol{\mathcal{X}}_{0,t^{old}} = \widehat{\boldsymbol{\mu}}_{t^{old}} \tag{3.9}$$

$$\boldsymbol{\mathcal{X}}_{i,t^{old}} = \widehat{\boldsymbol{\mu}}_{t^{old}} + \left(\sqrt{(L+\lambda)\widehat{\boldsymbol{C}}_{t^{old}}}\right)_i \qquad i = 1, \dots, L \tag{3.10}$$

$$\boldsymbol{\mathcal{X}}_{i,t^{old}} = \widehat{\boldsymbol{\mu}}_{t^{old}} - \left(\sqrt{(L+\lambda)\widehat{\boldsymbol{C}}_{t^{old}}}\right)_{i-L} \qquad i = L+1, \dots, 2L \tag{3.11}$$

$$W_0^{(m)} = \lambda/(L+\lambda) \tag{3.12}$$

$$W_0^{c} = \lambda/(\lambda+L) + (1-\alpha^2+\beta) \tag{3.13}$$

$$W_i^{(m)} = W_i^{(c)} = 0.5/(\lambda+L) \quad i = 1, \dots, 2L \tag{3.14}$$

where L is the dimension of the state vector (in our case 6) and $\lambda = \alpha^2(L+\eta) - L$, with α between 0 and 1, $\eta = 0$, $\beta = 2$. The expression $\left(\sqrt{(L+\lambda)\widehat{\boldsymbol{C}}_{t^{old}}}\right)_i$ indicates the ith row of the matrix square root. The generated sigma vectors are then propagated using the nonlinear function

$$\boldsymbol{\mathcal{X}}_{i,t_{obs,1}^{new}} = \boldsymbol{g}\left(\boldsymbol{\mathcal{X}}_{i,t^{old}}\right) \qquad i = 0, \dots, 2L \tag{3.15}$$

and the mean and the covariance for the state estimate $\overline{\boldsymbol{X}}_{t_{obs,1}^{new}}$ are obtained using a weighted sample mean and covariance of the posterior sigma points

$$\overline{\boldsymbol{\mu}}_{t_{obs,1}^{new}} \approx \sum_{i=0}^{2L} W_i^{(m)} \boldsymbol{\mathcal{X}}_{i,t_{obs,1}^{new}} \tag{3.16}$$

$$\overline{\boldsymbol{C}}_{t_{obs,1}^{new}} \approx \sum_{i=0}^{2L} W_i^{(c)} \left\{\boldsymbol{\mathcal{X}}_{i,t_{obs,1}^{new}} - \overline{\boldsymbol{\mu}}_{t_{obs,1}^{new}}\right\}\left\{\boldsymbol{\mathcal{X}}_{i,t_{obs,1}^{new}} - \overline{\boldsymbol{\mu}}_{t_{obs,1}^{new}}\right\}^{\mathrm{T}} \tag{3.17}$$

The UT, therefore, provides an a priori estimate of the state vector of the object at the epoch of the new passage.

The second phase of the OD refinement consists in updating the a priori estimate on the basis of the available measurements. The transit of the object is characterized by a vector of time instants $t_{obs}^{new} = \{t_{obs,1}^{new}, \dots, t_{obs,N_{obs}}^{new}\}$, where N_{obs} is the number of time instants for which the measured SNR is larger than the imposed threshold. For each time instant t_k, a vector of observations $\boldsymbol{y}_k$ is available. This vector for SRT consists of a single Doppler shift measurement. Starting from the a priori estimate $\overline{\boldsymbol{X}}_{t_{obs,1}^{new}}$ and the available vectors of measurements, the state update is performed with a sequential Kalman filter, namely the Unscented Kalman Filter (UKF) [23]. The UKF represents an evolution of the Extended Kalman Filter, in which the time update of the state estimate is performed by relying on the generated sigma points rather than computing the Jacobian of the transformation. Following the description offered in [23], the algorithm starts by initializing with $\widehat{\boldsymbol{\mu}}_0 = \overline{\boldsymbol{\mu}}_{t_{obs,1}^{new}}$ and $\boldsymbol{C}_0 = \overline{\boldsymbol{C}}_{t_{obs,1}^{new}}$. Then, for $k = 1, .., N_{obs}$, if we indicate with $\gamma = \sqrt{L + \lambda}$, we have

Sigma points computation

$$\boldsymbol{\mathcal{X}}_{k-1} = \left[\widehat{\boldsymbol{\mu}}_{k-1} \quad \widehat{\boldsymbol{\mu}}_{k-1} + \gamma\sqrt{\boldsymbol{C}_{k-1}} \quad \widehat{\boldsymbol{\mu}}_{k-1} - \gamma\sqrt{\boldsymbol{C}_{k-1}}\right] \tag{3.18}$$

Time update

$$\boldsymbol{\mathcal{X}}_{k|k-1} = \boldsymbol{g}(\boldsymbol{\mathcal{X}}_{k-1}) \tag{3.19}$$

$$\widehat{\boldsymbol{\mu}}_k^- = \sum_{i=0}^{2L} W_i^{(m)} \boldsymbol{\mathcal{X}}_{i,k|k-1} \tag{3.20}$$

$$\boldsymbol{C}_k^- = \sum_{i=0}^{2L} W_i^{(c)} \left[\boldsymbol{\mathcal{X}}_{i,k|k-1} - \widehat{\boldsymbol{\mu}}_k^-\right]\left[\boldsymbol{\mathcal{X}}_{i,k|k-1} - \widehat{\boldsymbol{\mu}}_k^-\right]^{\mathrm{T}} \tag{3.21}$$

$$\boldsymbol{\mathcal{Y}}_{k|k-1} = \boldsymbol{h}\left(\boldsymbol{\mathcal{X}}_{k|k-1}\right) \tag{3.22}$$

$$\widehat{\boldsymbol{y}}_k^- = \sum_{i=0}^{2L} W_i^{(m)} \boldsymbol{\mathcal{Y}}_{i,k|k-1} \tag{3.23}$$

Measurement update

$$\boldsymbol{C}_{\tilde{\boldsymbol{y}}_k\tilde{\boldsymbol{y}}_k} = \sum_{i=0}^{2L} W_i^{(c)} \left[\boldsymbol{\mathcal{Y}}_{i,k|k-1} - \widehat{\boldsymbol{y}}_k^-\right]\left[\boldsymbol{\mathcal{Y}}_{i,k|k-1} - \widehat{\boldsymbol{y}}_k^-\right]^{\mathrm{T}} + \boldsymbol{R}^n \tag{3.24}$$

$$\boldsymbol{C}_{\boldsymbol{\mu}_k \boldsymbol{y}_k} = \sum_{i=0}^{2L} W_i^{(c)} \left[\boldsymbol{\mathcal{X}}_{i,k|k-1} - \widehat{\boldsymbol{\mu}}_k^-\right] \left[\boldsymbol{\mathcal{Y}}_{i,k|k-1} - \widehat{\boldsymbol{y}}_k^-\right]^{\mathrm{T}} \tag{3.25}$$

$$\boldsymbol{\mathcal{K}}_k = \boldsymbol{C}_{\boldsymbol{\mu}_k \boldsymbol{y}_k} \boldsymbol{C}_{\tilde{\boldsymbol{y}}_k \tilde{\boldsymbol{y}}_k}^{-1} \tag{3.26}$$

$$\widehat{\boldsymbol{\mu}}_k = \widehat{\boldsymbol{\mu}}_k^- + \boldsymbol{\mathcal{K}}_k (\boldsymbol{y}_k - \widehat{\boldsymbol{y}}_k^-) \tag{3.27}$$

$$\boldsymbol{C}_k = \boldsymbol{C}_k^- - \boldsymbol{\mathcal{K}}_k \boldsymbol{C}_{\tilde{\boldsymbol{y}}_k \tilde{\boldsymbol{y}}_k} \boldsymbol{\mathcal{K}}_k^{\mathrm{T}} \tag{3.28}$$

In the previous formulation, $\boldsymbol{R}^n$ indicates the measurement noise matrix, $\boldsymbol{y}_k$ is the vector of real observations at time epoch t_k, i.e. Doppler shift, whereas $\boldsymbol{h}$ is the nonlinear transformation to pass from the state estimate to the observation vector estimate $\boldsymbol{\mathcal{Y}}_{k|k-1}$.

The algorithm is repeated for all the observation instants t_k of the investigated passage. The result, in the end, is an updated estimate of the state vector of the object at the epoch of the last observation instant $\widehat{\boldsymbol{X}}_{t_{obs,N_{obs}}^{new}} \sim \mathcal{N}\left(\widehat{\boldsymbol{\mu}}_{t_{obs,N_{obs}}^{new}}, \widehat{\boldsymbol{C}}_{t_{obs,N_{obs}}^{new}}\right)$. This new estimate replaces the old available estimate, thus updating the database. The described procedure is repeated for all the passages of the list. Every time a new passage of a given object is planned, its state estimate is retrieved from the database, it is propagated from its time epoch to the epoch of the new passage and eventually updated. If the OD refinement process is successful, the new estimate replaces the old one in the database, and so on.

Table 8 shows the evolution of the state estimate accuracy for object NORAD ID 00730 in terms of error in position and velocity (ε_p and ε_v) and standard deviation in position and velocity (σ_p and σ_v) obtained without performing OD refinement ("*free*" subscript) and updating the estimate with the UKF ("*OD*" subscript). For the case under study, only Doppler shift measurements are considered for the measurement update phase of the UKF. The first line shows the initial accuracy of the available estimate, whereas the second line shows the accuracy of the estimate at the epoch of the first available measurement of the first object passage. As can be seen, the errors in position and velocity increase of four and three orders of magnitude, respectively, in slightly less than two days. The third line shows a comparison between the result obtained at the end of the UKF (left) and what would be obtained without performing OD: the UKF guarantees an improvement in both position and velocity accuracy of around three orders of magnitude. Nevertheless, the uncertainty of the estimate obtained at the end of the UKF in both position and velocity is relatively large with respect to the actual errors (2.86 km and 4.17 m/s, respectively). This aspect has an unavoidable drawback in the accuracy of the results obtained when the estimate is propagated. Lines four and five show the comparison between the refined estimate and the old one when propagated one day and two days after the UKF epoch, respectively. As can be seen, the error of the updated estimate rapidly increases in time, and after one day the accuracy of the updated estimate is already lower than the accuracy of the old estimate. That is, the refinement effect granted by the UKF is already lost.

*Table 8 - Doppler-only performance for object NORAD ID 00730 at different time epochs, in terms of error in position and velocity (ε_p and ε_v) and standard deviation in position and velocity (σ_p and σ_v) obtained performing OD refinement ("*OD*" subscript) or without updating the estimate ("*free*" subscript).*

EPOCH (UTC)	$\boldsymbol{\varepsilon_{p,OD}}$ (KM)	$\boldsymbol{\sigma_{p,OD}}$ (KM)	$\boldsymbol{\varepsilon_{v,OD}}$ (M/S)	$\boldsymbol{\sigma_{v,OD}}$ (M/S)	$\boldsymbol{\varepsilon_{p,free}}$ (KM)	$\boldsymbol{\sigma_{p,free}}$ (KM)	$\boldsymbol{\varepsilon_{v,free}}$ (M/S)	$\boldsymbol{\sigma_{v,free}}$ (M/S)
26/07/2019 00:00:00	-	-	-	-	1.76e-2	2.45e-1	4.16e-1	1.73
27/07/2019 21:46:25	-	-	-	-	1.26e2	5.01e2	1.27e2	5.08e2
27/07/2019 21:48:09	2.46e-1	2.86	3.41e-1	4.17	1.26e2	5.01e3	1.27e2	5.08e2
28/07/2019 21:48:09	2.35e2	1.80e3	2.39e2	1.83e3	1.93e2	7.63e2	1.96e2	7.74e2
29/07/2019 21:48:09	8.82e2	3.76e3	9.01e2	3.82e3	2.62e2	1.03e3	2.66e2	1.04e3

As previously mentioned, this trend can be explained considering the large size of the covariance matrix obtained at the end of the UKF, which in turn is mainly affected by the fact that only Doppler shift measurements are used. In order to have a better description of the behavior of the sensor, the OD refinement procedure previously described was applied to all the objects included in the list of 355 objects. For each object, the initial estimate obtained with Equation 3 and 7 is propagated to the epoch of the first passage, an updated estimate is obtained, and this estimate is propagated again, till a new passage is considered or the final simulation epoch (02 August 2019 00:00:00 UTC) is reached. Each object can be therefore associated with a final state estimate, and its errors in position and velocity and standard deviations in position and velocity are obtained. The procedure is repeated for all the objects of the list. The obtained errors and standard deviations are then sorted, and a distribution is obtained. Table 9 shows a comparison of the median of the errors and standard deviations distributions obtained both performing OD refinement ("*OD*") and without updating the estimate ("*free*"). In addition, the median of the indexes I_p and I_v is shown. These two indexes are computed as

$$I_p = \sigma_{p,OD}/\sigma_{p,free} \tag{3.29}$$

$$I_v = \sigma_{v,OD}/\sigma_{v,free} \tag{3.30}$$

and they measure the effectiveness of the UKF process in reducing the size of the estimate uncertainty. As can be seen, the results follow the trend of the previous example: the estimates obtained by performing OD refinement show larger errors and uncertainty. That is, the UKF approach apparently seems to worsen the accuracy of the estimate.

*Table 9 - Doppler-only orbit determination (OD) performance in terms of median (50% superscript) of the error in position and velocity (ε_p and ε_v) and standard deviation in position and velocity (σ_p and σ_v) obtained with ("*OD*" subscript) and without ("*free*" subscript) OD refinement, and median of the I_p and I_v indexes. All quantities are referred to epoch 02 August 2019 00:00:00 UTC.*

$\boldsymbol{\varepsilon_{p,OD}^{50\%}}$ (KM)	$\boldsymbol{\sigma_{p,OD}^{50\%}}$ (KM)	$\boldsymbol{\varepsilon_{v,OD}^{50\%}}$ (KM/S)	$\boldsymbol{\sigma_{v,OD}^{50\%}}$ (KM/S)	$\boldsymbol{\varepsilon_{p,free}^{50\%}}$ (KM)	$\boldsymbol{\sigma_{p,free}^{50\%}}$ (KM)	$\boldsymbol{\varepsilon_{v,free}^{50\%}}$ (KM/S)	$\boldsymbol{\sigma_{v,free}^{50\%}}$ (KM/S)	$\boldsymbol{I_p^{50\%}}$	$\boldsymbol{I_v^{50\%}}$
1.76E3	3.19e3	1.74	3.11	4.80e2	1.85e3	4.47e-1	1.83	1.72	1.74

The weakness shown by Doppler-only OD refinement can be solved by including slant range measurements. The slant range is the sum of the distance of the transiting object from the receiver and the transmitter. We show here an analysis of the performance of BIRALET considering a future upgrade of the sensor, in which slant range measurements will be available.

A 1σ accuracy of 10 m is assumed for the simulated slant range measurements. If slant range measurements are included, the size of the covariance matrix obtained at the end of the UKF process decreases, and this has a positive effect on the accuracy of the propagated estimate. Figure 33 shows the trend of the error in position (Figure 33a) and error in velocity (Figure 33b) obtained without OD refinement (black line), with Doppler-only UKF (green), and range-Doppler measurements (blue) for object NORAD ID 00730. Squares and triangles represent the errors at the beginning and at the end of each UKF process, respectively. As can be seen, while the accuracy of the state estimate at the end of the first UKF is similar for Doppler-only and range-Doppler OD refinement, the evolution in time is very different: the Doppler-only estimate accuracy rapidly decreases, and after the second UKF the results become unreliable. With range-Doppler measurements, instead, the error remains limited and below what can be obtained without performing OD refinement, and the average accuracy increases as the number of processed passages increases. Table 10 shows the same comparison shown in Table 9. In this case, range-Doppler measurements are considered. As can be seen,

now the use of the UKF allows us to reduce the errors in position and velocity of a factor 3 and obtain an overall reduction of the size of the covariance of around one order of magnitude.

Table 10 - Range-Doppler OD performance in terms of median (50% superscript) of the error in position and velocity (ε_p and ε_v) and standard deviation in position and velocity (σ_p and σ_v) obtained with ("OD" subscript) and without ("free" subscript) OD refinement, and median of the I_p and I_v indexes. All quantities are referred to epoch 02 August 2019 00:00:00 UTC.

$\boldsymbol{\varepsilon_{p,OD}^{50\%}}$ (KM)	$\boldsymbol{\sigma_{p,OD}^{50\%}}$ (KM)	$\boldsymbol{\varepsilon_{v,OD}^{50\%}}$ (KM/S)	$\boldsymbol{\sigma_{v,OD}^{50\%}}$ (KM/S)	$\boldsymbol{\varepsilon_{p,free}^{50\%}}$ (KM)	$\boldsymbol{\sigma_{p,free}^{50\%}}$ (KM)	$\boldsymbol{\varepsilon_{v,free}^{50\%}}$ (KM/S)	$\boldsymbol{\sigma_{v,free}^{50\%}}$ (KM/S)	$\boldsymbol{I_p^{50\%}}$	$\boldsymbol{I_v^{50\%}}$
1.19E2	1.98e2	1.15e-1	1.91e-1	4.81e2	1.85e3	4.47e-1	1.83	1.09e-1	1.09e-1

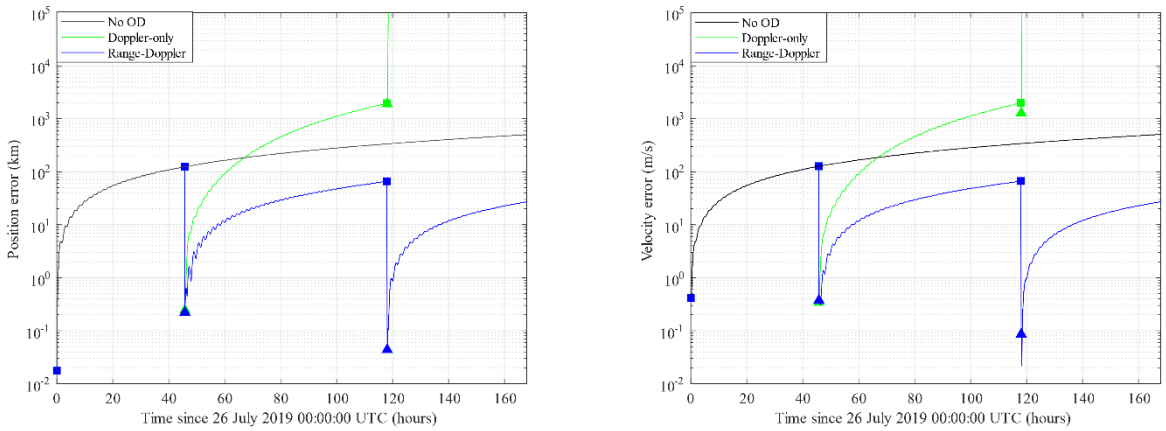

(a) **(b)**

Figure 33 - Object NORAD ID 00730, error in position (a) and velocity (b) as a function of time without performing OD refinement (black line), with Doppler-only (green) and range-Doppler (blue) OD refinement. Squares and triangles represent the error before and after the UKF, respectively.

These results provide a general overview of the possible performance of BIRALET sensor for space objects tracking: Doppler shift measurements alone cannot grant accurate results for the OD refinement process, the OD improvement obtained with the UKF is rapidly lost as the error evolves in time, i.e. the growth of the error is larger than what would be obtained without OD refinement. Conversely, the combined use of Doppler shift and slant range measurements guarantees a significant improvement.

4. Advantages of Using a C-band Phased Array Feed as a Receiver in the Sardinia Radio Telescope for Space Debris Monitoring

One of the limitations of the P-band BIRALET system is the relatively low pointing speed of the SRT (0.5 deg/sec in azimuth, 0.85 deg/sec in elevation) and the availability of only one beam (HPBW of 0.8 degrees), resulting in a limited Field of View (FoV). Space debris with angular speed greater than the maximum antenna angular movement cannot be tracked as the antenna would be too slow to follow their apparent motion in the sky. Imaging the sky with a multi-beam array receiver installed at the primary focus of the SRT would increase the telescope FoV and the survey speed (how quickly we can image a given area of sky to a given sensitivity level), assuming that the receiver sensitivity in not compromised with respect to that of a single-pixel feed. This allows to have a good spatial resolution and an increased FoV which permits to cover a greater portion of the sky in less time with respect to mono-beam observations, such as the case of the P-band BIRALET system described in Section 2.

As a matter of fact, one of the open-ended frontiers of the instrumentation for radio telescopes is the increase of the FoV. This could be obtained using a Phased Array Feed (PAF), also known as a Focal Plane Array (FPA), onto the primary focus of a radio telescope [25]. In particular, a PAF consists of closely packed antenna elements with about half wavelength element separation that, by spatially sampling the focal plane, can synthesize multiple independent beams and be set to Nyquist-sample the sky. Multiple beams are formed by electronically adding the signals from different groups of radiating elements of the array. An antenna element can contribute to form multiple beams. The properties of the beams can be optimized over a wide range of frequencies by electronically controlling each element phase and amplitude (complex weights) leading to high aperture efficiency and low spillover.

Figure 34 depicts a Focal Plane Array (FPA) at the primary focus of a telescope and shows that plane waves from different sky directions are focused on different areas of the FPA. The linear size of the electric field distribution on the focal plane is of order $f\lambda/D$, where λ is the wavelength, D the telescope aperture diameter and f its focal length. For a given direction ϑ, within a relative small region (FoV) close to the boresight direction, it is possible to maximize the coupling to a plane wave without a significant efficiency loss using a suitable illumination of the telescope aperture that provides a wavelength-dependent telescope resolution, in terms of HPBW given by $\vartheta_{3dB} \approx \lambda/D$. Instead, in first approximation, the angle of the off-axis far-field direction ϑ with respect to the boresight is wavelength-independent and scales as the ratio $\vartheta \approx d/f$, where d is the distance from the on-axis geometrical focus and the area of the focal plane excited by the off-axis source (location of the focal field distribution due to the incoming off-axis wave). Therefore, multiple beams can be pointed to different directions on the sky by suitably exciting different focal plane areas (different sub-arrays of the FPA). The antennas on the focal plane array have to be designed to efficiently sample the focal plane fields and to avoid generation of grating lobe responses, while minimizing the noise performance of the receiver chains (by accounting of mutual coupling effects).

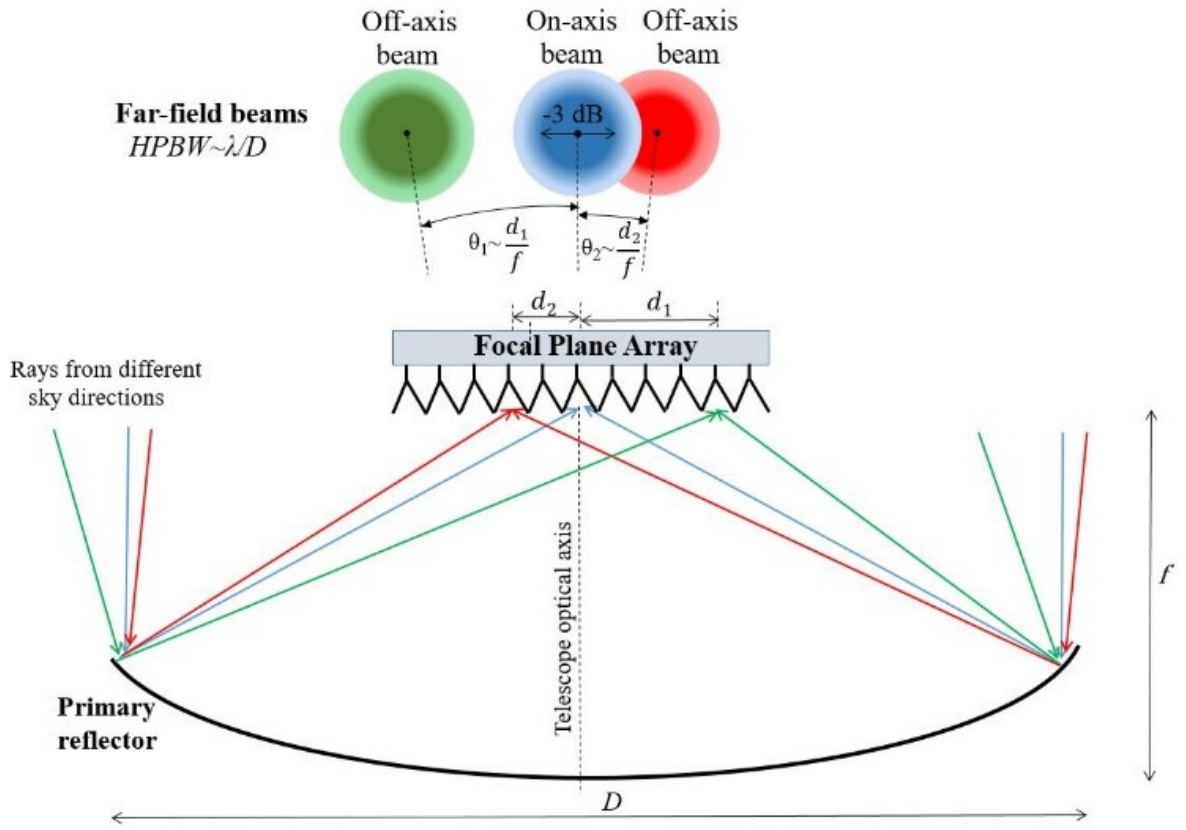

Figure 34 - Bottom: Schematic of a FPA at the primary focus of an axially symmetric single dish parabolic reflector with diameter D and focal length f. Plane waves from three different sky directions (on-axis in blue, off-axis in green and red) excite different areas of the FPA. Top: Far field patterns (angular size □□/D) and angular displacements from boresight (□d/f) resulting from the excitation of the different areas of the FPA at distance d from the axis.

Through the beam-forming process, PAFs are able to synthesize multiple beams and optimize each of them. The beam shapes and side lobes can be modified in real time and be set to minimize their response towards undesired Radio Frequency Interferences (RFI). Some radio astronomy phased arrays have been developed for astronomical research, such as the Low Frequency Array (LOFAR) and its expansion LOFAR2.0, a phased array radio telescope based in The Netherlands with extensions throughout Europe [25]; the Murchison Widefield Array (MWA) telescope, located in the remote Murchison region of Western Australia [25] and the Australian SKA Pathfinder (ASKAP), a world-class high-dynamic range wide-field-of-view survey instrument [25]. ASKAP utilizes a PAF at the focus of each of its antennas, while LOFAR and MWA are phased array operating in aperture array mode. The technologies adopted in these radio telescopes contribute to develop the Square Kilometer Array (SKA) [25].

As previously described, a multi-beam receiver installed at the focal plane of a telescope increases its FoV and a greater portion of the sky can be covered in less time with respect to a mono-beam observation. We point out that the development of a multi-beam system requires to carry out a dedicated feasibility study, followed by a long process of simulations, prototyping, verification, production, assembly and final characterization. A PAF is an array of closely packed antenna elements placed at the focal plane of a large dish. The PAF array is set to Nyquist sample the electromagnetic field in the focal plane. Beams can be formed by analog methods, for example by introducing delays between elements and by managing the electrical lengths of the transmission lines, and by proper weighting in phase and amplitude the signals from the different PAF elements. This approach tends to be simple and cost effective, but restrictive. A better option is to form the beams digitally using signal processors. This method is highly flexible because any weights can be update in real time to form arbitrary beams. A disadvantage of the digital beam-former is the

computational process, which is very intensive. Either way, it is necessary to include a beam-former in the signal path, adding complexity to the telescope system.

4.1 The SRT as a tracking Multi-beam system

The data obtained from the measurement campaigns are used in input at orbit determination algorithms. The observational data will usually consist of such measurements as range, Doppler shift, azimuth and elevation pointing, or other observable quantities. However, for the space debris orbit determination problem, the minimal set of necessary parameters are the position and velocity vectors at some given epoch. Therefore, the state variables (position, velocity, unknown model parameters, etc.) will not be observed, but rather the observable will usually be some nonlinear function of the state variables [25]. After an estimate of the apparent space debris trajectory on the sky from the SRT site has been obtained, the subsequent motion and other values can be predicted for the observations. These predicted values will differ from the true values because of inaccuracies in the estimated state vector (i.e., position and velocity vector) caused by errors in the orbit determination process, such as approximations involved in the method of orbit improvement and in the mathematical model, errors in the observations, errors in the computational procedure used in the solution process. Consequently, the process of observation and estimation must be repeated continuously as the space debris motion evolves [25]. Thus, for each space debris observation it would be advantageous to have a multi-beam systems multiple information are obtained in a unique antenna pointing with respect to a mono-beam system. In the case of a mono-beam system, for each mechanical antenna pointing, there is a unique reference point for the measured data (Doppler and/or range measurement, received SNR) of each observed debris. Instead, when a multi-beam system is employed the number of reference points matches the number of beams. When an object transits inside the antenna FoV, beams are illuminated by the reflected radio waves. By looking at the beam illumination sequence, it is possible to estimate the ground track of the transiting object, with a higher level of detail with respect to a single-beam system [25].

4.2 The advantages using C-band respect to P-band

Another important aspect regards the observing frequency of the BIRALET system. As shown in Table I, in P-band (at 410 MHz), the gains of the SRT and of the TRF are equal to 46.6 dBi and 27.3 dBi, respectively. As shown in Table 11, two objects could not be detected in the measurement campaign of December 13, 2018. If the BIRALET system were upgraded for operation to higher frequencies, in particular to C-band at 6 GHz the received SNR from the debris and the chances of detection would considerably increase. Table III lists the estimated SNR at 410 MHz and at 6 GHz, for the two debris that were not detected in the previous campaign. The estimated values are obtained with the radar equation [25] and considering an ideal noise floor in a noise bandwidth of 30 Hz.

Table 11 - received SNR: P-band vs C-band.

OBJECT ID	SLANT RANGE [KM]	RCS [M^2]	RECEIVED SNR AT 410 MHZ [DB]	RECEIVED SNR AT 6 GHZ [DB]

#25415	1853.70	0.55	33.8	57.1
#22824	2838.18	0.16	21.1	44.4

The analysis of the results of Table 11, we can conclude that space debris with RCS lower than 0.5 m^2 and for slant ranges greater than 1800/2000 km, the P-band BIRALET system is to the edge of its capabilities in terms of detection sensitivity. We point out that these SNRs are estimated by assuming an ideal noise floor. In the real case, the noise floor is higher and the SNR lower. Upgrading the BIRALET from 410 MHz to 6 GHz would increase the SRT and the TRF's antenna gains by about 23 dB as reported in Table 12, thus improving the expected SNR:

Table 12 - Characteristics of the C-band BIRALET system.

ANTENNA NAME	**SRT**	**TRF**
FREQUENCY	6 GHz	6 GHz
ANTENNA GAIN	69.9 dBi	50.6 dBi
HALF POWER BEAM WIDTH (HPBW)	0.05 deg	0.5 deg
AZIMUTH SPEED	0.85 deg/sec	3 deg/sec
ELEVATION SPEED	0.5 deg/sec	3 deg/sec

The HPBW in Table 12 refers to one antenna beam in C-band. The HPBW scales approximately inversely to frequency (at C-band the HPBW are smaller than at 410 MHz). The reduction of FoV due to operation at higher frequency can be (partially) compensated by a PAF, generating multiple independent beams.

Therefore, a C-band PAF installed in the SRT can improve the system performances in terms of minimum sizes of the observed objects.

5. The PHAROS2 system

PHAROS (Phased Arrays for Reflector Observing Systems) [26-28] is a cryogenically cooled PAF demonstrator with analogue beam-former based on an array of dual-polarization 10×11 Vivaldi antennas designed for radio astronomy observation across the 4-8 GHz band. The array, shown in Figure 35, is cooled to 20 K along with 24 low noise amplifiers (LNAs) mounted directly behind the array elements.

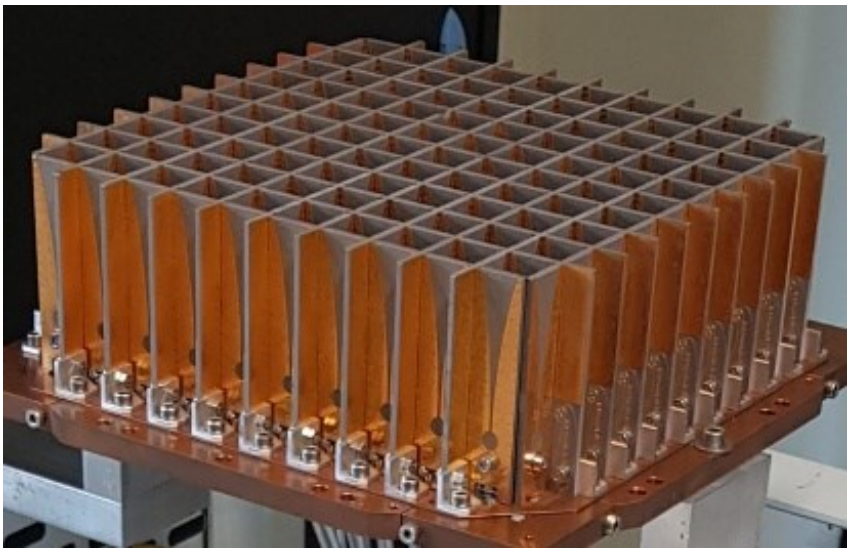

Figure 35- PHAROS array of 10×11 Vivaldi dual polarization antennas. Only the 24 central elements of the array are used for beamforming, the rest are matched terminated.

PHAROS2 [8], the upgrade of PHAROS, is a cryogenically cooled PAF with digital beam-former for the 4-8 GHz band. The instrument is under development in the framework of the PAF SKA (Square Kilometer Array) [9] advanced instrumentation program. PHAROS2 is a technology demonstrator resulting from the international collaboration between the Italian National Institute for Astrophysics (INAF), Jodrell Bank Observatory at the University of Manchester (UK), ASTRON (the Netherlands), the University of Malta (Malta) and the University of Chalmers (Sweden).

A block diagram of the PHAROS2 PAF is illustrated in Figure 36. The PAF features the following:

- a cryostat enclosing the PHAROS array of cryogenically cooled Vivaldi antennas, in which a sub-array of 24 antenna elements is cascaded with new generation LNAs with state-of-the-art performance (to reduce the system noise temperature);
- a 2.3-8.2 GHz room-temperature “Warm Section” (WS) multi-channel receiver;
- an FPGA-based Italian Tile Processing Module (iTPM) digital backend [28] capable of digitizing and synthesizing four independent beams across a ≈275 MHz IF band from a sub-array of 24 antenna elements.

The development of the PHAROS2 cryogenic section is in charge to the University of Manchester and to the University of Chalmers, while the development of the warm receiver section (WS) and of the digital backend and beam-former, described in this paper, are in charge to INAF and to the University of Malta. The main specifications of the WS and of the digital backend are listed in Table I. The WS is required to handle up to 32 RF input signals, although only 24 will be used for PHAROS2. We note that the frequency range of the WS receiver, 2.3–8.2 GHz (fmax/fmin ≈ 3.6), is greater than the one delivered by the PHAROS2 Vivaldi array

cryogenic section (4–8 GHz). Therefore, the WS and the associated digital backend can be used not only with PHAROS2, but also with other PAF antenna arrays that could be developed to cover 2.3–8.2 GHz.

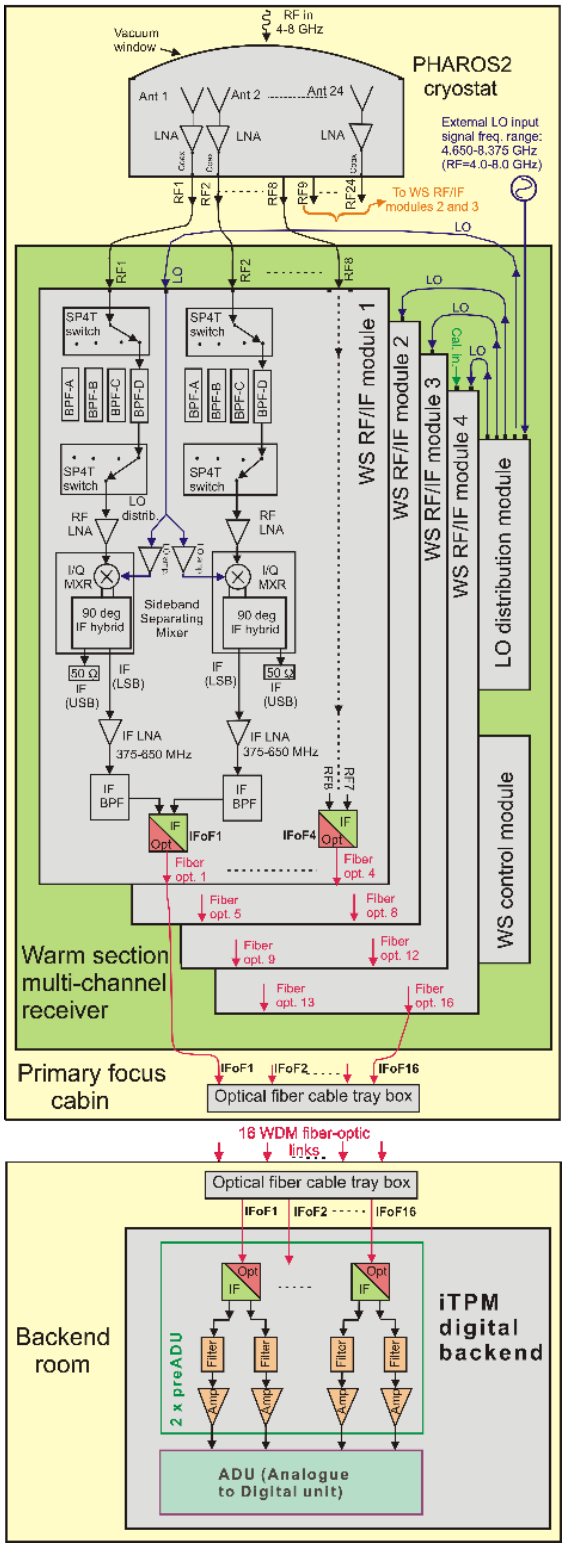

Figure 36 - Block diagram of the PAF receiver chain showing the PHAROS2 cryostat (top), the Warm Section multi-channel receiver (middle) and the iTPM digital backend (bottom). The schematic of the Warm Section multi-channel receiver, located in the primary focus receiver room, is enclosed by the green background rectangle.

The WS is a necessary piece of hardware for PAFs designed to operate beyond few GHz, as a direct sampling of the RF signal by analog to digital converters (ADCs) is currently possible up to several GHz. The existing high-performance ADCs have enough bits of resolution (typically 8–12) to operate in moderate radio frequency interference (RFI) environment, but limited bandwidth and maximum frequency, which makes them suitable solutions for PAFs radio astronomy application up to S-band (or lower frequency), but not yet for 4–8 GHz or beyond.

In Section 5.1 the PHAROS Vivaldi antenna array is presented. The design, construction, assembly and test of the PHAROS2 warm receiver section is discussed in Section 5.2, while the development of the digital backend and beam-former is discussed in Section 5.3.

The PHAROS2 project aims at assembling, testing and installing the full PHAROS2 instrument (cryogenic section plus warm receiver section and digital backend) onto the 25-m diameter Pickmere radio astronomy antenna at the Jodrell Bank Observatory (operated by the University of Manchester), in order to conduct the technical and scientific commissioning that will refine the calibration and characterization of the PHAROS2 system. These will enable first-ever radio astronomy observations in C-band with a cryogenic PAF. Test results of the fully assembled PHAROS2 system on the radio astronomy antenna will be reported in a future paper.

Table 13 - PHAROS2 warm Section and backend Specifications.

Warm receiver section	Number of RF channels	32 (four × eight-channel RF/IF modules). 24 used.
	RF band	2.3-8.2 GHz
	Frequency conversion scheme	Sideband Separating Mixer in LSB (USB terminated)
	LO band	2.950-8.575 GHz
	IF band	375-650 MHz
	Switched filter banks: Band Pass Filter freq. range and LO freq.	BPF-A: 2.300-8.200 GHz; LO tuning fLO=2.95-8.575 GHz
		BPF-B: 4.775-5.050 GHz; fixed fLO=5.425 GHz
		BPF-C: 5.780-6.055 GHz; fixed fLO=6.430 GHz
		BPF-D: 6.445-6.720 GHz; fixed fLO=7.095 GHz
	Signal transportation	Two IF output signals transported over a single optical fiber (IFoF) using WDM
	Number of WDM fiber-optics transmitters	16
	Control module	Optical fiber-Ethernet mediaconverter and microcontroller for BPF selection, LO power and PCB temperature monitoring

iTPM Digital backend	Number of WDM fiber-optics receivers	16
	ADCs	16 × dual-ADCs AD9680, 1 GS/s, ENOB=10.8
	FPGAs	2 × Xilinx Kintex Ultrascale XCU40 20 nm
	Number of synthesized beams and instantaneous coverage	Four beams implemented in the iTPM FPGAs for 24 antenna elements with 275 MHz bandwidth
	N. of frequency channels and resolution	512 channels, 0.81 MHz/ch. (32/27 overlapping factor)

5.1 PHAROS Vivaldi array

The PHAROS Vivaldi antenna array shown in Figure 35 utilizes high-performance Taconic PCBs (TLY-5 substrate, with εr=2.20, tanδ=0.0008) with three-layer laminated board structure, based on two 1.14 mm thick substrates [26]. The antenna feed element is a stripline on the center conductor layer, sandwiched between the two board laminates. The complete PHAROS focal plane array antenna was built with 11 boards in both the x and the y directions, each integrating 10 Vivaldi elements with 21 mm spacing (Figure 37). The spacing-to-wavelength ratio is 0.56 at the PHAROS/PHAROS2 maximum operating frequency of 8 GHz (λ_{min}≈37.5 mm). The overall size of the array on the x-y plane is ≈230×230 mm2, i.e. ≈6λ_{min}×6λ_{min} (and equivalently ≈3λ_{max}×3λ_{max} for λ_{max}≈75 mm, relative to the 4 GHz minimum frequency).

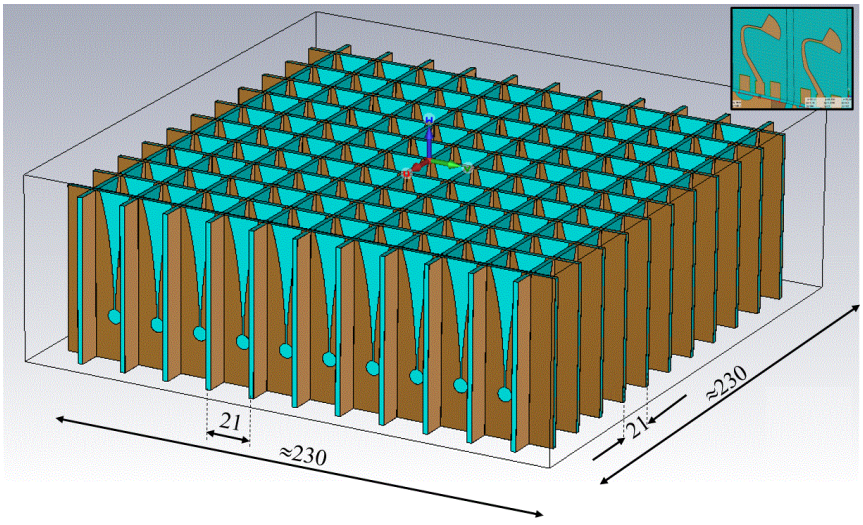

Figure 37- 3D view of the PHAROS array of 10×11 dual-polarization Vivaldi antenna elements. Dimensions are in mm. The inset on the top right shows the detail of two of the antenna stripline feed elements.

A subset of 24 elements of the dual-polarization 10×11 Vivaldi antennas (220 elements) are connected to LNAs, the rest are matched terminated. The 24 active elements are located at the center of the array and excite the same polarization channel (antennas oriented on the y-plane). In PHAROS, a 13-element subarray

of the 24 active elements (Figure 38) is connected to a cryogenically cooled analogue beam-former. PHAROS was designed to integrate four identical analogue beam-formers capable of forming four independent beams, each using a different combination of 13 elements of the 24 active ones. Some of the elements contribute to form more than one beam. Instead, in PHAROS2 all of the 24 same-polarization active antenna elements contribute to form each of the four independent beams synthesized by the digital backend.

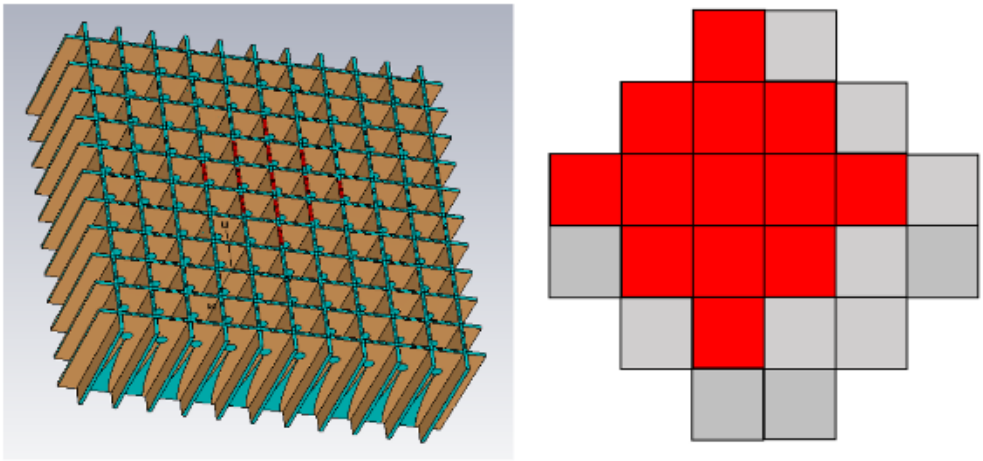

Figure 38 - Sub-array of 13 Vivaldi elements of the 24 active antennas connected to one analogue beam-former of the PHAROS PAF. Excited stripline antenna ports of Beam 1 (in red) and subset of the 24 active antennas (right panel).

5.1.1 3D simulation of PHAROS Vivaldi array and beam pattern (without coupling to the SRT optics)

The PHAROS Vivaldi array shown in Figure 35 utilizes high-performance Taconic PCBs (TLY-5 substrate, with ε_r=2.20, tanδ=0.0008). A three layer laminated board structure, based on two 1.14 mm thick substrates was employed [27]. The antenna feed element is a stripline on the centre conductor layer, sandwiched between the two board laminates. Figure 37 shows the 3D structure of the array that we simulated with the commercial electromagnetic software CST Microwave Studio (https://www.cst.com). The complete PHAROS FPA antenna was built with 11 boards in both the *x* and the *y* directions, each integrating 10 Vivaldi elements with 21 mm spacing. The spacing-to-wavelength ratio is 0.56 at the PHAROS maximum operating frequency of 8 GHz (λ_{min}≈37.5 mm). The overall size of the array on the *x*-*y* plane is ≈230×230 mm^2, i.e. ≈6λ_{min}×6λ_{min} (and equivalently ≈3λ_{max}×3λ_{max} for λ_{max}≈75 mm, relative to the 4 GHz minimum frequency).

The CST model of the array employs 220 ports, 110 per polarization channel (Figure 39). We excited the 24 active stripline ports of the *y*-polarization antennas of the array. These are the ports selected to be cascaded with LNAs and used for synthesizing the four beams. We calculated the S-parameters and far-field patterns generated by each Vivaldi element using the time domain solver. The model used ≈6 million meshcells. We made sure that all the stripline ports and the most critical parts of the antennas, where the highest electric field energy density is expected, were sufficiently well meshed. The computation time for the 24 ports was of order one week on a fast PC equipped with 64 GB RAM memory. The impedance of the ports is ≈33 Ω.

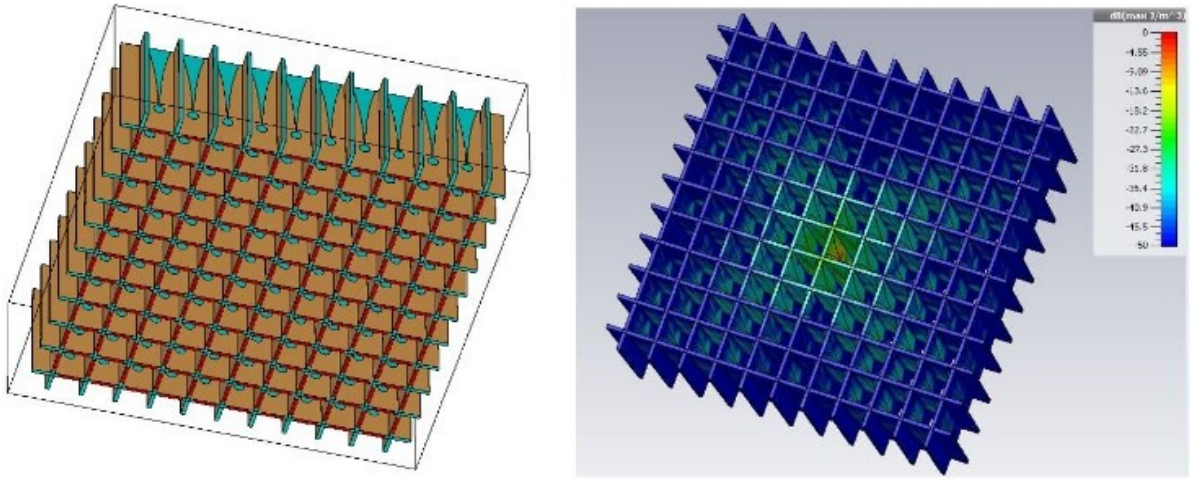

Figure 39 - Left: 3D model of the PHAROS array showing the 220 stripline ports. Right: Simulated electric energy distribution of PHAROS when exciting one of the central antenna elements (Ant. #175) aligned along the y direction at 6 GHz. The intensity of the energy distribution is color-coded through the scale given on the top right.

5.1.2 Far-field of a single Vivaldi element of the array

The right panel of Figure 39 shows the simulation results of the electric energy distribution at 6 GHz obtained by the excitation of one of the central elements of the array (Ant. #175). A relatively strong mutual coupling with the nearby elements is visible from the colour-scale image. The simulated far-field patterns of that array element at 4, 6 and 8 GHz are shown in Figure 40. The co-polar (CP) patterns are symmetric with respect to the boresight angle on the different cuts. The left side of Figure 41 plots the associated co-polar and cross polar (CX) antenna gains versus boresight angle (for the *y* polarization). The boresight gains are around 6 dBi at the three frequencies, while the HPWB are weakly frequency-dependent and have a value of ≈50 degrees at the three simulated frequencies.

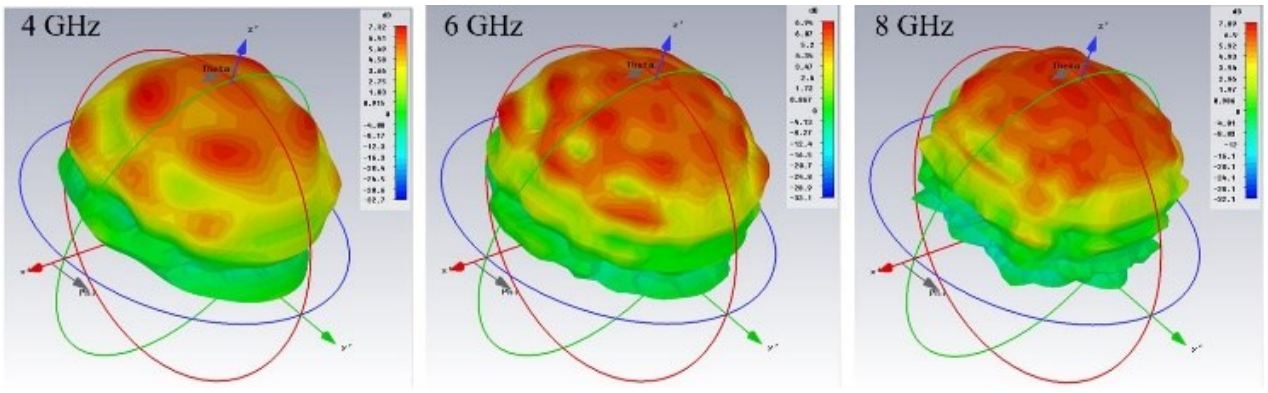

Figure 40 - 3D far-field beam pattern from Vivaldi element #175 at 4, 6 and 8 GHz simulated with CST.

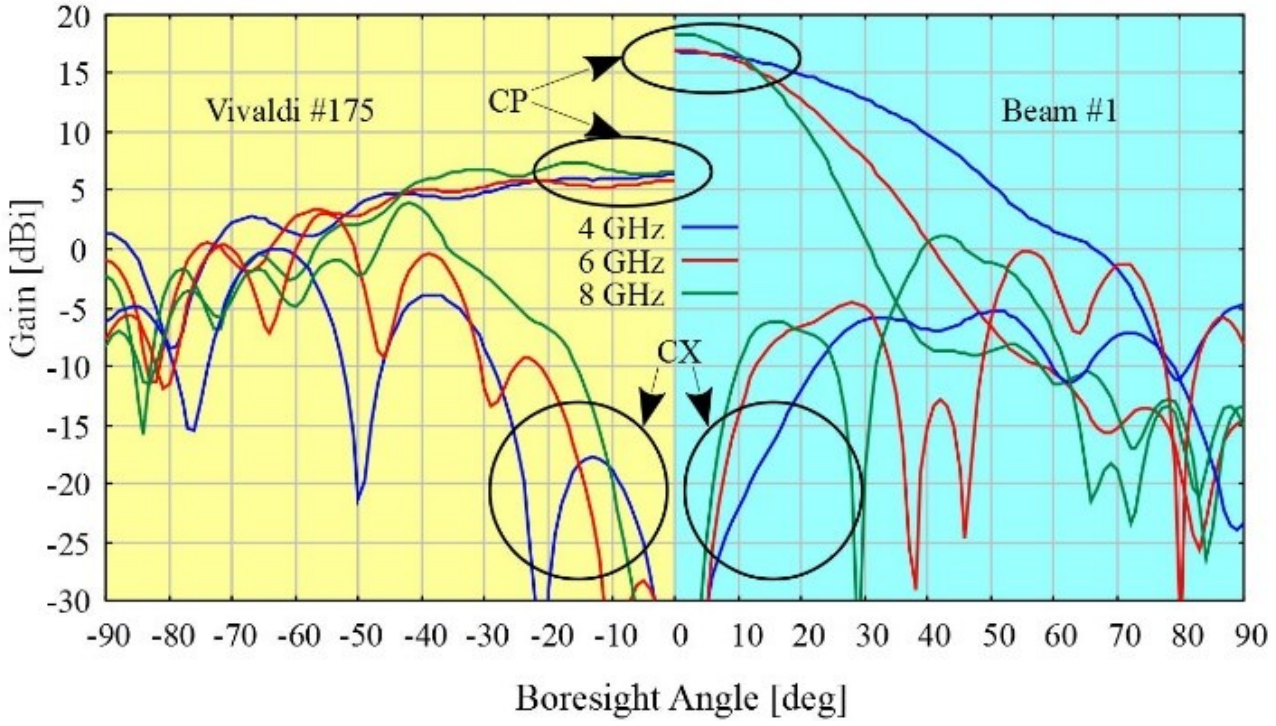

Figure 41 - Simulated antenna gains from Vivaldi element #175 (left side plots) versus Beam #1 (right side plots) formed by a linear combination of 13 elements equally fed. The plots refer to three following frequencies: 4 GHz (blue curve), 6 GHz (red curve) and 8 GHz (green curve).

5.1.3 Far-field of 13 Vivaldi elements combined

We simulated, using CST, the far-field patterns of the 24 active Vivaldi antenna elements. The PHAROS 24-element subarray was designed to form four independent beams, each utilizing a subset of 13 elements, as illustrated in Figure 42. We uniformly excited the elements of the 13-element subarrays using unitary-power normalized-weights, i.e. all equally fed in amplitude and phase. Figure 43 shows the resulting far-field beam patterns of one of the formed beams (Beam #1). The right side of Figure 41 plots the associated co-polar and cross-polar antenna gains versus boresight angle. The boresight gains are around 17 dBi at the three frequencies, and the HPBW are frequency dependent and of order 18 degrees at 6 GHz. We note that the antenna gain difference between the single element (≈6 dBi) and the 13-element sub-array (≈17 dBi) is as expected from array theory (-11.139 dB, or 1/13 in linear power scale).

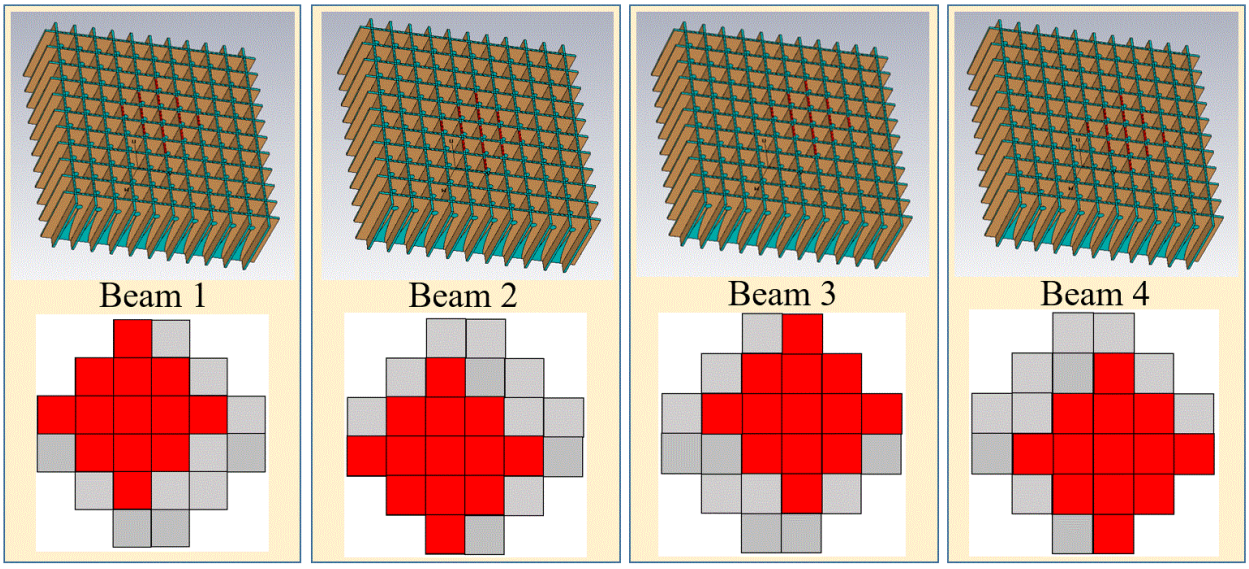

Figure 42 - Subsets of 13 Vivaldi elements of the 24 active antennas used to synthesize the four beams (Beam #1 to Beam #4).

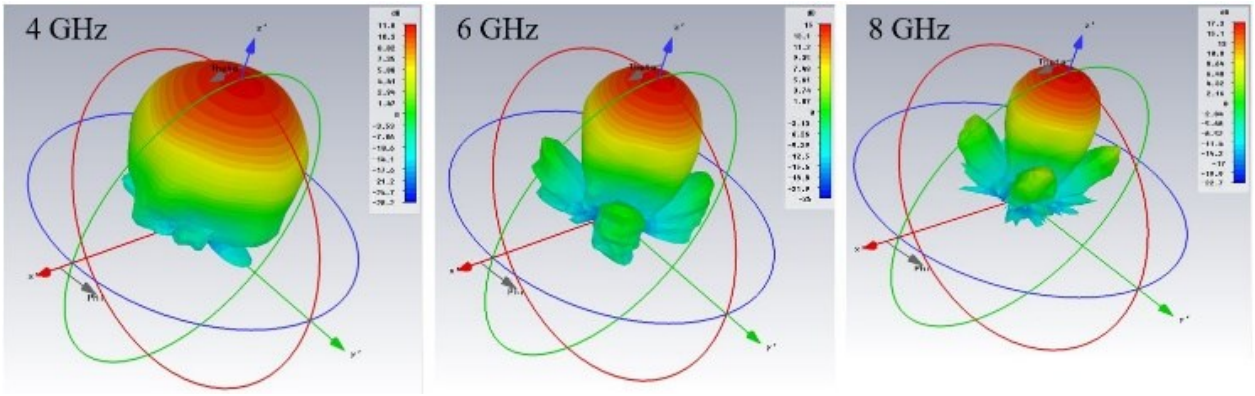

Figure 43 - 3D far-field beam patterns of Beam #1 obtained from 13 Vivaldi antenna elements equally fed both in amplitude and in phase at 4, 6, 8 GHz.

5.1.4 Co-Simulation of the PHAROS array at the SRT primary focus and coupling with the reflector

We performed electromagnetic co-simulations of the PHAROS FPA at the primary focus of the 64-m SRT dish (*f/D* =0.33), as depicted in Figure 44. We modelled the SRT primary reflector M1 with the commercial software GRASP (https://www.ticra.com). In particular, we coupled the CST simulated far-fields generated by the 24 active Vivaldi antenna elements (at 4, 6 and 8 GHz) to the SRT optics using the GRASP PO/PTD solvers (the output far-field files from CST were imported into GRASP). We used a simplified GRASP model for SRT: we assumed an ideal primary reflector with parabolic profile that has no quadrupod and includes no blockage due to the secondary mirror M2. The GRASP simulation for the three frequencies runs in approximately 12 hours. Then, the GRASP output files were imported into a Matlab (http://www.mathworks.com) script, developed to generate the final *uv* far-field plots of all the following figures.

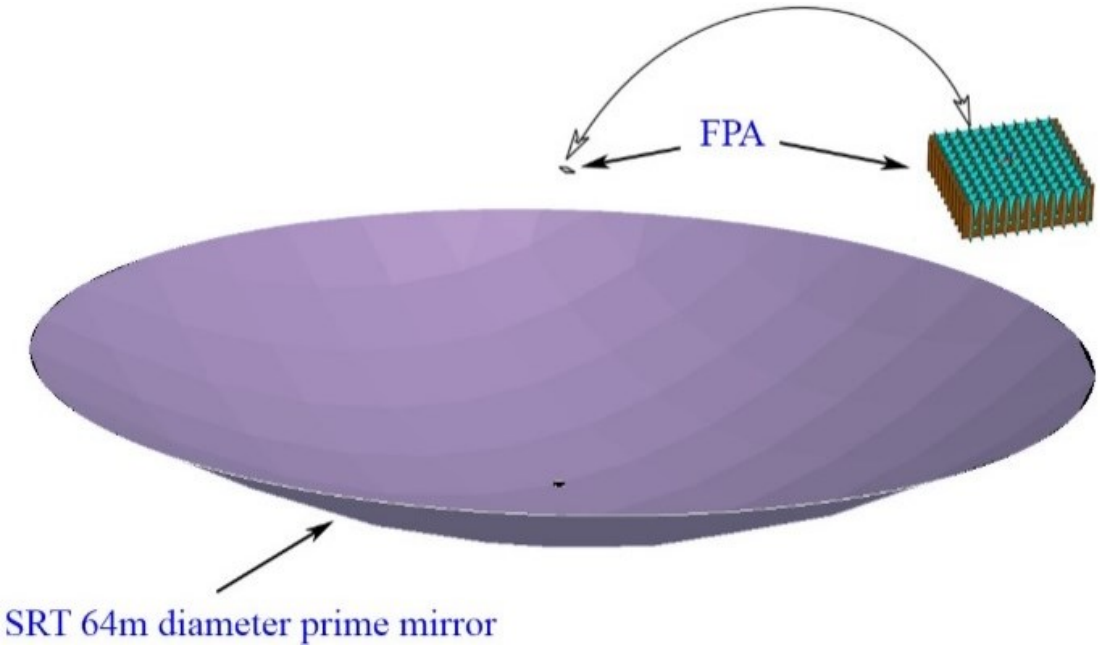

Figure 44 - Illustration of the CST-GRASP co-simulation adopted for modelling the PHAROS Focal Plane Array at the primary focus of SRT.

We note that the M1 edge is seen from the primary focus under a 74 deg half-angle. Thus, a suitable illumination pattern of M1 from primary is required to cover an angle of order 150 deg. For example, a typically used dish illumination is a Gaussian taper, which maximizes the aperture efficiency at $A_{eff}\approx 0.8$ with about 11 dB level edge taper [27]. The maximum is obtained as a trade-off between the illumination efficiency and the spillover efficiency.

5.1.5 Far-field of a single Vivaldi element of the array coupled to SRT

Each FPA Vivaldi element generates a specific far-field beam pattern on the sky when coupled to the SRT reflector. Figure 45 shows the *uv* plots of the co-polar and cross-polar far-field patterns obtained by illuminating the SRT with a single Vivaldi element of the array (Ant. #175) at 4, 6 and 8 GHz. Related performance parameters of this CST-GRASP co-simulation are listed in Table 14, third column. The antenna gain is in the range 66.9-71.34 dBi, while the antenna efficiency varies from 47% (at 8 GHz) to 65% (at 4 GHz). We note that the simulated HPBW match well with the values we estimate with the simplified formula HPBW$\approx 1.22\,\lambda/D$ (4.91 arcmin at 4 GHz, 3.27 arcmin at 6 GHz, and 2.45 arcmin at 8 GHz). The cross-polarization plots, shown on the right panel of Figure 45, have maxima at 45-degree azimuthal angle. The cross-pol values are in the range -11.59 dB to -17.59 dB below the maximum of the co-polar gain.

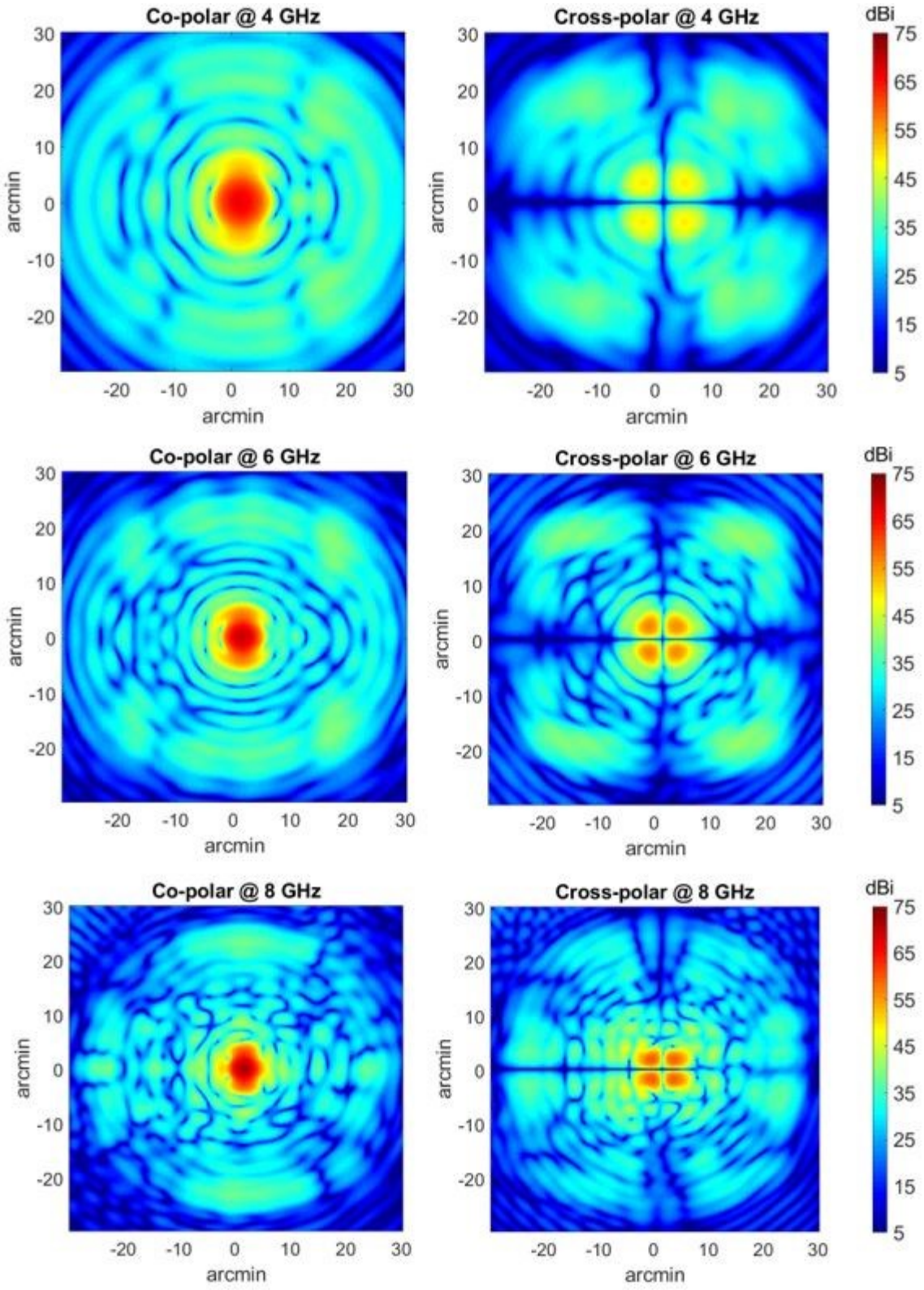

Figure 45 - Vivaldi element # 175 at SRT primary focus: co-polar (left) and cross-polar (right) beams on the sky at 4 GHz (top), 6 GHz (center) and 8 GHz (bottom).

Table 14 – Simulated parameters of the SRT antenna illuminated by: a single Vivaldi element (Ant. #175); 13 equally fed elements; 24 equally fed elements; 24 elements with CFM-derived weights.

	FREQ. [GHZ]	ANT. #175	13 ANTS. EQUALLY FED	24 ANTS. EQUALLY FED	CFM WEIGHTS
SRT GAIN [DBI]	4	66.69	70.12	65.89	72.31
	6	69.78	64.77	63.07	72.62
	8	71.34	64.02	61.77	72.36
SRT EFFICIENCY A_{EFF} [%]	4	65	143	54	237
	6	57	19	12	113
	8	47	9	5	60
HPBW [ARCMIN]	4	4.82	6.23	13.5	5.0
	6	3.27	N.A.*	N.A.*	3.2
	8	2.66	N.A.*	N.A.*	3.1
CROSS-POL [DB]	4	-17.59	-24.04	-23.97	-19.32
	6	-12.94	-15.06	-12.95	-14.81
	8	-11.59	-11.53	-12.88	-14.18

*Not Applicable because the beam has multiple maxima.

5.1.6 Far-field of 13 Vivaldi elements coupled to SRT

The far-fields of each of the 24 active Vivaldi antenna elements were propagated through the reflector. We formed four SRT far-field beams, each resulting from a linear combination of the antenna patterns generated by the sub-set of 13 Vivaldi elements illustrated in Figure 46. The 2D plots of the co-polar and cross-polar far-field patterns of Beam #1, obtained by a power-normalized equal-weight combination of the responses from the 13 Vivaldi antennas, are shown in Figure 41. The derived antenna parameters are summarized in Table 14, fourth column. At 4 GHz the reflector is under-illuminated, but the overall pattern and efficiency are sufficiently good. Instead, at 6 GHz and 8 GHz the antenna efficiencies drop to very low level as a result of a strong under illumination of the reflector, due to the narrow beams produced by the combination of 13 equally-weighted antennas. This behaviour had to be expected by the results of Fig. 9, showing field levels at 74 deg (edge taper), respectively ≈20 dB, ≈32 dB and ≈38 dB below on-axis values. While at 4 GHz the HPBW=6.23 arcmin is larger than expected from optimum aperture illumination and can be sufficiently well defined, it was not possible to estimate such antenna parameter at 6 GHz and 8 GHz because the beams have multiple maxima.

We note that the antenna efficiency at 4 GHz, calculated with GRASP, is greater than 1 (143%). This apparent element-gain paradox of phased array antennas was discussed in [27]. We can explain this result by considering the transmission mode and assuming that, when computing efficiency comparison for a PAF and a single feed, the same unitary power should be provided at their inputs. We can realize that the value of the array efficiency is normalized to the power that would be given to a single antenna element: as we employ 13 antennas, with the same power fed to a single element divided by 13, it is possible to achieve efficiencies greater than 100%. If we renormalize the array pattern we would obtain antenna efficiencies less than 100%, but we would also have less power compared to the one fed into a single antenna element. Therefore, the comparison is made assuming that equal power is provided to the array and to the single Vivaldi element and that the reference isotropic power is 4π W.

The simulated far field patterns of Beam #2, #3 and #4, are very similar to those of Beam #1 shown in Figure 46. The difference is in the beam-spot directions. The GRASP simulated result for the angular

separation between the maxima of two equal-weight beams (for example Beam #1 and Beam #2) is ≈2.7 arcmin (frequency independent). This is close to the expected value of $\vartheta \approx d_{el}/f$=3.4 arcmin, with f=21 m (the SRT primary focal length), due to the separation between the two associated sub-arrays on the focal plane, equal to the Vivaldi element size (d_{el}=21 mm).

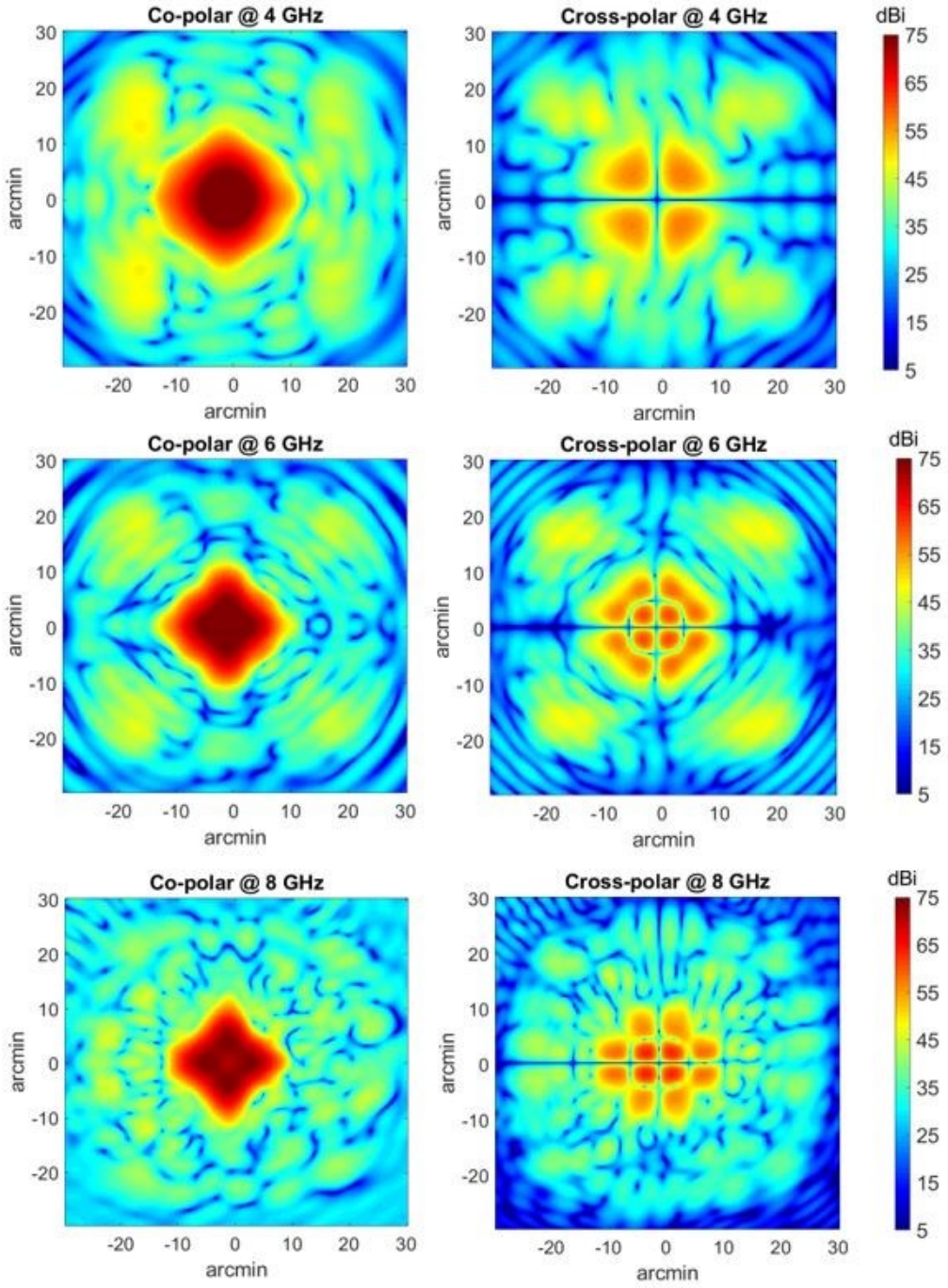

Figure 46 - Beam #1 patterns on the sky obtained by adding the far-field responses of 13 Vivaldi antenna elements feeding the SRT reflector from primary focus. Equal-weight was used to add the 13 far-fields. Co polar (left) and cross-polar (right) beams on the sky at 4 GHz (top), 6 GHz (center) and 8 GHz (bottom).

5.1.7 Conjugate Field Matching applied to PHAROS-SRT

The conjugate field matching method (CFM) is a technique to derive the optimum PAF element weights and maximize the coupling between a plane wave from a given direction and the receiver signal [27]. Since the prime mirror capturing the incident plane wave has a circular aperture, the on-axis beam has, on the focal plane, the typical diffraction figure of a circular aperture known as Airy pattern [27]. Off-axis beams or aberrated (distorted) mirrors would result in focal plane field distributions different from the Airy pattern. The basis for the CFM method is the fact that the product of a phase-distorted field and its complex conjugate is a plane wave. This opens the possibility to use PAFs for dish distortion compensation and for correction of off-axis aberrations. Once a focal plane field distribution *Ei* produced by a plane wave illuminating the reflector is known, the weighting field distribution Ew producing maximum flux of energy Ew · Ei on the focal plane is its complex conjugate Ew = Ei*. Since an array can be thought as a discrete sampler of a focal plane field, the optimum coupling excitation coefficients for delivering maximum power are the complex conjugate of the field samples at each element position. Due to the reciprocity theorem the focal plane field in receiving mode can be estimated from the far-field in transmitting mode: the Airy pattern samples (or focal plane phase distorted field samples) can be obtained by considering each array element in transmission, illuminating the reflector system, and calculating the field at a given far-field distance in the same direction as the incoming plane wave under consideration. The samples obtained in this way are complex numbers for which it is important to preserve their relative distribution.

We derived the CFM optimum beam weights of the 24 PHAROS active antenna elements for SRT boresight illumination using Matlab. The conjugate of the simulated boresight far-field values gave the CFM complex weights, which we evaluated at 4, 6 and 8 GHz. The modulus of the derived weights are plotted in Figure 47. Then, we used the 24 derived CFM weights to generate the *uv* SRT co-polar (Figure 48, right panels) and cross-polar (Figure 49, right panel) beam patterns. For comparison, the left panels of Figure 48 and Figure 49, show the co-polar and cross-polar beam patterns that would be obtained by equal-weight illumination of the 24 Vivaldi antenna elements. The summary of the results, provided in Table 14, shows how the CFM weights achieve high antenna performance, with antenna gain greater than 72 dBi, and efficiency as high as 60% at 8 GHz. Efficiencies of 237% and 113% are obtained at 4 GHz and 6 GHz, respectively.

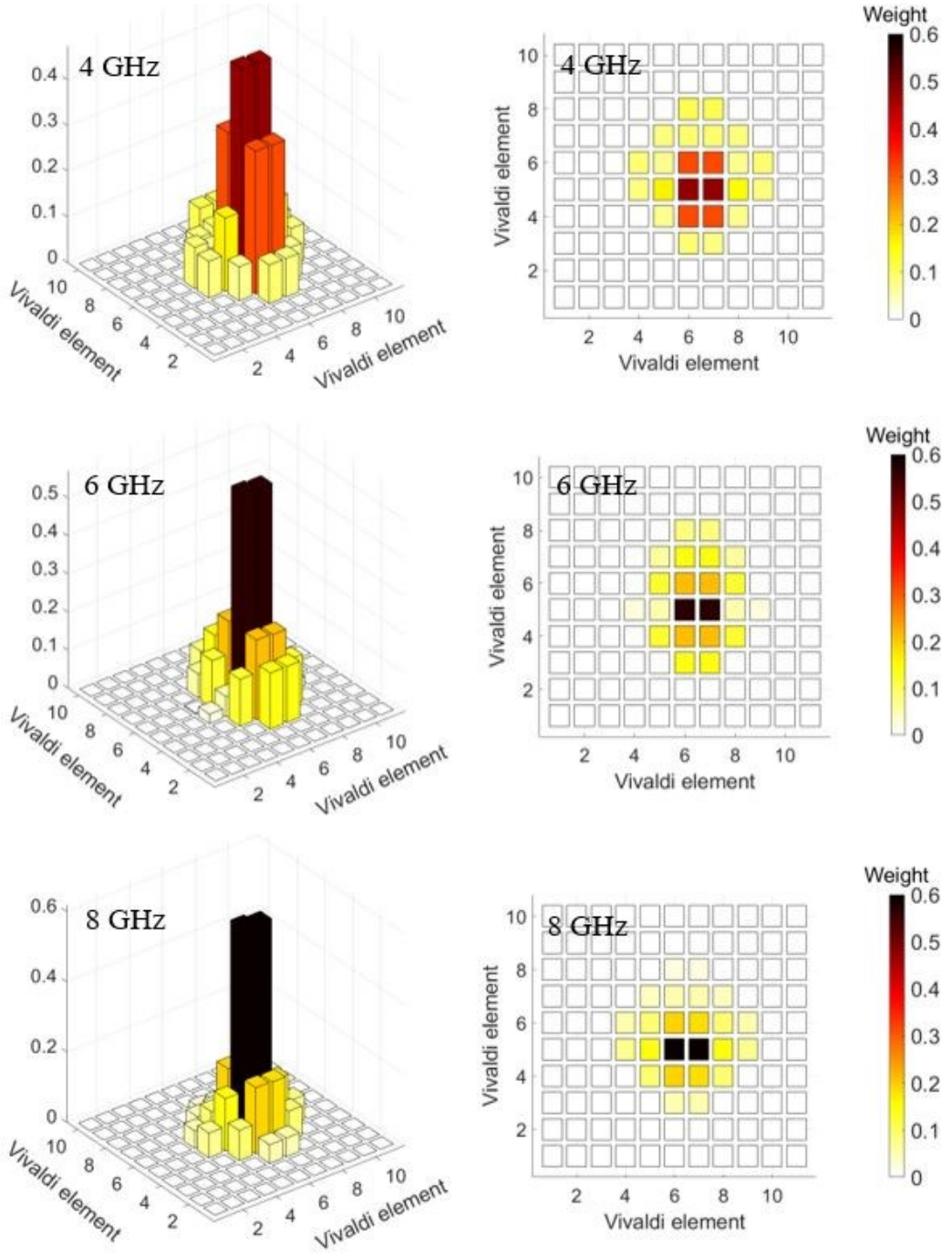

Figure 47 - Weights of the 24 antennas calculated by CFM at 4 GHz (top), 6 GHz (centre) and 8 GHz (bottom).

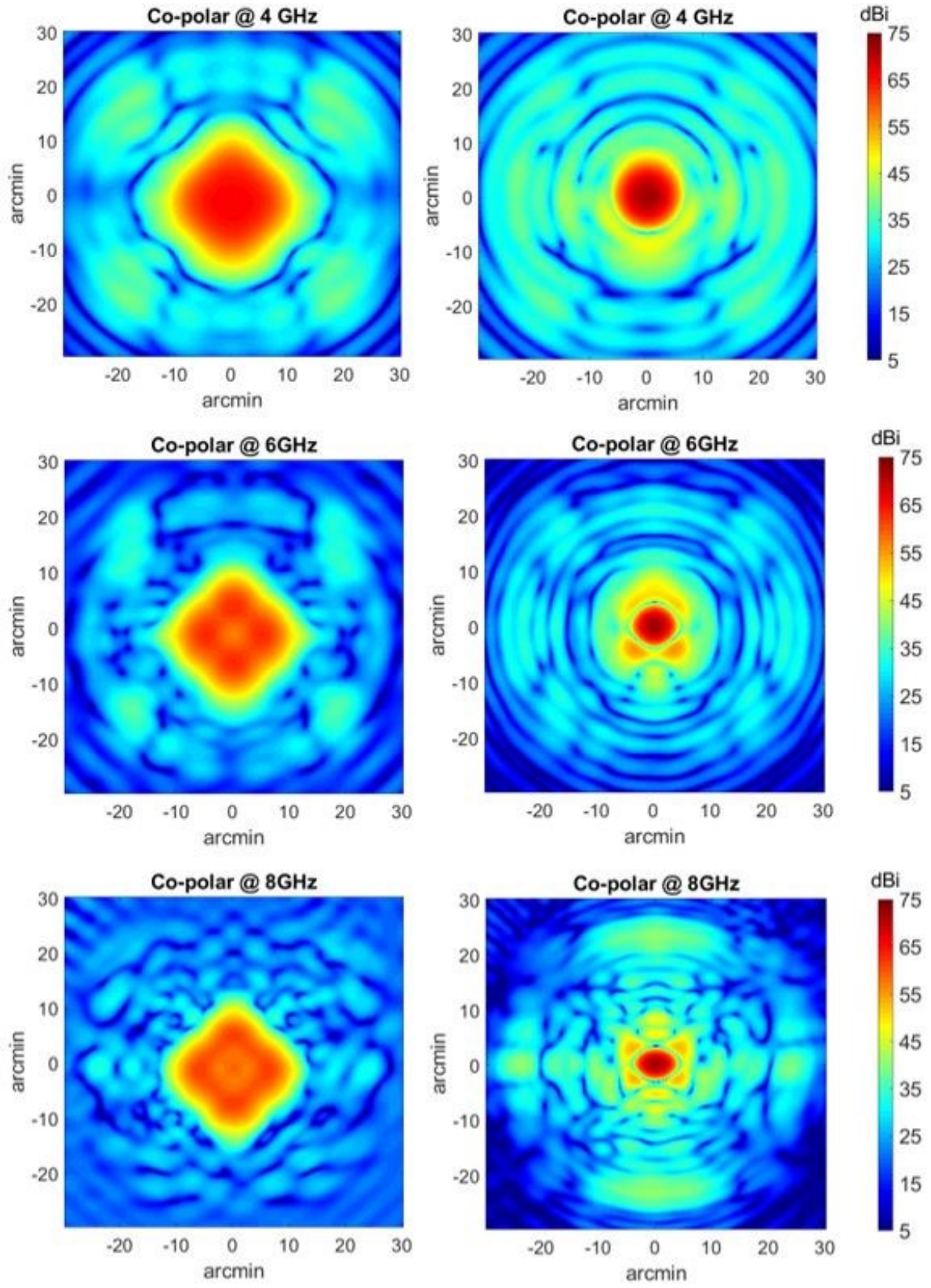

Figure 48 - Co-polar beam patterns of SRT by feeding 24 Vivaldi antennas with equal-weight (left panels) and with CFM weigths (right panels) at 4 GHz (top), 6 GHz (center) and 8 GHz (top).

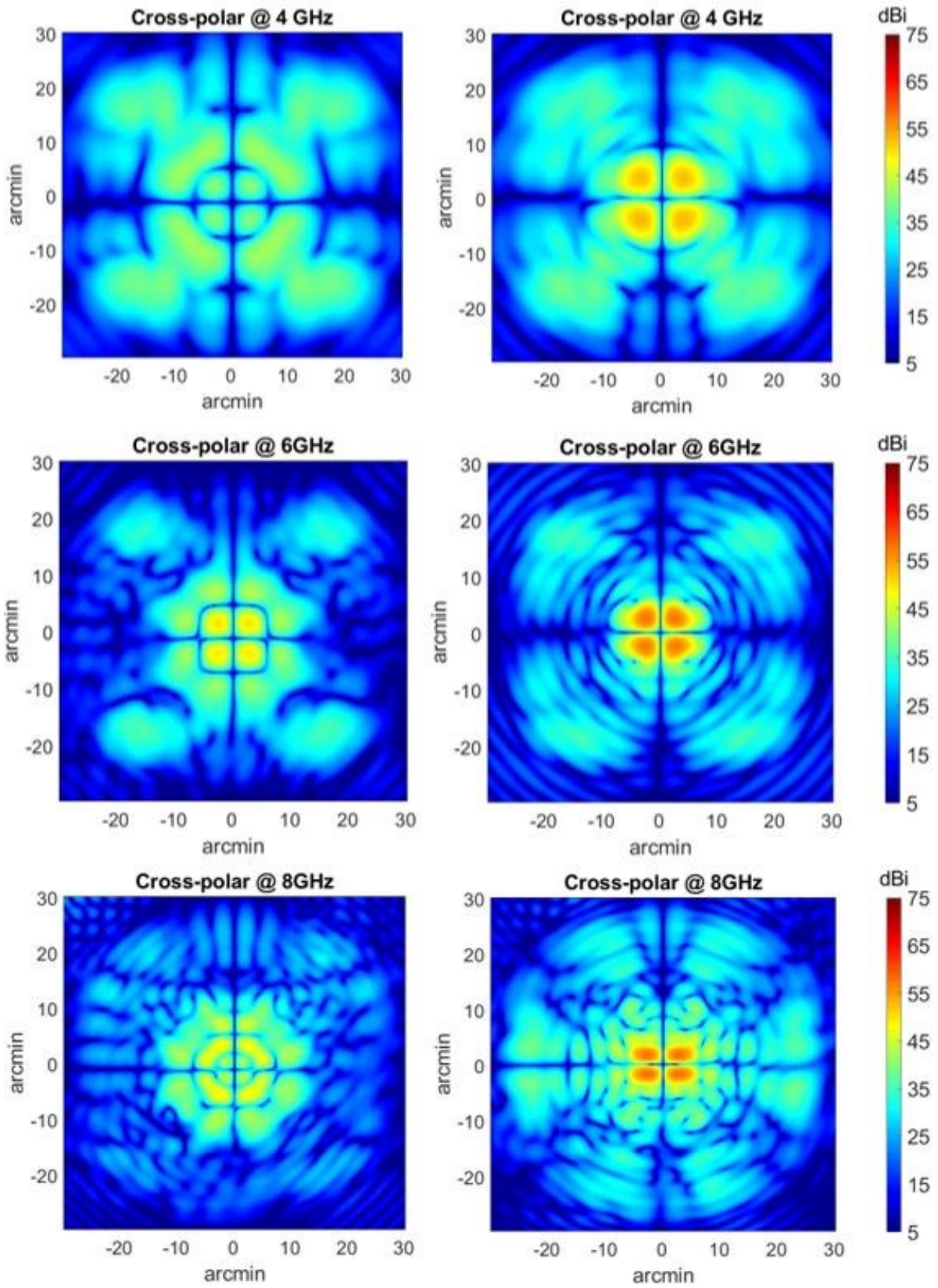

Figure 49 - Cross-polar beam patterns of SRT by feeding 24 Vivaldi antennas with equal-weight (left panels) and with CFM weights (right panels) at 4 GHz (top), 6 GHz (center) and 8 GHz (top).

5.2 Warm Section Multi-channel Receiver

The PHAROS2 warm section [26] is capable of analog processing up to 32 independent RF signals from the Vivaldi array, although only 24 are used.

A 3D view of the WS 32-channel receiver that we designed, assembled and tested, is given in Figure 50. The WS includes four eight-channel WS RF/IF modules, one LO distribution module and one WS monitor and control module arranged in a standard 6U×19-inch rack. The receiver performs signal filtering by switched filter bank, signal conditioning, and single frequency down-conversion of a section of the 2.3-8.2 GHz RF band down to the 375-650 MHz IF band (275 MHz instantaneous bandwidth). The down conversion scheme utilizes sideband separating mixers in LSB (Lower Side Band). The IF signals are converted to optical signals by analogue WDM (Wavelength Division Multiplexing) "IFoF" (IF over fiber) fiber-optic transmitter (OTX) that transports two IFs over a single optical fiber. One of the four BPF filters, BPF-A, is specified to cover the broad 2.3-8.2 GHz RF frequency band, while the other three filters (BPF-B, -C and -D) have ≈275 MHz "narrowband" characteristics, with bands centered around astronomical lines.

We note that the frequency range of the WS receiver (2.3-8.2 GHz) is larger than the one delivered by the cryogenic section (4-8 GHz). Therefore, the room-temperature Front-End (and associated digital backend) can be used not only for application with the PHAROS2 cryogenic array, but also with other PAF antenna array that could be developed to cover the band 2.3-8.2 GHz (fmax/fmin=3.4) or part of it.

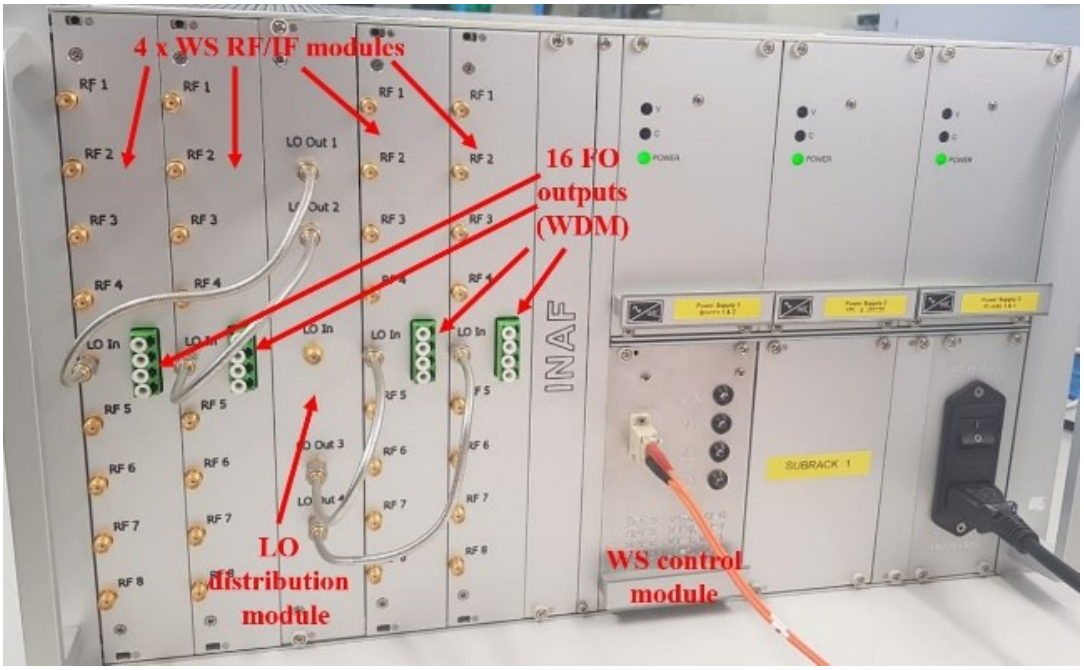

Figure 50 - Fully assembled PHAROS2 warm section 32-channel receiver showing the four WS RF/IF modules assembled with LO distribution module and WS control module arranged in a standard 19-inch × 6U rack.

5.2.1 Eight-channel Warm Section RF/IF module

Each of the four WS RF/IF modules (Figure 51) includes a PCB circuit and four WDM fiber-optic transmitters ("OTXs") on opposite sides of a mechanical support. The RF/IF module has eight SMA RF input connectors, one SMA LO input connector (centered on the front panel) and one quad LC/APC output connector to extract the four WDM IFoF optical fiber outputs provided by the four OTXs. The module employs a single four-layer PCB based on Rogers RG4003C substrate with thickness 0.508 mm and commercial surface-mounted components. The PCB adopts the standard double-height Eurocard size (6U, equivalent to ≈233.35 mm) that can be plugged into a standard chassis, which in turn can be mounted in a 19-inch rack. The IF output signals are extracted from MCX connectors mounted orthogonal to the board. The board IFs outputs are connected to the WDM fiber-optics transmitter inputs through coaxial cables (Figure 51, bottom panel).

The first element of the signal chain is a four-way switch filter-bank that allows selection of one of the four RF band pass filters through two SP4T switches. The filter bank is cascaded with an RF amplification stage followed by a sideband separating (2SB) mixer operated in single down conversion LSB mode. The 2SB mixer consists of a commercial I/Q mixer cascaded with a 90° IF hybrid that delivers two IF output signals to two independent ports. The USB output of the IF hybrid is terminated into a 50 Ω load, while its LSB output is band pass filtered and amplified. The IFs signal are routed to the on-board MCX connectors.

The PCB has one SMA connector for the LO input signal, centrally located on the RF side of the board. The LO signal is amplified, band pass filtered (by a cascade of low pass and high pass filters) and distributed internally to the PCB with one eight-way splitter based on a cascade of Wilkinson power dividers.

The PCBs and the mechanical housings were fabricated, respectively by Italian companies and INAF.

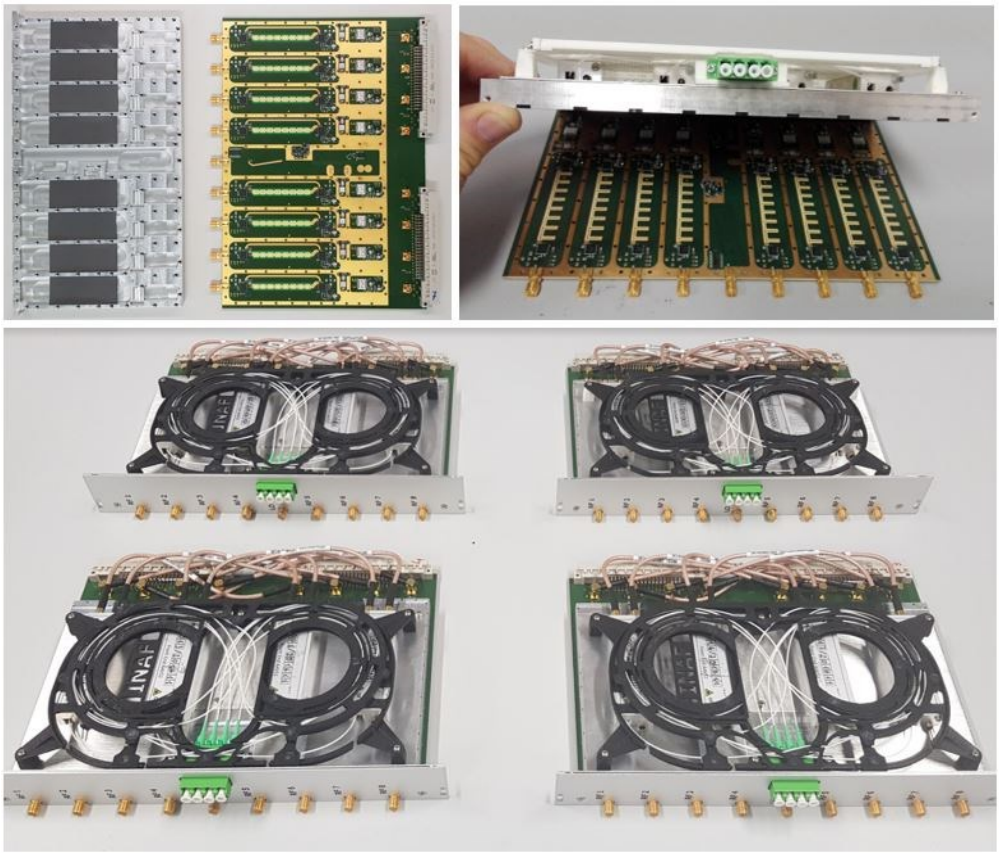

Figure 51 - Photos of the WS RF/IF module. Top left: mechanical housing (left) and fabricated PCB (right) before assembly. Microwave sbsorbers are glued in the pockets of the PCB mechanical housing. Top right: PCB board (first prototype version) and mechanical housing during assembly with optical transmitters. Bottom: Four WS RF/IF modules fully assembled, with OTXs.

5.2.2 Warm section Local Oscillator distribution module

The four WS RF/IF modules receive a copy of the same LO signal from the LO distribution module (Figure 50 and Figure 52) so that the mixers (eight per board) are pumped under identical conditions. The 2.950-8.575 GHz four-way LO splitter utilizes Wilkinson power dividers and incorporates a directional coupler (coupling value ≈ -20 dB) that directs part of the signal to a detector. The detector allows converting the LO power to a decibel-scaled DC output used for monitoring purpose.

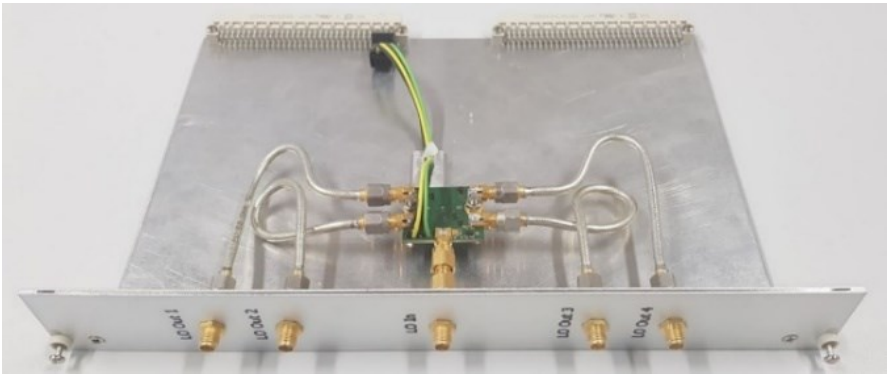

Figure 52 - Photos of the LO distribution module showing the four-way PCB LO splitter connected to the front panel SMAs through coaxial cables.

5.2.3 Warm Section monitor and control module

The WS monitor and control module (Figure 53) is based on commercial optical fiber to Ethernet mediaconverter (Digitus DN-82010) and microcontroller (Arduino Leonardo ETH) incorporated into a 3U rack-mountable box biased with +5 V. The module utilizes transmitting/receiving mode with TX/RX multimode fiber and has two TTL outputs. It allows selection of one among four possible band pass filters of the WS RF/IF modules and returns voltage values inversely proportional to the LO power of the LO distribution module. Furthermore, the module reads the physical temperature provided by the four sensors placed on the PCBs (one per board). The front-panel includes LEDs to visulaize the selected filter, the presence of LO power and of bias voltage.

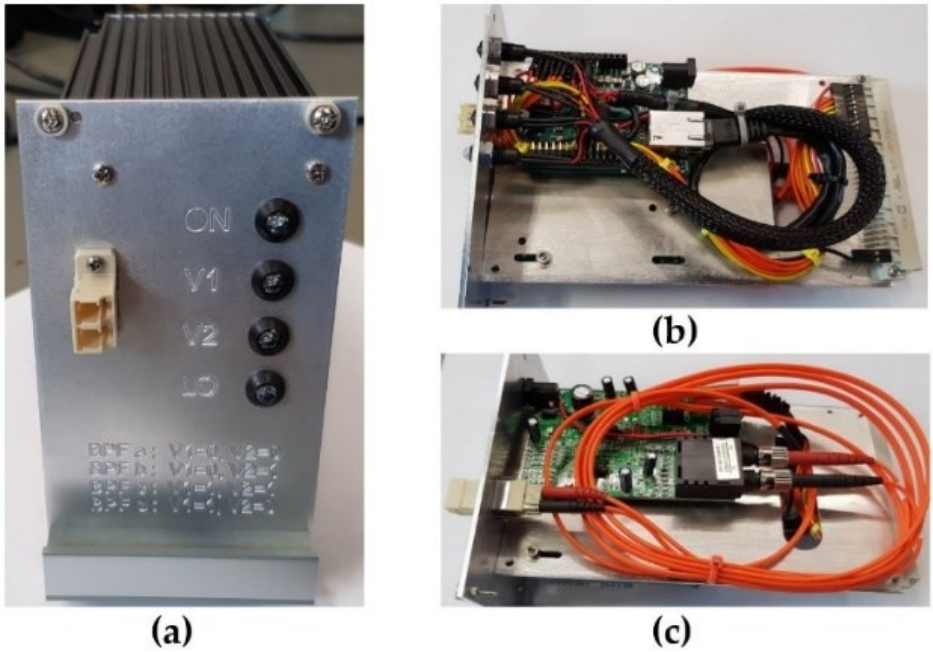

Figure 53 - Warm Section control module and its parts. (a) Front panel with TX/RX multimode fiber connector pair and LEDs. (b) Microcontroller by Arduino Leonardo ETH. (c) Optical fiber to Ethernet media-converter (Digitus DN-82010).

5.2.4 IF over fiber analogue links

The IFoF fiber-optic links were developed for SKA LFAA (Low Frequency Aperture Array, https://www.skatelescope.org/lfaa/) by an INAF-led collaboration with industrial partners and adopted for PHAROS2. The WDM IF over fiber technology utilizes dual distributed feedback (DFB) laser sources on the OTXs and dual photodiode detectors on the ORXs providing IF isolation between channels greater than 45 dB up to the maximum IF frequency (650 MHz). The signals are de-multiplexed at the optical receiver side. The optical (infrared) wavelengths at λ = 1270 nm and λ = 1330 nm were chosen to minimize the signal dispersion of the G652D optical fibers across the IF band. The OTX optical lasers are class 3A, delivering an optical power at each of the two WDM wavelengths of less than 5 mW.

The ORXs are part of the iTPM digital backend (see section IV for further details). Each of the optical receivers utilizes two independent IF receiver chains that adapt the signals for digital conversion by the following iTPM Analog Digital Unit (ADU). Each of the ORX chains performs amplification and level adjustment through the digital step attenuators (DSAs) with 31 dB range and 1 dB step. The ORX control adopts the SPI bus from the ADU board. The maximum gain of the IFoF link is ≈60 dB when the DSA is set to its minimum attenuation of 0 dB (the link gain is of order ≈35 dB when setting the DSA to 25 dB).

5.2.5 Characterization of the warm receiver section

Two identical 32-channel receivers were fully assembled, although only one was required to equip the PHAROS2 PAF. The eight-channel WS RF/IF modules were characterized by INAF (Figure 54). The modules perform according to technical specifications and have similar performances. Figure 55 shows an example of the measured receiver gains for the eight channels when the LO is set at a fixed frequency of 5 GHz and the RF is swept from 4 to 6 GHz (filter BPF-A selected). Vertical lines (in red) limit the nominal LSB (4350-

4625 MHz) and USB (5375-5650 MHz) down-converted to the 375-650 MHz IF band. The receiver signal gain is in the range GLSB=15-18 dB across the LSB (signal band) and below GUSB=-6 dB across the USB (image band). The image sideband rejection, i.e. the ratio between the conversion power gains IR=GLSB/GUSB at the available IF port, is greater than 23 dBc across the nominal band.

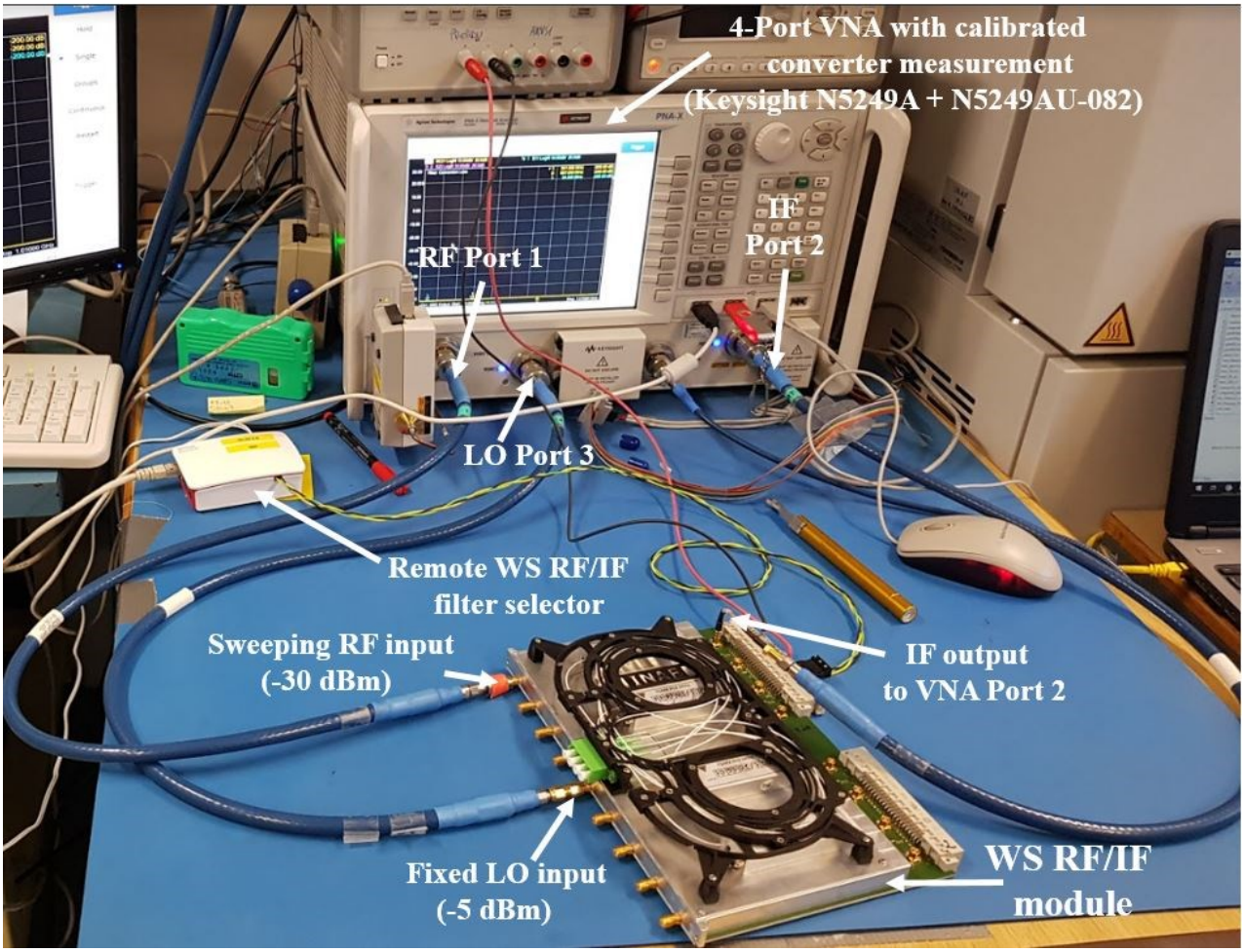

Figure 54 - Testing of one of the WS RF/IF boards (without the IFoF links). The RF port of the VNA is connected to ch. 1 of the board. The IF signal is extracted from the corresponding MCX connector.

We repeated the tests at 12 different LO frequencies, from 3 GHz to 8.5 GHz by 0.5 GHz steps, and measured the LSB gains of the eight-channels of the eight RF/IF boards (Figure 56). Across 2.3-8.2 GHz the LSB gains are in the range GLSB=6-23 dB; these are greater towards the lower part of the RF band (around 2.5 GHz) and fall off at the highest frequencies (beyond ≈8.2 GHz). The measured LSB gains across the three narrow band filters (BPF-B, C and D) are shown in Figure 57. All channels have very similar responses, with gains ≈10 dB.

Figure 58 shows the measured results of the image sideband rejection versus LSB frequency across the ≈2-9 GHz band for the four band pass filters. The image sideband rejection with BPF-A (red curves) has minima IR≈20 dBc at the center of the IF band (≈510 MHz) and reaches values greater than ≈40 dBc towards the IF band edges (at 375 MHz and 650 MHz). Selecting the narrow band filters BPF-B, BPF-C and BPF-D allows operating the receiver with much improved rejection, of order ≈60 dBc, as a result of the combined effect of the mixer sideband separation and of the filter rejection.

We measured the noise figure (NF) of the WS RF/IF chains using the FSV Signal Analyser from Rohde and Schwarz coupled with a noise source (Noisecom NC3104, ENR≈15.6 dB at 5 GHz). The test results are shown in Figure 59. The measurements refer to the board input SMA connector and include the signal chains up to the IF MCX connector. NF is in the range 8-16 dB across 4-8 GHz. For a given LO setting NF is minimum at the center of the IF band and increases towards the band edges. We note that NF value is lower for the wideband filter BPF-A than for the three narrow band filters BPF-B, C and D. This was expected from simulation as the insertion loss in front of the first amplifier on the WS board, which impacts the noise, is greater for the narrow-band filters.

Starting from the measured WS noise values, we evaluated the impact of the noise added to the entire PHAROS2 receiver chain. In particular, we estimated the noise temperature that would be obtained at the input of a cryogenically cooled PHAROS2 LNA (Low Noise Factory LNF-LNC4_8C) by cascading it to the WS (through coaxial cables assumed to have insertion loss of order ≈2 dB). The average noise temperature and gain performance of the cryogenic LNAs are TN≈2.3 K and G≈39 dB, respectively. The predicted noise temperature of the receiver chain at the cryogenic LNA input, assuming there are no mutual effects and noise coupling between the antenna elements, is shown in Fig. 15. Across the nominal RF range of PHAROS2, 4-8 GHz, the receiver noise temperature falls in the range 2.5-3.5 K for operation around the center of the IF band (at 512.5 MHz). A slight increase of noise, up to values of 5 K, is predicted for operation at the edges of the IF band. Although the cryogenic LNA operates across 4-8 GHz, in order to generate the plot of Figure 60, we assumed the amplifier could perform with same in-band noise and gain (G≈39 dB) across the entire LSB frequency range ≈2-8.5 GHz.

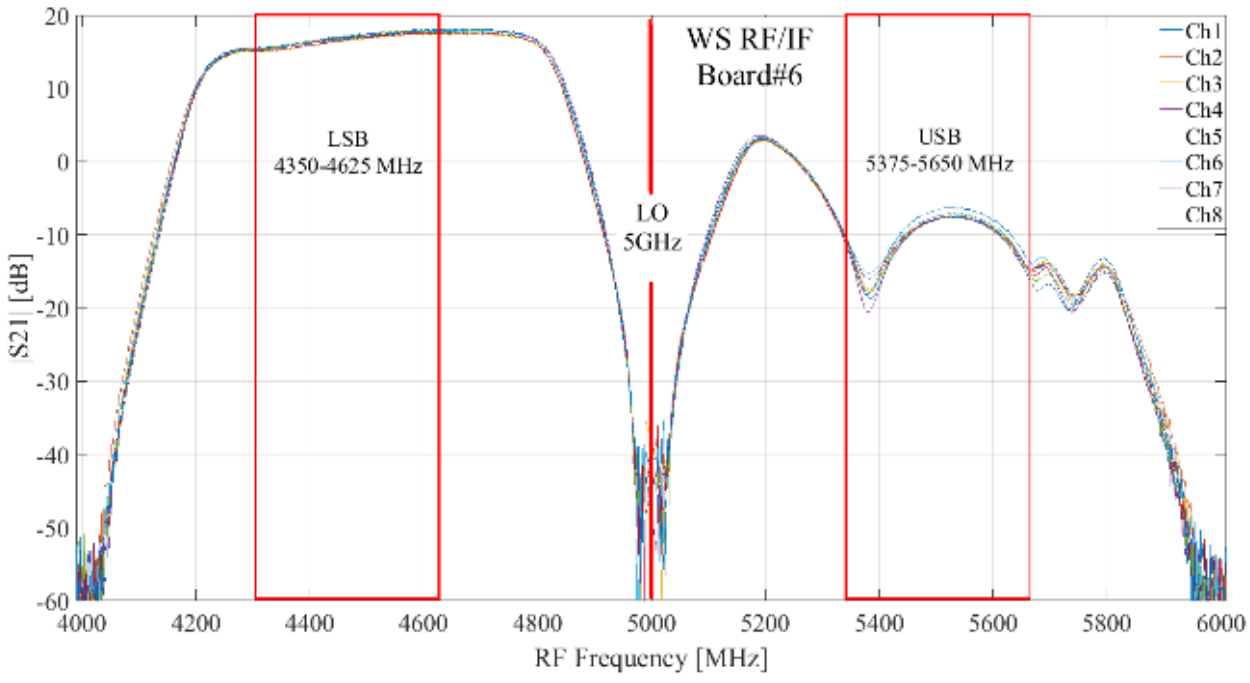

Figure 55 - VNA measured transmissions of the eight channels of one of the WS RF/IF boards by selecting filter BPF-A and LO frequency 5 GHz.

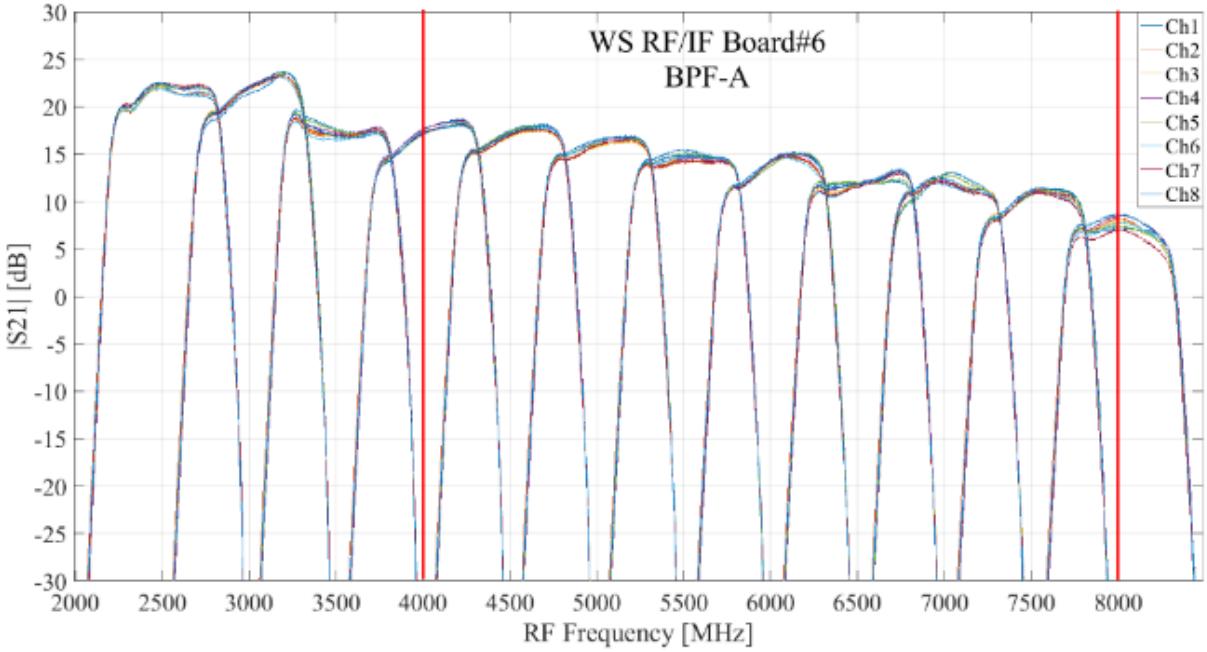

Figure 56 - Lower side band (LSB) gains of the eight channels of WS RF/IF Board #6 measured from the SMA RF input connector to MCX IF output connector with filter BPF-A. Cumulated measurements from 12 different LO frequency settings, ranging from 3 GHz to 8.5 GHz by 0.5 GHz steps. The power level was set at −5 dBm for the LO and −30 dBm for the RF.

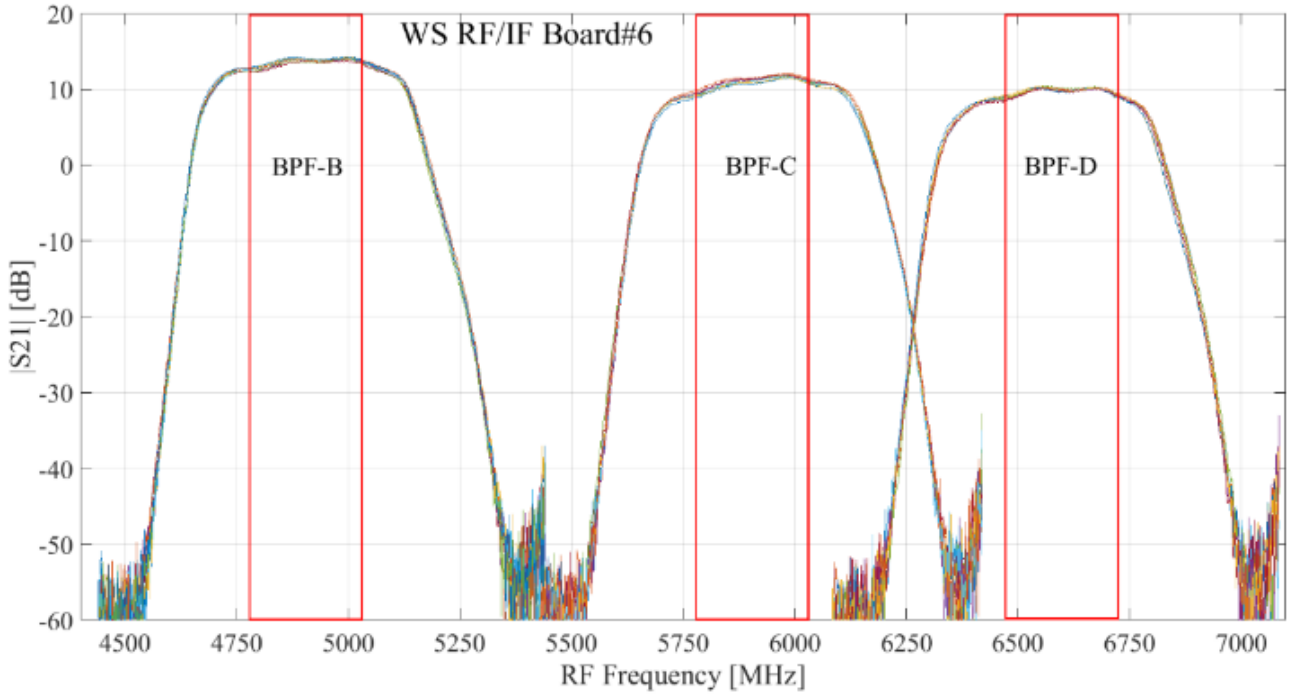

Figure 57 - Measured LSB gains of the eight channels of WS RF/IF Board #6 measured from the SMA RF input connector to MCX IF output connector for filters BPF-B, C and D.

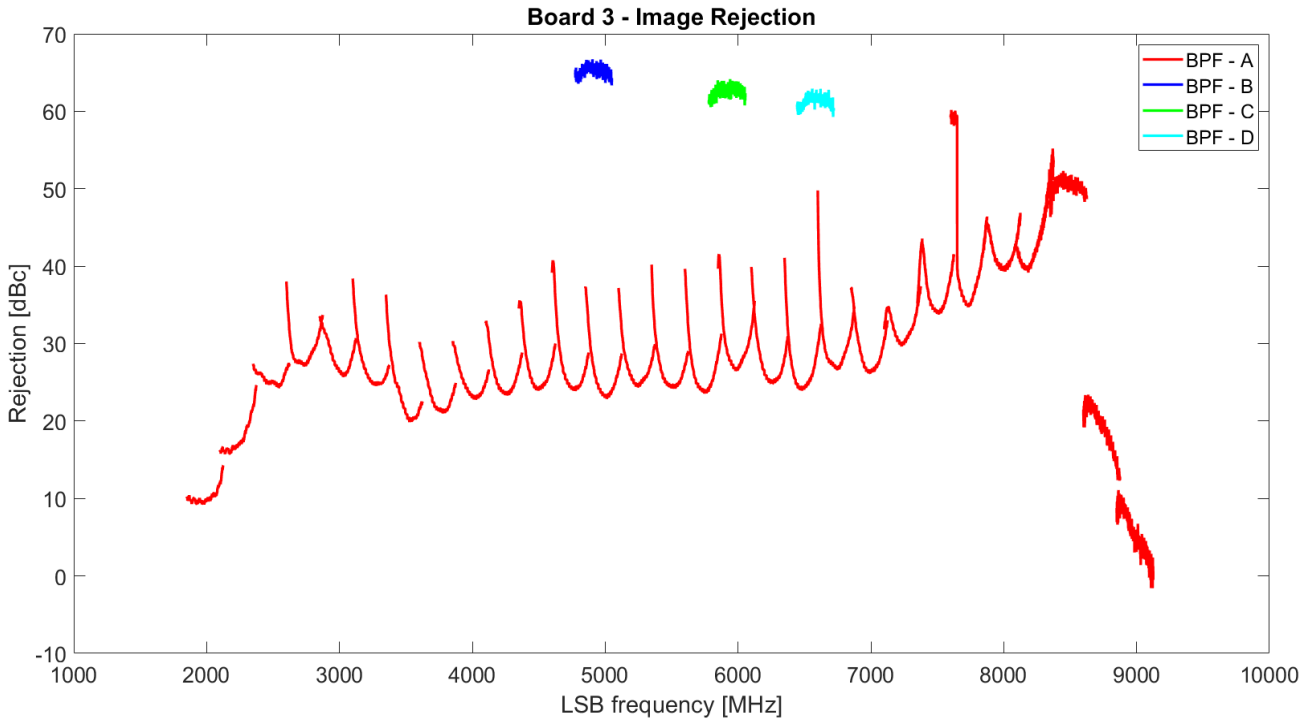

Figure 58 - Image sideband rejection measured for one of the channels (ch.1) of WS RF/IF Board #3 across the four different band pass filters. The 2-9 GHz LSB signal frequency for BPF-A was covered by 29 different LO frequency settings (red curves). Measured image rejection across BPF-B, C and D are shown by curves in dark blue, green and light blue, respectively. For each given LO frequency, the rejection values refer to the 375-650 MHz IF frequency band (275 MHz bandwidth).

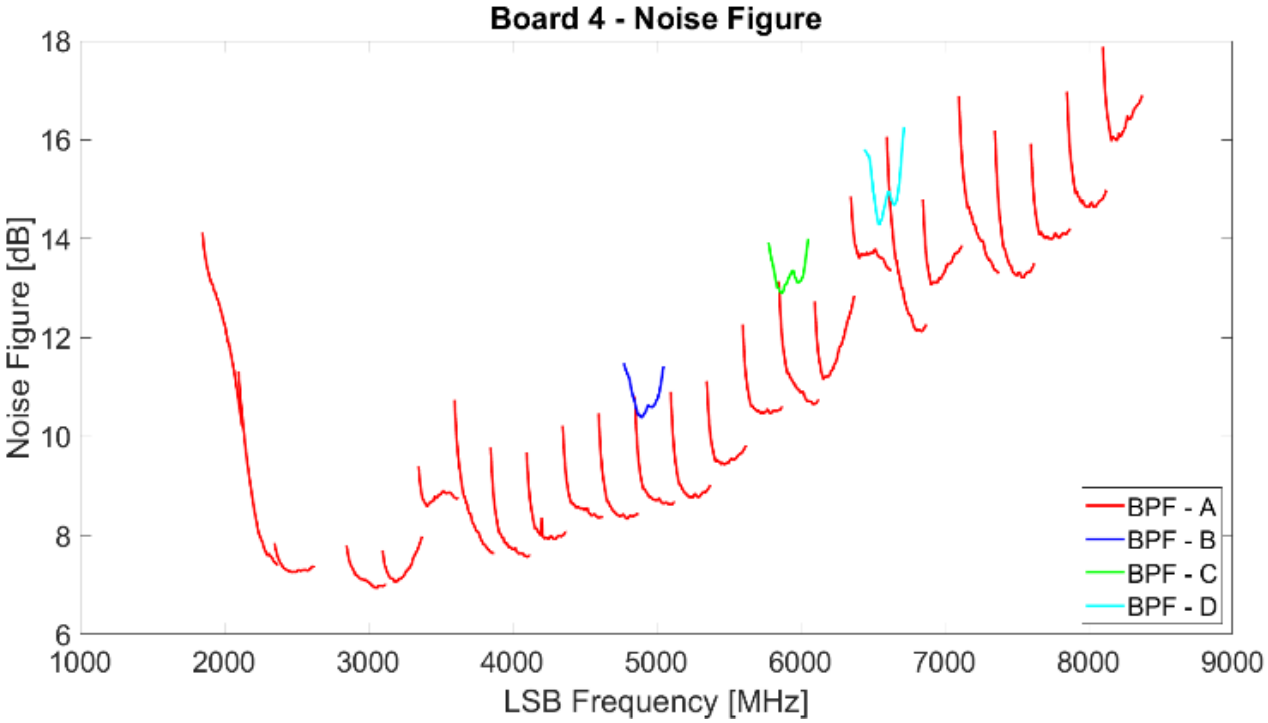

Figure 59 - Measured noise figure of one of the channels (ch. 1) of WS RF/IF Board #4 across the four different band pass filters. The bandwidth are 275 MHz wide for each of the different LO settings.

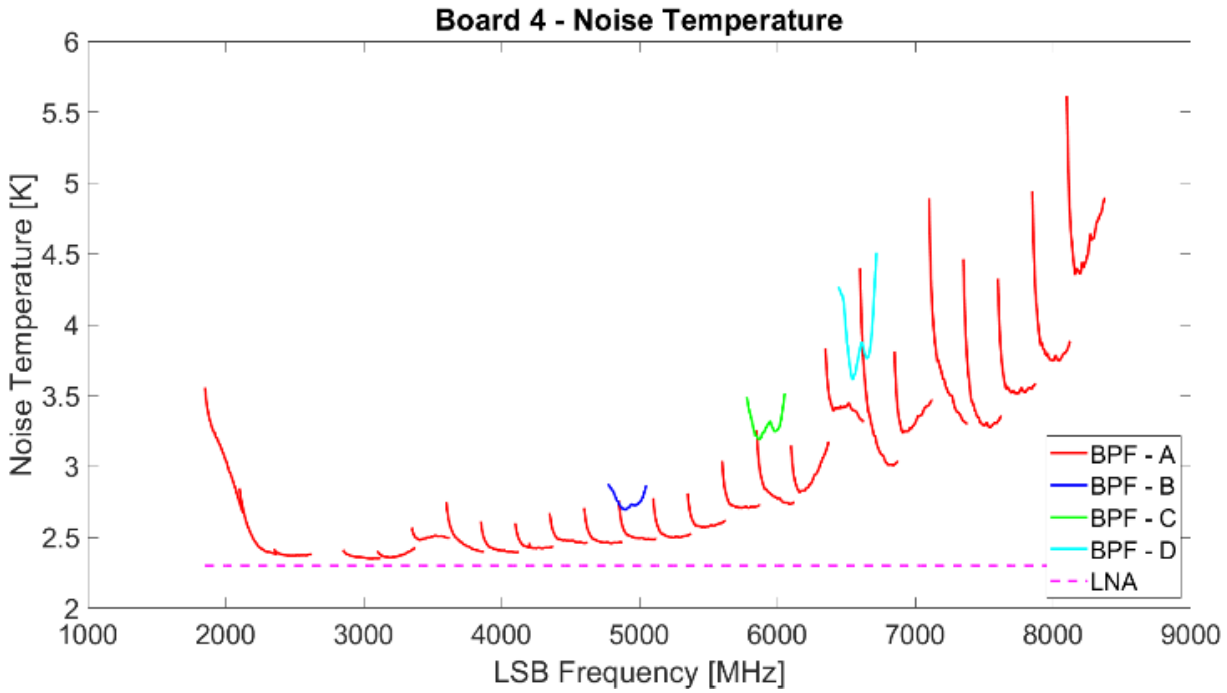

Figure 60 - Predicted noise temperature at the input of a PHAROS2 cryogenic LNA (TN□2.3 K, pink dashed line) cascaded to the warm receiver section.

We tested the WS receiver with IFoF link. The average gain across 4-8 GHz is GLSB≈50 dB when the digital step attenuator of the ORX is set to DSA=25 dB. The gain can be varied from ≈45 dB to ≈75 dB by changing the DSA from 31 dB to its 0 dB minimum attenuation. The measurement results are shown in Figure 61.

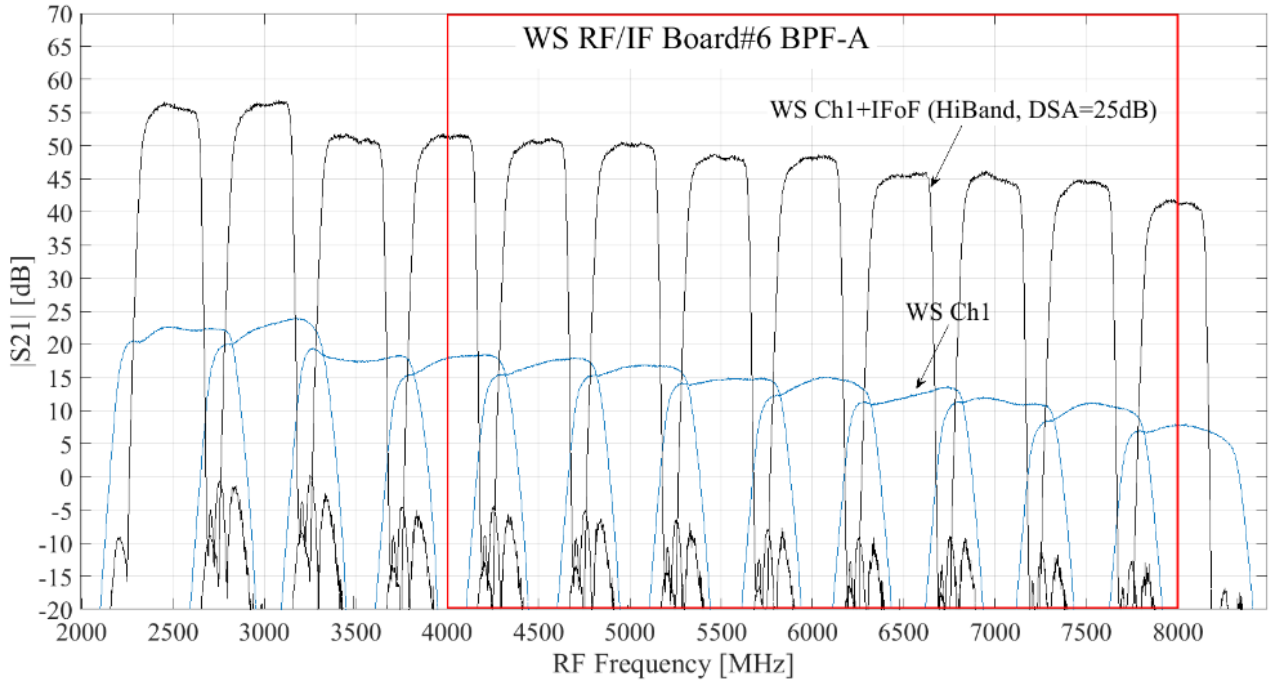

Figure 61 - Measured gain of Board #6 for 12 different LO frequency settings, from 3 GHz to 8.5 GHz by 0.5 GHz steps: including IFoF link with DSA = 25 dB (black curves) and without IFoF link (blue curves). The vertical red lines at 4 and 8 GHz delimit the nominal band edges of PHAROS2.

5.3 iTPM digital backend for PHAROS2

The iTPM digital backend is a processing module developed for SKA LFAA [28] by an INAF-led collaboration with industrial partners. The PHAROS2 digital backend is based on the iTPM hardware, version 1.2. We modified the firmware to perform the digital beamforming synthesis of the signals from the PHAROS2 antenna elements on the iTPM Field Programmable Gate Arrays (FPGAs).

PHAROS2 can simultaneously produce up to four beams with non-integrated spectra (used for pulsars timing) and up to four beams with “integrated spectra” (used for pulsar search and on-the-fly mapping). A schematic diagram showing the implementation of the beamforming is shown in Figure 62.

The iTPM consists of the Analog Digital Unit (ADU) and of two preADU boards (Figure 63). The ADU is a 6U board containing sixteen dual-inputs Analog to Digital Converters (ADC) and two FPGAs (Xilinx Kintex Ultrascale XCU40) capable of digitizing and processing up to 32 RF input signals. Although the ADU was conceived mainly for the 50-350 MHz low frequency band, its use proved to be effective also for the 375-650 MHz high frequency band, therefore being suitable to process the IF signals from the PHAROS2 warm receiver section. The preADU board is based on eight ORXs, each of which performs optical-electrical demultiplexing conversion, amplification, level adjustment (with the digital step attenuator, DSA) and equalization. Furthermore, the ORX includes a band selector with a filter bank (low band 50-375 MHz used for LFAA, or high band 375-650MHz used for PHAROS2) and a switch to divert the IF input of any receiver on a 50 Ω load for debugging procedures.

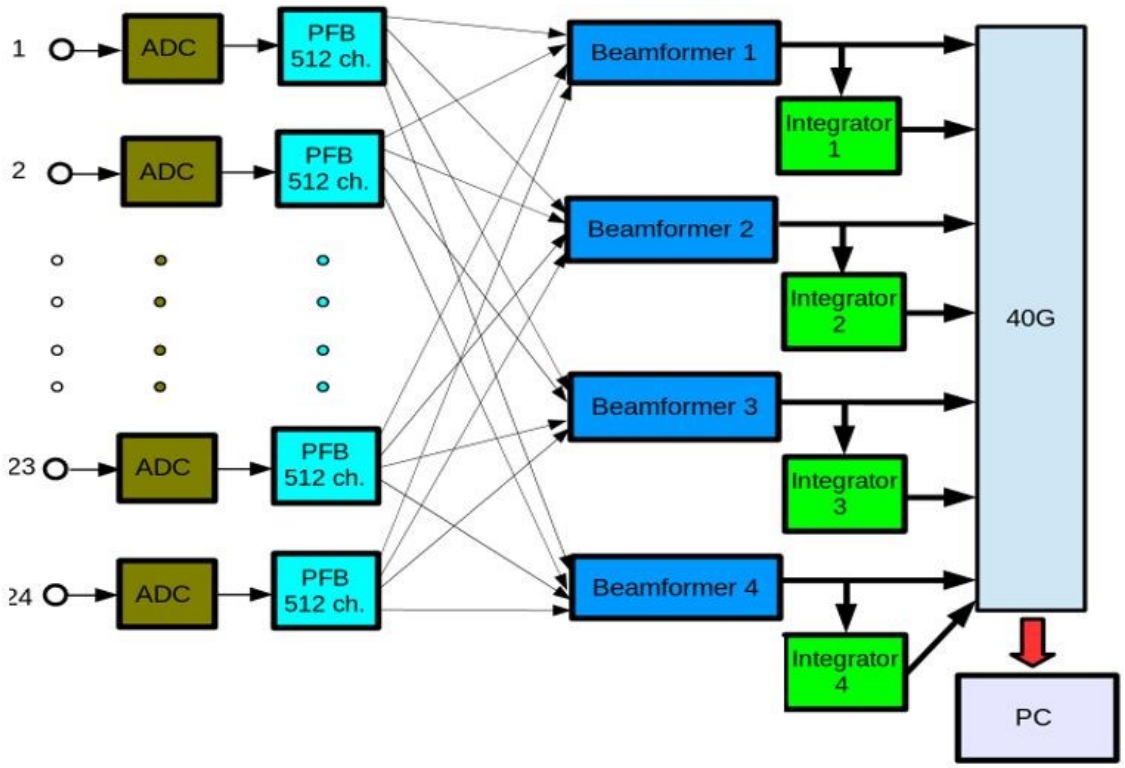

Figure 62 - Schematic diagram illustrating the implementation of the beamforming in the iTPM FPGAs for 24 single-polarization antenna elements. Four beams can be digitally synthesized, each provided with integrated spectra and with non-integrated spectra.

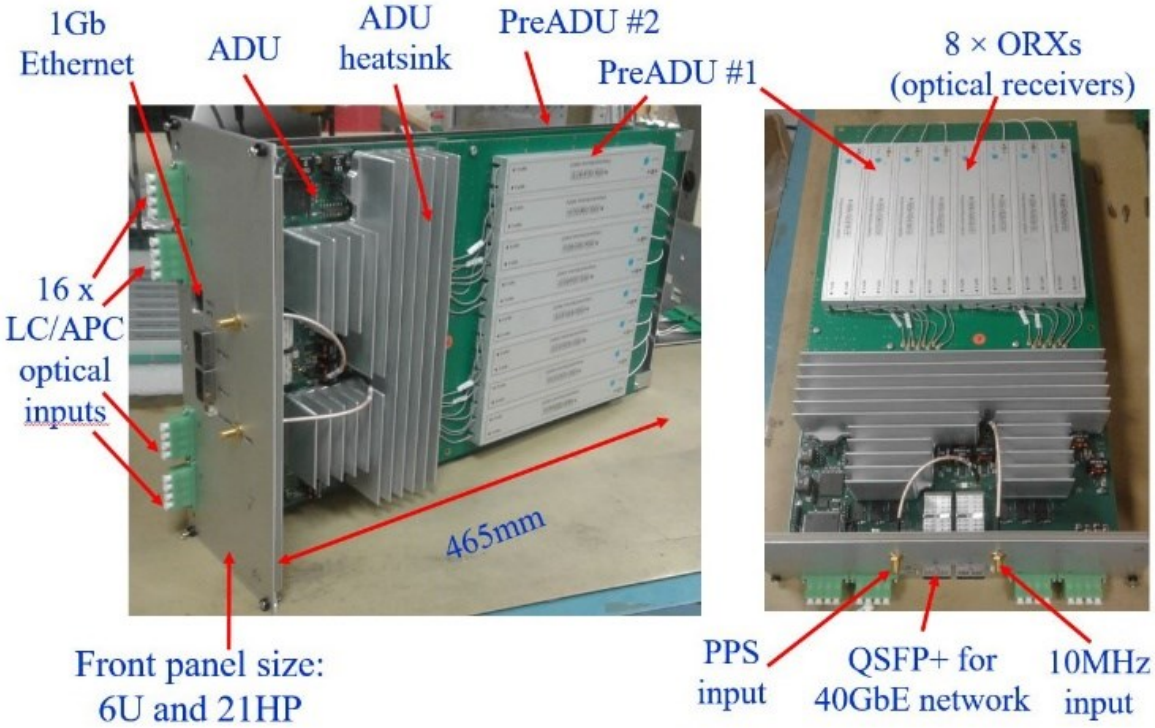

Figure 63 - iTPM digital backend consisting of the Analog Digital Unit (ADU) and of two preADU boards. Each preADU boards contains eight fiber-optics receivers (ORXs).

The ADU is capable of acquiring and processing up to ≈500 MHz bandwidth radio-frequency streams from 32 antennas. The ADU adopts 2 x 40Gbps Ethernet interfaces (QSFP), one for each FPGA, and high speed internal bus to connect the two FPGAs (25 Gbps + 25 Gbps bidirectional). Data processing includes channelization of

the sampled data for each antenna based on an oversampling polyphaser filterbank architecture (oversampling factor 32/27) with 512 spectral channels and beamforming on the FPGAs. The ADCs (AD9680, 1 GS/s) are set to a sampling rate of 700 MS/s, thus the IF 375-650 MHz band (275 MHz bandwidth) is sampled in the second Nyquist zone. The primary channels have a bandwidth of 810 kHz and are spaced of 684 kHz. The integration time for the integrated version can be set by the user to vary from ≈50 μsec to ≈1 sec. All the formed beams are sent to the 40 GbE network and further processed by other computing nodes (CPU, GPU).

Figure 64 shows the digital backend cabinet hosting the iTPM and a computing server for post-processing and data storage. The power consumption of the iTPM is ≈150 W. We note that in PHAROS2 the signals are reversed twice in frequency: a first time in the WS, due to LSB tuning, and a second time in the digital backend, due to operation on second Nyquist zone. This double inversion results in non-reversed passbands.

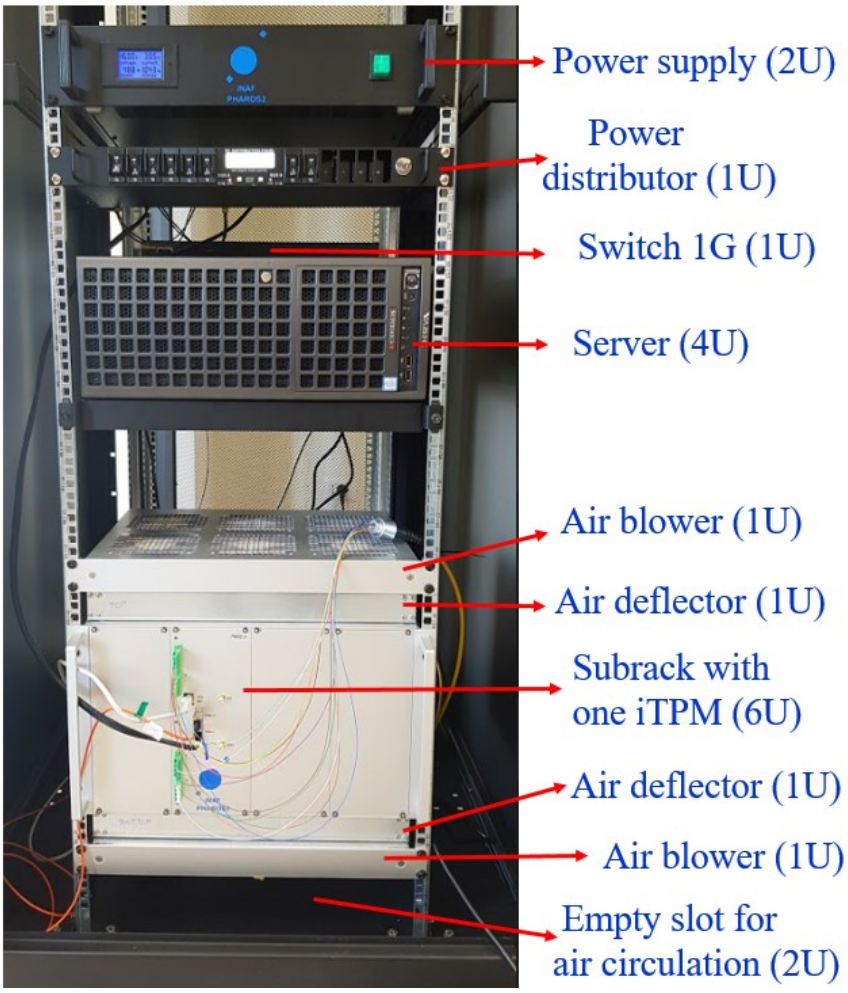

Figure 64 - Digital backend cabinet showing a subrack with one iTPM and air blower for air circulation (bottom), the server, the power supply, the power distributor and the network switch (top).

Conclusion

Due to the SRT radio astronomy-oriented employment, where large bandwidths are required, the radio telescope was characterized by a lack of useable receivers for space debris observations. To improve the capability of the BIRALET system, wherein the SRT is employed as a receiver, in this thesis, a space debris dedicated channel for the SRT has been designed and realized. The new receiving channel has been tested taking advantage of the re-entry of the Tiangong-1 and in several resident space objects measurement campaigns. The measured Doppler frequencies (which are in very good agreement with the estimates) have been employed along with those of different sensors involved in the Tiangong-1 monitoring program, providing useful information about the Chinese space station re-entry.

At present, the SRT allows only Doppler measurements, as the receiver of a CW bi-static radar system. However, to exploit the full potential of the antenna, in the near future it will also be employed for orbit determination purposes. The orbit determination algorithms demand as many range measurements as possible to achieve high accuracy. Accordingly, the BIRALET transmitter is currently being upgraded to transmit both CW and pulsed signals. A mixed transmission, partly pulsed and partly CW, is also planned, so that the system will be able to retrieve the SNR, the Doppler shift, and range at the same time.

A further improvement planned for the BIRALET system is the development of a C-band multi-beam receiver, in particular a Phased Array Feed (PAF). This would allow us to achieve different information using a single antenna pointing with respect to the current mono-beam configuration. In other words, the transit of an object inside the Field of View of the antenna could illuminate different beams, providing information about the space debris trajectory and allowing a high level of detail in the estimation of the ground track of the object.

In this respect, a development of PHAROS2 PAF is described in this thesis, focusing on the design and development of both the front-end and the back-end. In particular, for appreciating the advantages of using a PAF for space debris monitoring, we reported on electromagnetic co-simulations and beam-pattern optimization of PHAROS2 from the primary focus of the SRT. By comparing the far-field differences obtained by feeding with 24 equal-weight Vivaldi elements and with an optimized weight procedure based on CFM, it appears that the SRT efficiency increases from 54% to 237% at 4 GHz, from 12% to 113% at 6 GHz and from 5% to 60% at 8 GHz. This aspect demonstrates that the CFM method for beam-pattern optimization achieves a performances boost of the SRT.

References

[1] A. Ruggiero, P. Pergola, and M. Andreucci, "Small Electric Propulsion Platform for Active Space Debris Removal", *IEEE Transactions on Plasma Science*, vol. 43, no. 12, pp. 4200-4209, Dec. 2015.

[2] F. R. Hoots, P. W. Schumacher, and R. A. Glover, "History of Analytical Orbit Modeling in the U.S. Space Surveillance System", *Journal of Guidance Control and Dynamics*, vol.27, no. 2, pp. 174-185, Apr. 2004.

[3] H. Klinkrad, "Hypervelocity Impact Damage Assessment and Protection Techniques", in *Space Debris – Models and Risk Analysis*, Ed. Springer, 2006, pp. 199-205.

[4] M. Grassi, E. Cetin, and A. Dempster, "Enabling Orbit Determination of Space Debris Using Narrowband Radar", *IEEE Transaction on Aerospace and Electronic Systems*, vol. 51, no. 2, pp. 1231-1240, Jun. 2015.

[5] F. Piergentili, F. Santoni, and P. Seitzer, "Attitude Determination of Orbiting Objects from Lightcurve Measurement", *IEEE Transcations on Aerospace and Electronic Systems*, vol. 3, no. 1, pp. 81-90, Feb. 2017.

[6] H. Klinkrad, "The Current Space Debris Environment and its Sources", in *Space Debris – Models and Risk Analysis*, Ed. Springer, 2006, pp. 5-18.

[7] B. Weeden, P. Cefola, and J. Sankaran, "Global Space Situational Awareness Sensors", *Advanced Maui Optical and Space Surveillance (AMOS) Conference*, Maui, HI, USA, 14-17 Sept. 2010.

[8] D. A. Vallado, J. D. Griesbach, "Simulating Space Surveillance Networks", *Paper AAS 11-580 presented at the AAS/AIAA Astrodynamics Specialist Conference*, Girdwood, AK, USA, 31 Jul.-4 Aug. 2011.

[9] P. Masekell and O. Lorne, "Sapphire: Canada's Answer to Space-Based Surveillance of Orbital Objects", *Advanced Maui Optical and Space Surveillance (AMOS) Conference*, Maui, HI, USA , 16-19 Sept. 2008.

[10] J. Markkanen, M. Lehtinen, and M. Landgraf. "Real-time space debris monitoring with EISCAT", *Advances in Space Research*, vol. 35, no. 7, pp. 1197-1209, Mar. 2005.

[11] D. Mehrholz, L. Leushacke, and R. Jehn, "The COBEAM-1/96 Experiment", *Advances in Space Research*, vol. 23, no. 1, pp. 23-32, 1999.

[12] H. Wilden et. al, "GESTRA – A Phased-Array Based Surveillance and Tracking Radar for Space Situational Awareness", *IEEE International Symposium on Phased Array Systems and Technology (PAST)*, Waltham, MA, USA, pp. 1-5, 18-21 Oct. 2016.

[13] J. Ender, L. Leushacke, L. Brenner, and H. Wilden, "Radar Techniques for Space Situational Awareness", *IEEE Proceedings International Radar Symposium (IRS)*, Leipzig, Germany, pp. 21-26, 7-9 Sept. 2011.

[14] H. Klinkrad, "Monitoring Space – Efforts Made by European Countries", *International Colloquium on Europe and Space Debris*, Nov. 2002.

[15] I. A. Gomez et al., "Description of the Architecture of the Spanish Space Surveillance and Tracking System", *Proceedings of the 7th European Conference on Space Debris*, Darmstadt, Germany, 18-21 Apr. 2017.

[16] D. Ladd et al., "Technical Description of a Novel Sensor Network Architecture and Results of Radar and Optical Sensors contributing to a UK Cueing Experiment", *Advanced Maui Optical and Space Surveillance (AMOS) Conference*, Maui, HI, USA , 19-22 Sept. 2017.

[17] Losacco, M.; Di Lizia, P.; Massari, M.; Mattana, A.; Perini, F.; Schiaffino, M.; Bortolotti, C.; Roma, M.; Naldi, G.; Pupillo, G.; Bianchi, G.; Lama, L.; Cutajar, D.; Magro, A.; Portelli, C.; Reali, M; Villadei, W. The multibeam radar sensor BIRALES: performance assessment for space surveillance and tracking, 69th International Astronautical Congress (IAC), Bremen, Germany, 1–5 October **2018.**

[18] M. Catelani et al.,"Northern Cross Radiotelescope: Test and Measurements of Reliability Performance on Radioreceiver Chains", IEEE Transactions on Instrumentation and Measurement, vol. 58 (10), pp. 3769 - 3777, 2009.

[19] G. Muntoni et al., "Space Debris Detection in Low Earth Orbit with the Sardinia Radio Telescope", *Electronics*, vol. 6, no. 3, pp. 1-16, Aug. 2017.

[20] Bolli, P.; Orlati, A.; Stringhetti, L.; Orfei, A.; Righini, S.; Ambrosini, R.; Bartolini, M.; Bortolotti, C.; Buffa, F.; Buttu, M.; et al. Sardinia Radio Telescope: General Description, Technical Commissioning, and First Light. *J.Astron. Instrum.* **2015**, *4*, pp. 1–20.

[21] Bolli, P.; Olmi, L.; Roda, J.; Zacchiroli, G. A Novel Application of the Active Surface of the Shaped Sardinia Radio Telescope for Primary-Focus Operations. *IEEE Antennas Wirel. Propag. Lett.* **2014**, *13*, pp. 1713–1716.

[22] Muntoni, G.; Schirru, L.; Montisci, G.; Pisanu, T.; Valente, G.; Ortu, P.; Concu, R.; Melis, A.; Urru, E.; Saba, A; Gaudiomonte, F.; Bianchi, G. A Space Debris Dedicated Channel for the P-Band Receiver of the Sardinia Radio Telescope. *IEEE Antennas and Propagation Magazine* in press.

[23] Kesteven, M.; Hobbs, G.; Clement, R.; Dawson, B.; Manchester, R.; Uppal, T. Adaptive Filters Revisited: Radio Frequency Interference Mitigation in Pulsar Observations. *Radio Science* **2005**, *40*, pp. 1-10.

[24] Losacco, M.; Schirru, L. Orbit Determination of Resident Space Objects Using the P-Band Mono-Beam Receiver of the Sardinia Radio Telescope. Appl. Sci. 2019, 9, 4092.

[25] Schirru, L.; Pisanu, T.; Navarrini A.; Urru, E.; Gaudiomonte, F.; Ortu, P.; Montisci, G. "Advantages of Using a C-band Phased Array Feed as a Receiver in the Sardinia Radio Telescope for Space Debris Monitoring," IEEE 2nd Ukraine Conference on Electrical and Computer Engineering (UKRCON), Lviv, Ukraine, 2–6 July 2019.

[26] Navarrini, A.; Scalambra, A.; Rusticelli, S.; Maccaferri, A.; Cattani, A.; Perini, F.; Ortu, P.; Roda, J.; Marongiu, P.; Saba, A.; Poloni, M.; Ladu, A.; Schirru, L. The Room Temperature Multi-Channel Heterodyne Receiver Section of the PHAROS2 Phased Array Feed. Electronics 2019, 8, 666.

[27] A. Navarrini, R. Nesti, L. Schirru, "Electromagnetic simulation and beam-pattern optimization of a C-band Phased Array Feed for SRT",Proceedings of IEEE UKRON2019 Conference, Lviv, Ukraine, July 2-6, 2019.

[28] A. Navarrini, A. Scalambra, A. Melis, S. Rusticelli, R. Concu, P. Ortu, G. Naldi, G. Pupillo, A. Maccaferri, A. Cattani, A. Ladu, L. Schirru, F. Perini, M. Morsiani, J. Monari, J. Roda, P. Marongiu, A. Saba, M. Poloni, M. Schiaffino, A. Mattana, G. Bianchi, G. Comoretto, R. Nesti, E. Urru, T. Pisanu, F. Schillirò, K. Zarb Adami, A. Magro, R. Chiello, "The Warm Receiver Section and the Digital Backend of the PHAROS2 Phased Array Feed," IEEE Int. Symposium on Phased Array Systems and Technology, Waltham, MA, USA, Oct. 15-18, 2019.